Secteur des Sciences de la santé
Ecole doctorale en Sciences médicales
Institute of Neuroscience

Dissertation

TMS-evoked potentials as biomarkers of cortical excitability: from motor networks to the angular gyrus

Dominika Šulcová

supervisors: Prof. André Mouraux, UCLouvain
Prof. Adrian Ivanoiu, UCLouvain

members of the jury: Prof. Valéry Legrain, UCLouvain (president)
Prof. Bernard Hanseeuw, UCLouvain (secretary)
Prof. Julie Duque, UCLouvain
Prof. Thomas König, University of Bern, Switzerland
Prof. Mario Rosanova, University of Milan, Italy

2023

Table of contents

Dedication **5**

List of abbreviations **6**

1. Rationale & aims of the project **8**

2. General introduction **11**

2.1. Excitation-inhibition balance in the brain 11

2.2. Transcranial magnetic stimulation 15

2.3. Electroencephalography 18

2.4. TMS-evoked potentials 19

2.4.1. Multiple sources of TEPs 21

2.4.2. TEPs from the motor cortex 24

2.4.3. TEPs from non-motor cortical areas 28

2.4.4. TEPs from the angular gyrus 29

2.5. Using TEPs to evaluate $GABA_AR$-mediated inhibition 30

2.5.1. TEPs and pharmacological modulation of $GABA_ARs$ 31

2.5.2. Short-latency intracortical inhibition 32

2.6. Summary of aims and objectives 33

3. Investigating the origin of TMS-evoked brain potentials using topographic analysis **34**

3.1. Abstract 34

3.2. Introduction 34

3.3. Materials and Methods 36

3.3.1. Ethical approval 36

3.3.2. Participants 37

3.3.3. Experimental design 37

3.3.4. EEG recording 37

3.3.5. Neuronavigation and TMS 37

3.3.6. Pre-processing of the EEG data 39

3.3.7. TEP peak labelling 40

3.3.8. Planned comparisons 40

3.3.9. Topographic analysis of TEPs 41

3.4. Results 44

3.4.1. TEPs elicited by supra-threshold M1, sub-threshold M1 and AG stimulation 44

3.4.2. Analysis of the topographic dissimilarity between sub-threshold M1 TEPs and AG TEPs 45

3.4.3. Microstate analysis of sub-threshold M1 TEPs and AG TEPs 46

3.4.4. Analysis of the topographic dissimilarity between sub-threshold and supra-threshold M1 TEPs ... 47
3.4.5. Microstate analysis of sub-threshold and supra-threshold M1 TEPs ... 48
3.5. Discussion ... 50
3.5.1. Target specificity of TEPs and the contribution of sensory-evoked responses ... 50
3.5.2. TEP signature of supra-threshold motor cortex activation ... 52
3.5.3. Usefulness and limitations of topographic analysis in TEP evaluation ... 54
3.6. Conclusion ... 55
4. Evaluation of $GABA_AR$-mediated inhibition in the human brain using TMS-evoked potentials ... 56
4.1. Abstract ... 56
4.2. Introduction ... 56
4.3. Materials and Methods ... 58
4.3.1. Ethical approval ... 58
4.3.2. Data and code availability ... 58
4.3.3. Participants ... 59
4.3.4. Experimental design ... 59
4.3.5. EEG recording ... 59
4.3.6. EMG recording ... 60
4.3.7. TMS stimulation and neuronavigation ... 60
4.3.8. Data processing ... 61
4.3.9. Statistical analysis ... 63
4.4. Results ... 64
4.4.1. TEP features depend on TMS stimulation intensity ... 64
4.4.2. Alprazolam modulates peak amplitude of specific TEP components ... 65
4.4.3. Drug-induced change in MEP amplitude is correlated with change in amplitude of TEP N17 ... 65
4.4.4. The effect of alprazolam manifests in RS-EEG ... 66
4.4.5. Alprazolam-induced reduction of N17 correlates with the increase in β band amplitude ... 68
4.4.6. SICI leads to a selective suppression of M1 TEP components ... 68
4.4.7. N17 SICI is correlated with changes induced by alprazolam ... 68
4.4.8. SICI tends to be reduced when $GABA_ARs$ are potentiated by alprazolam ... 70
4.5. Discussion ... 71
4.5.1. TEP signature of pharmacological $GABA_AR$ activation ... 71
4.5.2. RS-EEG signature of pharmacological $GABA_AR$ activation ... 72
4.5.3. TEP SICI and its relation to the effect of alprazolam ... 73

4.6. Conclusion 74
4.7. Supplementary materials 75
4.7.1. Pre-processing of TMS-evoked potentials 75
4.7.2. Microstate analysis as a source of prior for TEP peak amplitude extraction 77
4.7.3. Pre-processing of motor-evoked potentials 79
4.7.4. TMS-evoked potentials from the angular gyrus 81
5. Exploring the properties of the left angular gyrus using TMS-evoked potentials 83
5.1. Abstract 83
5.2. Introduction 83
5.3. Materials and Methods 85
5.3.1. Ethical approval 85
5.3.2. Participants 85
5.3.3. Experimental design 86
5.3.4. EEG recording 86
5.3.5. TMS stimulation and neuronavigation 86
5.3.6. Data pre-processing 87
5.3.7. Data analysis and statistics 88
5.4. Results 90
5.4.1. Spatiotemporal characteristics of AG TEPs 90
5.4.2. Topographic dissimilarity 90
5.4.3. Microstate analysis 93
5.4.4. Contribution of muscular contraction 95
5.5. Discussion 96
5.6. Conclusion 98
5.7. Supplementary materials: Influence of stimulation parameters on AG TEP magnitude 98
5.7.1. Material and methods 98
5.7.2. Results 98
6. Probing intracortical inhibition in the angular gyrus using TMS-EEG 100
6.1. Introduction 100
6.2. Materials and Methods 100
6.2.1. Ethical approval 100
6.2.2. Participants 101
6.2.3. Experimental design 101
6.2.4. EEG recording 101
6.2.5. Neuronavigation 102
6.2.6. TMS stimulation 102

6.2.7. Data pre-processing 102
6.2.8. Preliminary data analysis 103
6.3. Preliminary results 104
6.3.1. Single-pulse AG TEPs 104
6.3.2. Paired-pulse AG TEPs 106
7. General discussion 110
7.1. Early TEPs as biomarkers of local cortical excitability 110
7.2. TEP signature of $GABA_AR$-mediated inhibition 113
7.3. The utility of topographic analysis for TEP evaluation 115
8. Bibliography 118

Dedication

This dissertation marks the end of a long and happy period of my life that was defined by my doctoral studies. Sure, the 'science' part was difficult at times, but mostly it was **fun** – and I am very grateful to all those who made it possible, both at work and outside of it.

Firstly, I would like to thank André for supporting and helping me throughout these past years and for supervising me enough, yet not too much – so now I can feel like I earned it :) . A special mention goes to his willingness to Ad Hoc whenever he has a gap in the schedule and his capability to correct at 6AM whatever I send at 3AM the day before a deadline.

My thanks also go to my co-supervisor Adrian and to my amazing colleagues – my friends, actually – Arthur, Ced, Lieve, Julien, Giulia & Giulia, Fanny, Emanuel, Adriana, Youssef, Yasmine, Tomáš, Sylvie and her bunch... and all the others that keep improving my workdays, you know who you are!

Lastly, it must be said that while a PhD is definitely cool, it wouldn't mean much if I couldn't brag and complain about it to Martin, my family, les Roncerays, and all the other friends. They have endured a lot of both (bragging and complaining) and still stick around and I love them for it. So, this dissertation is actually dedicated to you guys (but you don't have to read it :D).

List of abbreviations

AAC	alpha attenuation coefficient
AD	Alzheimer's disease
AEP	auditory-evoked potential
AG	the angular gyrus
ALS	amyotrophic lateral sclerosis
a/rMT	active/resting motor threshold
ANOVA	analysis of variance (rm – repeated measures)
BDZ	benzodiazepine
CS	conditioning stimulus
COG	centre of gravity
DC	direct current
DISS g	lobal topographic dissimilarity
DMN	default mode network
DLPFC	dorsolateral prefrontal cortex
E/I	excitation / inhibition ratio
EEG	electroencephalography
EMG	electromyography
EOI	electrode of interest
E/IPSP	excitatory/inhibitory post-synaptic potential
ERP	event-related brain potential
fMRI	functional magnetic resonance imaging
GABA	gamma-aminobutyric acid
$GABA_{A/B}R$	GABA receptor type A/B
GEV	global explained variance
GFP	global field power
IAF	individual alpha peak frequency
ICA	independent component analysis
IN	interneuron
ISI	interstimulus interval
LMM	linear mixed model
M1	the primary motor cortex
MARA	multiple artifact rejection algorithm
MEP	motor-evoked potential

MRI	magnetic resonance imaging
MRS	mean root square
MSO	maximum stimulator output
PEP	peripherally evoked potential
PC	principal cell
PCA	principal component analysis
PSD	power spectrum density
ROI	region of interest
RS-EEG	resting-state EEG
SD	standard deviation
SE	spectral exponent
SEM	standard error of the mean
SEP	somatosensory-evoked potential
SICI	short-latency intracortical inhibition
SNR	signal-to-noise ratio
STS	superior temporal sulcus
TANOVA	topographic analysis of variance (non-parametric test)
TCT	topographic consistency test
TEP	TMS-evoked brain potential
TES	voltage transcranial electric current stimulation
TF	transition frequency
TMS	transcranial magnetic stimulation
TOI	time of interest
TS	testing stimulus
vs.	versus

1. Rationale & aims of the project

Human brain is a dynamical system that constantly balances between fast action and steady state, between adaptation and compensation, between chaos and order. To maintain this fragile equilibrium, individual neurons interconnected in complex networks ceaselessly send and receive excitatory and inhibitory signals, thereby fine-tuning the reactivity of the system. The proportion of excitation and inhibition (E/I) is therefore crucial for the optimal function of the brain.

Every neuronal network exists on the E/I spectrum within its own physiological range. While its excitability rapidly fluctuates according to the momentary need, its global characteristics remain constant or change only slowly with age. However, when the balance shifts too far to either side, the excitability of the affected neural network changes, which inevitably impacts its performance. Luckily, the brain disposes of an abundance of buffering mechanisms that make it possible to efficiently compensate for subtle excitability changes within individual cortical areas and circuits, thereby for some time preserving their function. Yet, ultimately, this compensatory capacity gets exhausted and the pathologic changes in local excitability manifest as a specific functional impairment. Furthermore, such aberrant neural activity progressively modifies the synaptic organisation and structural connectivity within the given network, in some cases leading to neuronal death and lesions.

Indeed, many neurological or psychiatric disorders can be linked to a specific E/I dysregulation that corresponds to the underlying pathology and promotes the development of typical cognitive symptoms. Moreover, because of the compensatory mechanisms, considerable alterations in cortical excitability might be present long before the occurrence of cognitive dysfunction. By consequence, progressive neurologic disorders are usually diagnosed only when the compensatory capacity of the brain is surpassed, in other words, when the functional changes are already widespread and often accompanied by irreversible structural modifications.

Clearly, there is a need for a diagnostic tool that would allow to identify pathologic changes in cortical excitability at the earlier, pre-clinical stages of neurological disorders, at the time when it might be still possible to intervene. Such tool should probe the functional state of a specific cortical area or network, while being safe, non-invasive, with minimum contraindications, and with a practical cost low enough so it can be routinely performed in healthy populations at risk (for example reaching a certain age). As it happens, all those criteria can be fulfilled by combining transcranial magnetic stimulation (TMS) with electroencephalography (EEG). Based on the principle of electromagnetic induction, TMS makes it possible to non-invasively and painlessly stimulate a selected cortical site, triggering a synchronised neuronal response that spreads from the target site to other interconnected brain regions. Simultaneous EEG recording captures this time-locked evoked activity in a form of a TMS-

evoked potential (TEP), which then represents an easily obtainable measure that provides information about the excitability and connectivity within the targeted brain network.

In the past two decades, multiple studies showed that TEPs are sensitive to changes in E/I and that the state of excitatory and inhibitory neurotransmission can be evaluated separately if the measure is combined with a suitable experimental manipulation. In other words, by recording TEPs following the stimulation of specific cortical areas, it is possible to estimate the functional state of different brain networks of interest. However, several key points must be clarified before TEPs can be routinely used as biomarkers of cortical excitability.

Firstly, the origin of TEPs has been recently much debated, in particular their likely contamination by sensory and auditory peripherally evoked potentials (PEPs). Therefore, it is necessary – for each targeted brain region – to identify the latencies at which the TEP signal can be reliably linked to the activity directly evoked by TMS in the stimulated area/network. Secondly, individual TEP components presumably reflect the activity of specific large neuronal populations, which may be predominantly excitatory or inhibitory – and most likely is generated by the interplay of both. So, in order to use TEPs to characterize local E/I, we must first determine which TEP peaks correspond to which processes. Lastly, each cortical region has a distinct cytoarchitecture, connectivity, and by consequence specific functional properties. Large number of past publications reported TEPs evoked from the primary motor cortex (M1), because the stimulation of this area elicits a measurable contraction of the corresponding muscle, thereby providing a useful input-output readout. For this reason, the spatiotemporal profile of M1 TEPs is now well known, and it is possible to further explore the significance of this measure as well as its potential clinical use. Yet, M1 TEPs primarily relate to the state of (sensory)motor circuits, whereas other cortical targets may be better suited to investigate different brain networks. It is therefore crucial to thoroughly characterize the physiological profile of TEPs from non-motor regions of interest and to identify the optimal stimulation parameters for their acquisition.

In the present work, we aimed to address each of these points, while investigating two specific cortical regions. Next to the M1, the most explored TMS target often stimulated in clinical practice, we focused on the angular gyrus (AG). This area represents a highly connected cortical hub that is involved in several large-scale brain networks and participates in innumerable cognitive processes. For that reason, changes in AG excitability can be expected to accompany the development of various neuropsychiatric syndromes – an assumption that is supported by reports of structural or functional impairment of this region in diseases such as schizophrenia or Alzheimer's disease. Furthermore, the AG is conveniently located at the outer brain surface in the reach of the classic TMS, which makes it possible to explore its functional properties using TMS-EEG. Therefore, AG TEPs – if properly characterized – have the potential to become a valuable non-invasive biomarker that could provide information about the state of this brain region at the pre-clinical stages of neuropsychiatric disorders.

In the first study (chapter 3), we recorded TEPs from the two regions of interest, the left M1 and the left AG, and compared obtained signals using topographic analysis – namely the analysis of topographic dissimilarity and microstate analysis – to distinguish TEP components that are specific for each stimulation site from those that are extensively contaminated by PEPs. In addition, we stimulated the M1 with intensities under and above the threshold for eliciting a motor response and used the same methods to compare these two M1 datasets, thereby describing the TEP signature of cortico-spinal activation as well as the possible confounding sensory response to the evoked contraction of hand muscles. Within the same experimental setup, we then performed a second study (chapter 4) that investigated the effect of increased inhibitory neurotransmission on all three categories of TEPs (sub- and supra-threshold M1 TEPs and AG TEPs). To this end, we introduced two different experimental manipulations: (1) we selectively stimulated inhibitory signalling with benzodiazepines and (2) used paired-pulse TMS protocol to induce the short-latency intracortical inhibition (SICI). Next, we focused on the AG. In the third study (chapter 5), we recorded AG TEPs using various combinations of stimulation parameters. Using topographic analysis, we aimed to describe in detail the spatiotemporal profile of the response, determine the optimal recording settings, and identify AG TEP components reflecting the activity within the stimulated network. Finally, in the fourth study (chapter 6), we used the previously established TMS parameters to apply paired-pulse stimulation to the AG and elucidate the effect of SICI on AG TEPs.

2. General introduction

2.1. Excitation-inhibition balance in the brain

The dynamics of neural processes at all the levels of the brain hierarchy, starting with individual cortical microcircuits and ending with large-scale networks, are shaped by a complex interplay of excitatory and inhibitory signals. These are generated at synapses[1] with the help of two major neurotransmitters: glutamate and gamma-aminobutyric acid (GABA). Glutamate binds to its cation-permeable receptors, thereby triggering an influx of Na^+ and Ca^{2+} that quickly (< 10 ms) depolarizes the post-synaptic membrane and produces an excitatory post-synaptic potential (EPSP) [1]. The interaction of GABA and its ionotropic receptors A ($GABA_ARs$) causes an equally swift entry of Cl^- ions, which has an opposite, hyper-polarizing effect, resulting in an inhibitory post-synaptic potential (IPSP) [2]. In addition to its fast $GABA_ARs$-mediated effect, GABA can also activate metabotropic receptors B ($GABA_BRs$), which eventually leads to an opening of inward-rectifying K^+ channels and closing of voltage-gated calcium channels, thereby imposing a slow (100–500 ms) post-synaptic inhibition [3, 4]. All post-synaptic potentials spread from receiving synapses towards the neuronal body, interacting with local microenvironments and slowly weakening as they go, to finally sum up at the axonal hillock. If a large number of EPSPs occur simultaneously, the hillock membrane may get sufficiently depolarized to generate an action potential. Therefore, the output activity of each neuron is determined by the character, number, and temporal coordination of incoming signals as well as by its intrinsic properties that determine the integration of these signals, such as membrane conductance, resting potential (typically in a range from -85 to -60 mV) and threshold potential (usually around -50 mV) [5].

In the mammalian brain, excitatory glutamatergic cells (or 'principal cells') make up the large majority of all cortical neurons, with inhibitory GABAergic cells constituting only 10-15% [6, 7]. Yet, GABA is typically released in about 30% of all synapses and represents the most widely distributed neurotransmitter of the central nervous system [8, 9]. This reflects the abundant connectivity of inhibitory neurons, which – in contrast to their excitatory counterparts – rarely form long-range projections and limit their sphere of influence to local cortical circuits (hence the name 'interneurons') [10]. Moreover, the exact manner in which any such circuit is wired depends to a great extent on the type of inhibitory cells it contains, as these display an overwhelming diversity in their preferred targets and synaptic locations, which subsequently defines their effective connectivity within a given network. To this day, three main sub-populations of GABAergic neurons have been identified based on their protein expression profile, each including numerous interneuron classes with distinct morphology and connectivity profiles. So, for example, while somatostatin-expressing Martinotti cells typically form

[1] Both excitatory and inhibitory neurotransmission can also take place outside of the synapse. However, to limit the scope of the introductory text, the extra-synaptic mechanisms will be disregarded.

synapses with apical dendrites of principal cells, parvalbumin-expressing basket cells preferentially contact their proximal dendritic segments and the soma, whereas serotonin receptor-expressing bipolar cells project to other interneurons [11, 12].

The interactions between principal cells and interneurons in a local network are reciprocal: a single interneuron often innervates more than 50% of the surrounding principal cells and receives excitatory inputs from a considerable portion of them [13]. Such bidirectional connectivity gives rise to the 'feedback' inhibition of principal cells in response to their own activity (Fig. 2.1A). The excitatory input can also come from neurons located in distant brain areas (for example in thalamic nuclei), which project both to local principal cells and interneurons. In this case, activated principal cells receive slightly delayed signals from co-activated interneurons resulting in their 'feedforward' inhibition (Fig. 2.1B). Finally, if interneurons synapse to each other, their excitation leads to a disinhibition of the network (Fig. 2.1C) [14, 15]. The recruitment of inhibitory cells through feedback or feedforward excitatory connections guarantees a certain proportionality of excitation and inhibition in the system. This was directly confirmed by *in vivo* electrophysiological recordings in animals, showing that following an external stimulus, neurons in the corresponding sensory cortex experience simultaneous increase in excitatory and inhibitory inputs [16-19]. Similarly, during resting-state activity, the strength of excitatory and inhibitory neurotransmission in various (also non-sensory) cortical assemblies fluctuate in synchrony in line with spontaneous cortical oscillations [16, 20]. Therefore, despite being in direct opposition, synaptic excitation and inhibition represent two inseparable events.

At the level of a single neuron, the ratio of excitatory and inhibitory neurotransmission (E/I) can change extremely fast. The activity of principal cells usually precedes the recruitment of interneurons (either through feedback or feedforward mechanisms) by a couple of milliseconds, which creates a short window of high E/I that subsequently shifts towards low values when the inhibition kicks in [21]. At the level of a whole network, the precise value of E/I depends on the architecture of the circuitry, current level of activity and the firing properties of involved neurons. Yet, over longer periods of time, it is maintained in balance and remains robust to perturbations [22]. To explain the dynamics of E/I, it was recently proposed that physiological cortical circuits may operate as inhibition-stabilized networks [23]. In such configuration, network behaviour is governed by strong feedback inhibition mediated by $GABA_A$Rs. When the external excitatory input is weak, principal cells are little activated and the recurrent inhibitory connections stay silent. In such case, the resulting cortical output is highly variable and shows non-linear relation to the strength of the input. However, following a strong external stimulus, local excitatory activity sharply increases, which in turn recruits a massive inhibitory response and the input-output relationship of the network becomes linear and predictable [22, 24].

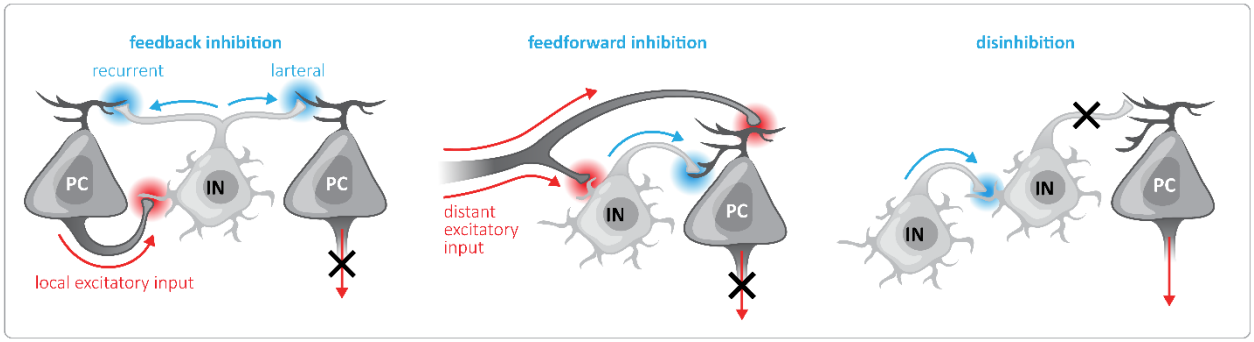

Figure 2.1 Basic neuronal circuit motives: (A) Feedback inhibition (blue) occurs when the excitatory signal (red) comes to interneurons (IN, light grey) from local principal cells (PC, dark grey). Activated INs then inhibit the PCs that originally provided the excitatory impulse (recurrent inhibition) and/or previously silent local PCs they innervate (lateral inhibition). **(B) Feedforward inhibition** is triggered by parallel excitatory inputs coming from distant PCs both to local PCs and INs. **(C) Disinhibition** occurs when an IN targets another IN, thereby preventing it from inhibiting PCs.

While the feedback inhibition drives the immediate E/I towards its baseline values, the explosive (albeit very brief) cortical activation triggered by a sufficiently powerful (= relevant) excitatory input leads to the amplification of the signal and enables its transmission across a distributed large-scale brain network. Since the duration of the initial excitation determines the extent of such amplification, the precise timing of local inhibition is crucial for the propagation of information and its integration [25, 26]. Furthermore, the character of the recurrent inhibitory response reflects the overall reactivity of principal cells in the circuit and further sharpens their selectivity for a specific stimulus, thereby increasing the information content in the system [21]. Finally, it has been repeatedly shown that a specific interneuron activity conditions the generation and modulates the temporal features of cortical oscillations [27-31], which then mediate the communication between multiple networks [32]. Therefore, it seems that the fast inhibitory neurotransmission plays a key role in the complex multiscale processing of the information in the brain by controlling the spatiotemporal dynamics of network activity, which would otherwise turn into an excitatory chaos.

The efficiency of inhibition-based regulatory mechanisms is dependent on network excitability and is therefore closely linked to the optimal long-term tuning of E/I. For this reason, neurons dispose of an array of homeostatic mechanisms that keep the overall level of network activity within a physiologically acceptable range. Any deviation in E/I entails slow (manifesting within hours or days) compensatory adjustments in intrinsic excitability of neuronal cells and/or their synaptic architecture [33]. Similar molecular machinery stands behind the activity-induced changes in connectivity that contribute for example to learning or memory encoding. In such cases, the plastic reorganisation of inhibitory and excitatory synapses is coordinated so that the overall E/I remain constant [34-36]. Therefore, the optimal functioning of the brain is enabled by the coexistence of homeostatic and synaptic processes that operate at different temporal scales: while the whole system exists in a global

equilibrium, individual neurons or their sub-populations dynamically enter transient instable states, thereby producing rapidly changing patterns of activation that represent individual steps of information processing.

As described earlier, the value of E/I defines network's response to an external stimulus. Under normal conditions, an optimally maintained E/I tends to maximize the signal-to-noise ratio (SNR) in the system, thus supporting the correct treatment of the information and by consequence the appropriate function of the system. When the balance is disturbed and the E/I tips either to excessive excitation or excessive inhibition, the SNR drops and the network performance decreases as well (Fig. 2.2) [37]. Importantly, due to the complexity and high dimensionality of cortical circuits, a shift in E/I may be possibly caused by a malfunction of either (or multiple) of the involved neuronal populations. For example, an observed state of hyperexcitability may have its origin in an increased activity of excitatory cells or in an impaired function of inhibitory cells. In this aspect, inhibitory interneurons represent a weak link in the neuronal chain, because their low numbers and high specialisation renders them less redundant than the principal cells [11, 38]. Moreover, any defect of the synaptic inhibition – originating either pre- or post-synaptically – can be also expected to impact the precise regulation of neural dynamics.

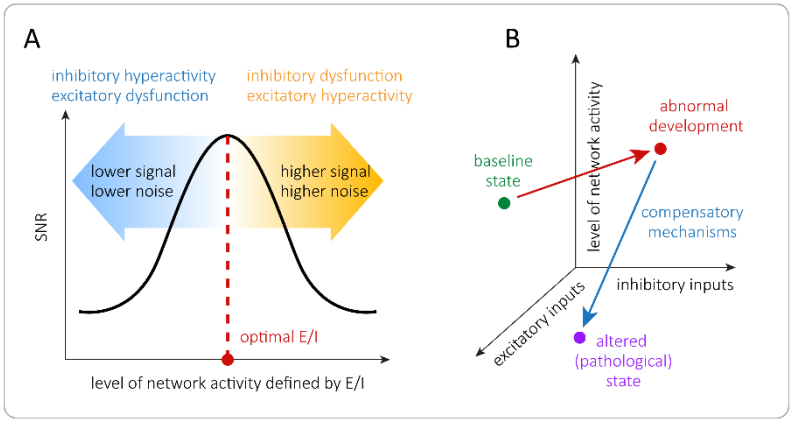

Figure 2.2 Excitation/inhibition balance in networks. **(A)** Increased E/I may reduce SNR by augmenting the noise in the circuit, thereby rendering it less responsive to relevant inputs. The noise could represent meaningless signals or the state of excessive conductance that leads to low neuronal gain. Conversely, lower E/I may effectively reduce SNR by dampening the relevant signals. **(B)** E/I can be represented as a multidimensional space, with different mechanisms (pathologic, homeostatic) perturbing the networks along its different axes.
adapted from: Sohal et al., 2019 [37]

The functional impairment of a specific brain network resulting from its chronically aberrant E/I ultimately manifests as a neuropsychiatric syndrome with symptoms that reflect the character and purpose of the perturbed circuit (although this doesn't mean that *all* the associated clinical symptoms are necessarily linked to the shift in E/I). Indeed, an E/I disbalance in one form or another has been observed in a large and diverse group of neuro-pathologies including epilepsy [39], schizophrenia [40], autism [41], amyotrophic lateral sclerosis [42] and Alzheimer's disease [43].

In the framework of scientific research, it is useful to define the term 'cortical excitability'. It refers to the current overall E/I of a specific cortical network – or, more likely, functionally or anatomically defined cortical area(s) – which itself depends on a great number of mostly inaccessible parameters. Because the value of E/I is tightly linked to the input-output properties of the circuit, it can be assessed *in vivo* by describing the cortical response to an appropriate external stimulus [44, 45]. Depending on the network of interest, the stimulation can be delivered in different forms and various tools are currently available that allow to measure the subsequent brain's reaction. Furthermore, when combined with the right experimental manipulation, a readout of cortical excitability can provide selective information about the state of individual contributors, including the local inhibitory system. Some of these methods will be introduced in the following chapters.

2.2. Transcranial magnetic stimulation

In 1985, Anthony Barker and his colleagues introduced a new method of non-invasive stimulation of the human brain based on the principle of electromagnetic induction [46]. When applied over the M1 with sufficient intensity, TMS reliably evoked a contraction of contralateral limb muscles, thus demonstrating its capability to trigger action potentials in cortical motoneurons. Furthermore, when compared to high-voltage transcranial electric current stimulation (TES), an approach established a few years earlier [47, 48], TMS brought about one major advantage. High-voltage TES requires a potential of several hundred Volts between the electrodes for the electric current to reach the target cortical structure – an intensity that inevitably activates pain receptors in the scalp as well as motor nerve terminals in nearby cranial muscles, causing their strong and often unpleasant contraction. In contrast, TMS activates cortical neurons painlessly and, in ideal cases, without provoking noticeable muscle twitches, thereby allowing for longer stimulation sessions with minimal discomfort for subjects [49]. For that reason, it became the tool of choice when targeting the M1 as well as other cortical areas and is now well established both in experimental research and in clinics.

A TMS device consists of a stimulator coil containing several superimposed loops of copper wire, which is connected to a large capacitor via a switch (Fig. 2.3A). When discharged, the capacitor releases to the coil an electric pulse that lasts less than a millisecond and can gain up to several thousand Ampers [50]. This pulse is essentially composed of two successive currents of opposite phases which can adopt different waveforms (Fig. 2.3B). A 'monophasic' pulse is dominated by a strong initial current that carries the main effect of the stimulation and is followed by a heavily dampened return current with minimal physiological impact. In contrast, both phases are fully preserved in a 'biphasic' pulse, with the reversed current usually lasting longer and having more physiological relevance [51, 52]. The electric current passing through the coil generates a rapidly changing magnetic field directed orthogonally to the plane of the coil loops. It only lasts several hundred µs (depending on the device),

yet its magnitude (1-4 Tesla), which is proportional to the coil current strength according to Ampere's circuital law, can be compared to the static field of magnetic resonance imaging (MRI) scanner. When the stimulator coil is placed on the scalp, the magnetic field enters the brain without being hindered by the resistant barrier of the skull. In line with Faraday's law [53], it induces there a phasic electric field (E-field), which is oriented perpendicularly to the lines of the magnetic flux and whose strength rapidly falls off with the distance from the coil (Fig. 2.3C) [50, 54]. The E-field forces charged particles of the environment (ions) to flow along its gradient, thereby forming electric currents in the tissue that would circulate in loops parallel to the plane of the stimulator coil in the direction opposite to the coil current, were the brain a homogeneous sphere. In reality, induced electric currents follow the brain anatomy and are influenced by differences in electric conductivity caused by transitions between tissues with distinct compositions. This ultimately leads to local accumulations of electric charges that give rise to superimposed secondary E-fields [55, 56].

Despite the wide use of TMS, the exact mechanisms through which the induced E-fields engage the target cortical structures and trigger the spread of activity across the whole brain are still not completely understood (for a review see [57]). In principle, the flow of charges in the extracellular space causes a shift in the membrane potential of cortical neurons at the site of stimulation, depolarizing them and thereby increasing the probability of the action potential generation. Due to the fast decay of the E-field with the distance from the coil, the neurons located in gyral crowns and, generally, in the superficial layers of the target cortex are always stimulated with a higher intensity. Considering the exact site of action, it seems that the stimulation rather affects myelinated axons than cell somas or dendrites, at least when one focuses on the M1 [58-60]. Because the E-field is practically homogeneous at the spatial scale of cortical neurons, its gradient along the axons contributes only little to the evoked response [61]. Instead, it is likely that TMS predominantly acts at locations where the axons abruptly change their geometry, such as at their synaptic terminals within the grey matter [62, 63] or at their bends when entering the white matter [64, 65] (Fig. 2.3C).

The final neural response to TMS is extremely complex and combines the activity of multiple neuronal populations that might be affected to various degrees and respond in various ways, according to their inherent properties [57, 66]. Their identity is determined by the anatomy and cytoarchitecture of the target cortical region, but it also strongly depends on the specific character of the E-field itself. All predictive models agree that the excitation of neuronal axons in the grey matter is critically conditioned by the magnitude of the E-field and its orientation relative to the axonal course. This has been repeatedly confirmed by experimental studies that reported different outcomes when stimulating the same cortical site while varying stimulation parameters and by consequence the properties of the induced E-field. Naturally, the bulk of evidence came from the stimulation of the M1, due to the possibility to conveniently record the output of the stimulated cortex from the peripheral

muscle in a form of a motor-evoked potential (MEP). There, it has been shown that the evoked response differs both qualitatively and quantitatively when changing the stimulation intensity, coil orientation, and electric pulse configuration [58, 59, 67-72]. More recently, similar observations were also made following the stimulation of non-motor cortical areas by using the electroencephalogram as the outcome measure [73, 74].

Since the character of the E-field is crucial for the estimation of the stimulation effect, great efforts were made during the years to improve its modelling. Due to the complex structure of the human brain, the spatial distribution of the electric charge in its volume is heterogeneous and varies according to subject's anatomy. Therefore, currently employed models typically use the method of finite elements or the method of boundary elements to reconstruct the E-field based on individual MRI images [75-77], striving to optimize the TMS parameters for the cortical areas beyond the M1 [78, 79]. However, the E-field distribution alone is not sufficient to predict the outcome of the stimulation, as this equally depends on the specific characteristics of recruited neuronal populations. For that reason, new approaches were developed in recent years that combine anatomically-informed E-field models with the simulation of realistic neuronal networks [66]. It is the hope that in the future, such models might considerably increase the accuracy and efficacy of TMS.

Because the induced E-field is greatest directly under the loop circumference and virtually non-existent at its very centre, the coil shape also influences the spatial reach of TMS. A simple circular coil induces a powerful E-field all along its course, thereby affecting multiple neighbouring brain structures. The focality of stimulation can be improved by using a figure-of-eight coil, where two stacks of loops are overlapping, and the E-field is the strongest under the coil centre [80]. The penetration of the field can be further increased by introducing an angle between the two circular loops (resulting in a so-called double-cone coil) or by otherwise modifying the wire geometry (like in H-coils). It is then possible to stimulate deeper brain structures, such as cortical areas located in medial walls of brain hemispheres, although this comes at the expense of the targeting precision [81-83]. This fundamental trade-off between stimulation reach and focality is also linked to the coil size irrespective of its shape, larger coils generally reaching deeper in the tissue but producing less focal E-field [84, 85].

Stimulation precision, or spatial resolution, represents an important parameter of TMS, especially when considering its clinical application. Based on the E-field modelling, it has been estimated that a cortical area of several cm^2 may be efficiently stimulated by a single TMS pulse [55]. However, a recent study recording single-neuron activity from the macaque parietal cortex clearly showed that the neuronal response to TMS is limited to the cortical site of several millimetres in diameter [86]. Such focality of stimulation is in line with previous observations in human subjects that TMS of M1 can elicit twitches of individual fingers [87], while the M1 area for a single finger movement measures about 4 mm^2 [88]. The high spatial selectivity of TMS was further confirmed by a recent study by Passera et al.,

who used EEG recording in humans to determine the functional TMS resolution as approximately 10 mm [89]. Taken together, these findings indicate that precisely defined, localized cortical targets can be stimulated by TMS without widespread concomitant activation of neighbouring regions, thus allowing for selective engagement of individual brain systems and networks.

2.3. Electroencephalography

Although its invention dates back almost a century [90], modern EEG is still nowadays widely used to explore the electric activity of (not only) the human brain. There are multiple reasons for its unwavering popularity. The method is based on non-invasive recording of voltage fluctuations at the scalp that reflect the everchanging collective output of the underlying neuronal assemblies [91]. Because the temporal resolution of current EEG systems can easily match the speed of neuronal processing at the millisecond scale [92], it allows to accurately capture the fast-paced dynamics of neural events in the brain and link them to specific cognitive processes or their pathologies. Furthermore, thanks to its relatively low cost, portability and virtually no contraindications, EEG is well suited for clinical diagnostics as well as experimental research.

During an EEG recording, the electric signals emitted by the brain are measured by a set of scalp electrodes whose numbers can range from a few to several hundred. The voltage sampled at each electrode corresponds to a time-varying difference between the measure at the active channel and one or two reference electrodes (an additional ground electrode is used to reduce the electric interference of the environment) [93]. At each timepoint, recordings of all channels compose a topographic map of voltage distribution, which can be regarded as a scalp projection of all simultaneously occurring electric fields in the brain. Each individual minuscule electric field is generated by electrochemical signals passing between neurons. When millions of such transmissions coincide in time within a spatially aligned network, their electric fields compose into a signal that is powerful enough to be measured outside of the head. Therefore, surface EEG predominantly captures strong synchronous activity of big neuronal populations with specific spatial properties, while largely ignoring all the rest [94].

It is generally agreed that the deflections in the EEG signal mostly reflect extracellular electric currents generated by the temporal summation of post-synaptic potentials at the dendrites of cortical pyramidal cells [95, 96]. These neurons, parallel to each other, are oriented perpendicularly to the brain surface, with an apical dendritic tree and an axon diving into the white matter. Synaptic activity at the level of superficial dendrites leads to local negative (excitatory synapse = cation influx) or positive (inhibitory synapse = cation efflux) extracellular charge, which is then compensated by an opposite charge appearing at the level of the neuronal soma, thereby forming an electric dipole (the aforementioned electric field) whose direction is determined by the type of synaptic input (Fig. 2.3D).

However, when the receiving synapse is located deeper, in the proximity of (or even at) the soma, the resulting dipole is reversed, with the compensatory charge building up in the distal dendritic tree. Therefore, both excitatory and inhibitory neurotransmission can produce local electric fields of the same orientation depending on the exact synaptic location, which means that the polarity of voltage deflections measured by EEG cannot be automatically associated with either [97].

The spontaneous EEG signal is dominated by rhythmic activity (although it also has a significant aperiodic component [98]) detectable in the spectrum comprising delta (approximately 1 – 4Hz), theta (4 – 8Hz), alpha (8 – 12Hz), beta (12 – 30Hz) and gamma (30 – 80Hz) frequency bands [99, 100]. These neural oscillations are caused by excitability fluctuations within multiple neuronal populations, which, in turn, are driven by a combination of periodic inputs from thalamocortical and corticocortical connections [101]. According to the identity of their generators, the resulting oscillations show different spatiotemporal profiles with distinct scalp distributions and dominant frequencies. The functional significance of different neural oscillations likely varies, as they arise from distinct brain circuits through heterogenous biophysical mechanisms [102]. Correspondingly, various neural processes have been linked to a specific type of rhythmic activity, whose features can subsequently provide information about the current brain state [103].

Due to the volume conduction of the brain and the surrounding tissues, the electric output of each cerebral source contributes to different extent to the voltage measured at multiple electrodes. This means that two recordings from neighbouring channels cannot be considered as independent as they to a large extent sample the same underlying activity [104]. Because of such blurring, the spatial the location of individual generators in the brain volume is not apparent based on the scalp topography. Yet, in order to correctly interpret the measured signal, it is often necessary to link it to a specific functionally defined brain structure, and the past years saw a huge advance of computational models aiming to estimate the sources of EEG. The location accuracy of these models keeps improving, as the simulation of conductive properties of different brain and head tissues becomes increasingly more realistic. However, the inverse mapping remains an ill-posed problem: any voltage distribution recorded at the scalp can be possibly generated by multiple combinations of participating neural sources. Furthermore, the source estimation is highly sensitive to small signal changes that are often related to the EEG noise [105, 106].

2.4. TMS-evoked potentials

The combination of single-pulse TMS and concurrent EEG constitutes a unique tool for exploring the functional properties of the human brain. This approach benefits at the same time from the spatial resolution of TMS, which – when aided by MRI-based neuronavigation – allows to directly stimulate a single cortical region targeted with a millimetre precision, and from the temporal resolution of EEG

corresponding to the millisecond-scale dynamics of normal neural events [107, 108]. While originally troubled by the presence of a large recording artefact caused by the electromagnetic interference [109], the fast-paced development of EEG hardware as well as the continuous improvement of data processing techniques made it soon possible to isolate the EEG signal corresponding to the TMS-evoked activity [107, 110]. As a result, during the past two decades, the application of TMS-EEG generated an abundance of valuable information about the neural processes underlying both physiological and pathological brain states (for review see for example [111]).

TEPs represent the EEG readout of the neural response to the stimulation and when evaluated in the time domain, it usually corresponds to the synchronous evoked neural activity that is time-locked to the stimulus. Due to the relatively low amplitude of the signal and the generally high background activity of EEG data, several tens of trials are typically averaged to obtain a clear TEP. The final signal appears as a sequence of voltage deflections that are time-locked to the TMS stimulus and last for several hundred milliseconds [107, 112] (Fig. 2.3E). The spatiotemporal profile of TEPs is highly reproducible at the group level [113], but varies substantially across individual subjects [114] and shows distinct features depending on the site of stimulation [89, 115] and the used set of stimulation parameters [73, 74, 116]. Furthermore, it can be modulated by the momentary neuronal state in the target cortex [117-119] or by the overall brain state, for example by subject's vigilance [120, 121]. Because TEPs reflect, at least partially, the activity directly triggered within the stimulated cortex and its subsequent spread to the interconnected brain regions, they can provide information about the functional properties of the target cortical area as well as the larger brain network this area functionally integrates [122-124]. Furthermore, based on the assumption that individual TEP components correspond to the consecutive processing steps of the evoked response [125], their features have been also used to characterize the effective connectivity between the activated brain regions [126, 127].

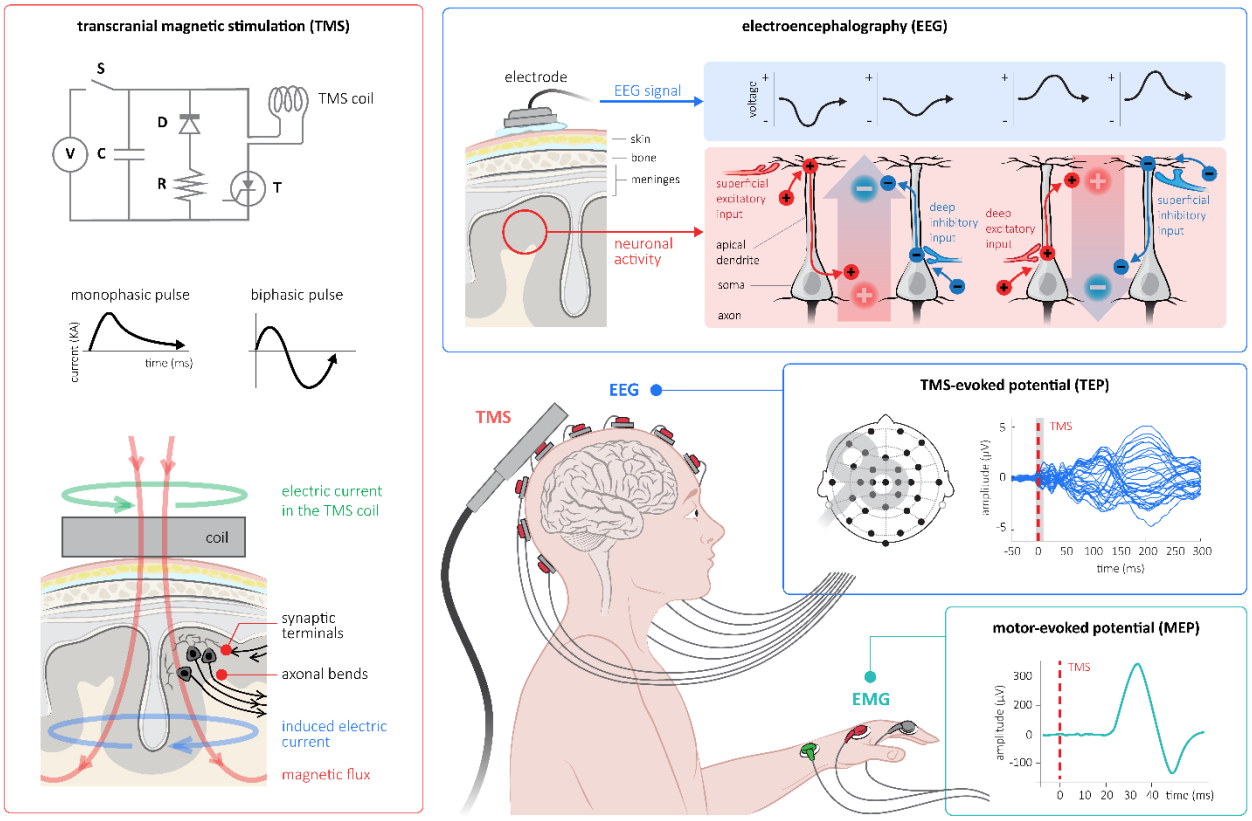

Figure 2.3 Methods. (A) TMS – schema of the stimulator circuit. The TMS coil is attached to the main unit that typically contains a switch (S), a voltage source (V), a capacitor(C), a diode (D), a resistor (R), and a thyristor (T). **(B) TMS – configuration of the electric pulse.** Schematic illustration of the biphasic and monophasic TMS pulse waveforms. **(C) TMS – mechanism of the stimulation.** When the TMS coil (in grey) is placed tangentially on the scalp and the electric pulse rushes through its loops in one direction (in green), it generates a strong magnetic field oriented perpendicularly to the coil (in red) that traverses the skin and the skull as well as the meningeal envelopes of the brain (in white, from the most external – dura, arachnoid, and pia mater) and reaches the brain. There, it induces an electric field (in blue) with the currents flowing parallel to the electric current in the coil but in the opposite direction. The E-filed distribution is influenced by local brain anatomy and contains areas with charge accumulation. Myelinated axons of cortical neurons are most stimulated at their terminals in the grey matter and in their bends at the transition from the grey to the white matter (red dots). **(D) EEG – generation of the signal.** An EEG electrode samples the changes in voltage generated by the neural activity in the brain that is transmitted to the scalp through the meninges, the skull, the skin, and the layer of conductive gel. The polarity of such voltage change (blue panel) depends on the type and location of the synaptic input to the cortical pyramidal neurons, whose post-synaptic potentials represent the main sources of the EEG signal (red panel). IPSPs and EPSPs cause an exchange of ions between the neuron and the environment (red – cations, mostly Na^+; blue – anions, mostly Cl^-), thereby creating an electric dipole in the extracellular space. Superficial excitatory or deep inhibitory inputs create a dipole with the negativity oriented towards the gyral surface, while deep excitatory or superficial inhibitory activity leads to a positivity at the gyral surface **(E) TEP.** Left – 32-channel EEG layout with mastoids marked with empty circles (in our studies used as reference channels), the TMS coil (in grey) is displayed in the position typical for the stimulation of the left M1. Right – a butterfly plot of a group averaged TEP recorded from the M1. Each blue line represents the signal of one EEG channel, the shaded in light grey denotes the signal replaced by interpolation. TMS stimulus is marked in red. **(F) MEP.** Typical biphasic wave associated with the muscular contraction evoked by sub-threshold M1 stimulation. TMS stimulus is marked in red.

2.4.1. Multiple sources of TEPs

When recording TEPs, the aim is to use this measure to characterize the above-described brain activity evoked within the stimulated brain area and the connected network. The major advantage of this direct cortical stimulation is that the brain response doesn't require subject's engagement and should therefore exclusively relate to the functional state of the target brain areas. However, in reality,

the TMS-evoked activity captured by TEPs is inevitably contaminated by several simultaneously occurring events of both extra-cranial and cerebral origin that mix with the genuine cortical response and considerably complicate TEP interpretation.

Firstly, the strong (although brief) magnetic field interferes with the recording system at the level of electrodes, causing a high-amplitude EEG artifact that completely masks all other ongoing activity. Its contribution can be minimized by different hardware modifications that typically allow to recover the underlying signal within a few milliseconds, although the channels close to the stimulation site may be affected longer [110, 128, 129]. These channels also often suffer from a large voltage shift lasting up to 100 ms that likely reflects the discharge of electric currents built-up in the electrodes, their lead wires, and in the underlying conductive tissues [130-133]. In addition, the contact between the TMS coil and EEG electrodes can lead to their movement or contamination with line noise [134], and a specific artifact can be also caused by the recharge of TMS capacitors [128, 135]. The presence and magnitude of all these instrumental disturbances vary across different TMS devices [135], TMS coils [136], and types of EEG electrodes [137]. While they can be to some extent reduced by a careful setup configuration, these artifacts are usually efficiently removed from the data using offline source-separation techniques such as principal component analysis (PCA) [130] or independent component analysis (ICA) [138, 139].

The electrogenic activity of different physiological systems constitutes the second major source of extra-cranial TEP artifacts. Similarly to any other EEG recording, TEPs can be contaminated by eye blinks, saccadic eye movements, tonic contraction of head and neck muscles, and ongoing heart beats. While these events often significantly impact the signal, their occurrence is not time-locked to the TMS stimulus (unless we are very unlucky) and the spatiotemporal and spectral features of the associated artifacts are usually well defined and consistent in individual subjects. For these reasons, it is relatively easy to filter out their contribution with ICA [139]. However, the TMS pulse can also provoke a contraction of underlying muscles, either by directly depolarizing their fibres or (more likely) by stimulating local terminals of appropriate motor nerves [135, 140, 141]. The resulting evoked potential typically consists of a biphasic peak that can reach several hundred microvolts and persist for about 10 ms following the TMS stimulus, although the closest EEG channels may be affected by a longer-lasting tail of the artifact. Its topography is often lateralized, with the specific pattern determined by the anatomical properties of the contracting muscle relative to the TMS coil position, and it is therefore highly variable across subjects [135, 141]. The character of the artifact also varies according to the used hardware and chosen stimulation parameters, and its magnitude can fluctuate from trial to trial depending on the momentary neuromuscular excitability [135, 141]. Several offline techniques were previously successfully used to remove this muscular artifact from TEP data, including different variation of ICA [138, 139, 142, 143], PCA [144] or an alternative approach based on signal-space-

projection [145, 146]. Although seemingly efficient, these methods still present a risk of alternating the underlying signal of interest, and as such should be applied with caution.

Finally, the most problematic source of TEP contamination is the activity generated by the brain in response to TMS stimulation of various peripheral structures. The magnetic field, which is considerably more powerful at the level of the scalp than in the depth of the cerebral cortex, induces electric currents in the skin, cerebrospinal fluid, and meninges. This in turn triggers a variety of local receptors, whose discharge activates appropriate afferent pathways and results in a compound somatosensory-evoked brain potential (SSEPs) [107, 147]. Another response with a similar spatiotemporal signature (but presumably slightly different onset) can be evoked by the TMS-induced contraction of the face and neck muscles (Fig. 2.4B,C). Furthermore, the electric current passing through the TMS coil produces a loud clicking noise that stimulates the auditory system (causing auditory evoked brain potentials (AEPs; Fig. 2.4D) as well as the proprioceptive system through the sound-related vibration [148, 149] (Fig. 2.4A). All these evoked potentials (collectively labelled peripherally evoked potentials, PEPs) are time-locked to the stimulus, with topographic patterns corresponding to normal brain activity. They are therefore completely entangled with the genuine cortical response to TMS and represent a major confounding factor hampering the reliable interpretation of TEPs [150].

Certain preventive measures can be adopted (and are highly recommended) during the recording session to minimize the occurrence of PEPs in the data. Masking sound, ideally based on white noise combined with the recorded sound of the TMS click, is usually used to reduce the salience of the auditory stimuli [151], and a layer of soft plastic or thin foam placed under the coil helps minimize the transmission of vibrations [152, 153]. Although these methods have been reported by some groups as effective [152, 154], their application cannot ensure the absence of sensory response in TEPs. Firstly, because the level of noise masking might be insufficient in subjects that require higher stimulation intensities [155], and secondly, because at the moment there are no available means to avoid the TMS-induced peripheral electric stimulation.

Another possibility is the use of a sham condition with subsequent comparison of sham and active TEPs. The level of sophistication of the procedure ranges from stimulation of a different body part [156, 157] through active stimulation using a distanced or tilted coil [148] to custom-made sham coils that also integrate electric stimulation of the skin [150, 158]. While the simpler shams usually cannot completely match the sensation evoked by TMS, the new ‘realistic’ coils seem to perform sufficiently well. However, the electric pulse that these devices deliver to the scalp causes an EEG artifact lasting for a few tens of milliseconds, which completely overlays the earliest TEP components, thereby preventing their analysis [159].

It was recently proposed that PEPs could be separated from the genuine cortically evoked brain activity in an offline processing step using ICA [160]. The authors successfully identified and removed from the TEP signal a component that corresponded in its time-course and topography to the N100-P200 complex typically found in later AEPs. Since this so-called vertex potential can be also elicited by a variety of other sensory stimuli [161], taking out the associated artefactual component could reduce TEP contamination by both AEPs and SSEPs. Nevertheless, considering the high degree of temporal interdependence of all participating signals, the basic assumptions of ICA are likely violated, and its efficiency might be in this case reasonably questioned.

2.4.2. TEPs from the motor cortex

The frontal motor areas present a unique property that sets them apart from other cortical regions of the brain - in addition to cortico-cortical and cortico-thalamic circuits, the axons of local layer V pyramidal neurons form cortico-spinal connections through which they initiate and modulate

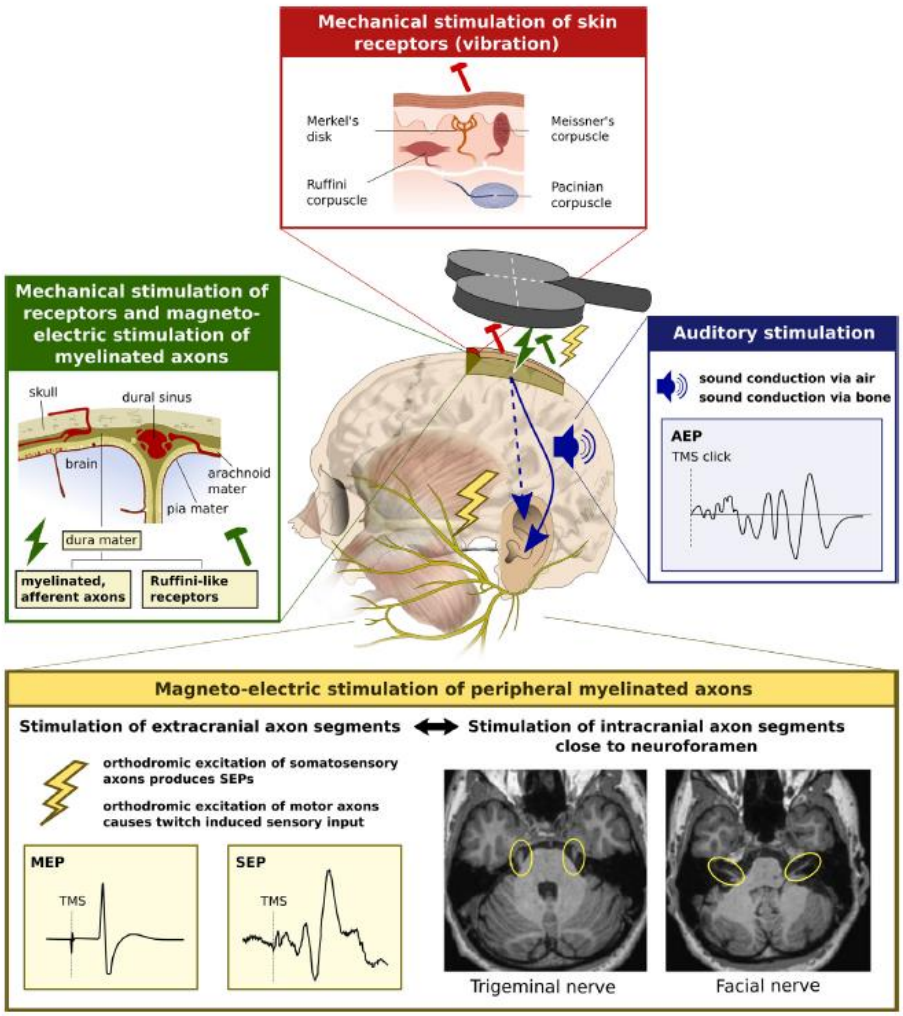

Figure 2.4 Peripheral sensory receptors and axons that can be stimulated by TMS and thus evoke sensory brain potentials contaminating TEPs. (A) The pressure, movement, or vibration of the TMS coil can activate local. **(B)** SEPs can occur following magneto-electric stimulation of afferent nerve fibres in the dura mater. **(C)** SEPs are typically elicited by magneto-electric stimulation of peripheral sensory axons, as well as by the muscle twitch triggered by the excitation of peripheral motor terminals. In addition, facial and trigeminal nerves can be activated at their passing through cranial foramina. **(D)** AEPs can be evoked by the high frequency clicking sound emitted when the electric pulse is discharged into the TMS coil. *source: Siebner et al., 2022 [55]*

muscular contractions and by consequence the movement [162, 163]. The M1, which occupies the Brodmann area 4, is considered as the main contributor to this descending motor pathway. It also contains most of the pyramidal cells synapsing directly to lower motoneurons, including the characteristic giant Betz cells [163, 164]. The functional organisation of the area generally follows the somatotopic representation of major body parts, although each of its subdivisions contains a distributed neuronal network that does not necessarily correspond to the peripheral anatomy and shows noteworthy activity-driven plasticity [165]. As such, the M1 certainly represents an exception rather than a typical example of cerebral cortex, both functionally and structurally. Yet, its outstanding properties made of this area the model target to study cortical reactivity to TMS, with findings often (most likely incorrectly) generalized to other brain regions.

Following a TMS pulse of a sufficient intensity, the pyramidal cells of the M1 generate a volley of action potentials that manifests as a contraction of the associated muscle (or a group thereof, depending on the size of the affected motor field). Intraspinal recordings from animals [166, 167] and later from awake human subjects [168-170] revealed that a supra-threshold stimulus to the M1 elicits a series of high-frequency (about 600 Hz) descending waves. While the earliest D-wave ('direct') likely reflects the direct depolarization of motoneuron axons, following I-waves ('indirect') have been attributed to the trans-synaptic activation of these pyramidal cells [171, 172]. The composition of the descending evoked response largely depends on TMS orientation and intensity and not all the waves are always necessarily present [67-69]. Importantly, a series of voltage deflections corresponding to D- and I-waves can be also recorded directly from the surface of the contracting muscle in a form of a MEP (Fig. 2.3F). This peripheral readout therefore represents a readily accessible measure of the response to TMS, which can provide valuable information about the functional state of the cortico-motor pathway [171]. Furthermore, the magnitude of MEPs can be conveniently used to localize the exact motor hotspot, thereby ensuring the optimal stimulation targeting [49, 107].

Because the combination of stimulation parameters clearly determines which neuronal populations of the M1 are preferentially affected by TMS, the threshold intensity for eliciting muscular activity varies accordingly. The lowest threshold values are typically obtained when the most impactful phase of the electric current induced in the brain is directed posterior to anterior (PA) across the central sulcus [67, 68]. This orientation has been therefore maintained by the majority of TMS studies targeting the M1. The motor threshold, defined as the minimal stimulation intensity required to elicit a reliable MEP of a certain amplitude, can be measured either at rest (rMT) or when the target muscle is pre-activated (aMT). Its value depends on subject's anatomy (the physical distance between the scalp and the cortical surface, the exact topographic organisation of motor areas, etc.) and on the overall excitability of the entire motor pathway, it is therefore highly specific for each individual. For

this reason, in both clinical and experimental settings, the final stimulation intensity is usually determined relative to r/aMT [49].

The extensive exploration of MEPs significantly broadened our knowledge of the motor system function (for review see [173]). Nevertheless, because this measure depends on the current condition of all central and peripheral components of the cortico-motor pathway, it cannot be used to evaluate neither of them separately. In this aspect, TEPs represent a more informative readout, as they can be directly linked to the state of motor cortices. Since the original paper published more than two decades ago [110], an impressive number of studies focused on the supra-threshold single-pulse M1 TEPs. They consistently described a sequence of stable TEP components that were labelled N15, P30, N45, P60, N100, P180 and N280 according to their dominant polarity (P = positive, N = negative) and peak latency (for example [118, 139, 159, 174-178])[2] (Fig. 2.5).

Based on the results of experimental manipulations complemented by source localization, individual components of M1 TEPs have been associated with the activity of specific brain regions. The peak N15, in the sensor space defined by a negativity at the site of stimulation, was attributed to the output of the stimulated cortex [119, 130, 179, 180]. Although potentially providing precious information, its isolation is technically challenging due to the proximity to the TMS artefact and it was therefore explored only by a few of the past studies. The following peak P30, characterized by a more central positivity, is thought to reflect an excitatory response [181, 182], although no consensus has been made regarding the location of its sources [130, 175, 179]. Both N15 and P30 were previously found correlated to the size of MEPs [180] and abolished following the use of non-optimal stimulation parameters [176]. Therefore, these earliest components possibly correspond to the genuine brain activity directly triggered by TMS in the targeted motor network.

The significance and origin of later TEP components is less clear. Firstly, in line with the conduction velocity of peripheral nerves, components occurring after approx. 40 ms post stimulus are potentially susceptible to the contamination by re-afferent somatosensory signals from the contracting muscles. In fact, a connection was previously made between this sensory response and the TEP component P60 [118, 183], while its link to other peaks cannot be excluded either. Secondly, it has been reported that the contribution of PEPs to the TEP signal increases with time and becomes significant already at latencies around 60 ms [184, 185]. Therefore, it is highly probable that all the later TEP peaks are generated by multiple brain processes occurring in parallel, and so their relevance to the direct activation of the motor network remains uncertain.

[2] Several earlier peaks were also previously reported (see reference 242) as would be expected considering the speed of neuronal synaptic transmission, however this TEP activity is usually too difficult to isolate due to the presence of TMS-related artifacts and will not be further discussed in this manuscript.

The peak N45, with a bipolar topography negative anterior on the contralateral hemisphere and positive posterior on the stimulated hemisphere, has been previously related to the balance of inhibitory $GABA_A$ergic and excitatory glutamatergic neurotransmission [186-188]. It was also suggested that this component might correspond to the inhibition of the sensorimotor area [174], which would be in line with its estimated source in the central sulcus [116]. The following peak, P60, shows a spatial distribution similar to N45 and seems to be at least partially generated by excitatory glutamatergic activity [187]. By contrast, the peak N100 corresponds to a widespread negativity maximal at fronto-central channels of the stimulated hemisphere, and is likely at least partially generated by inhibitory processes mediated by $GABA_BRs$ [186]. It reflects, at least partially, the excitability of motor cortices, as its magnitude was reportedly modulated by movements of the target limb [147, 189, 190] and correlated with the duration of the cortical silent period [191]. Moreover, some studies reported its association to the MEP amplitude [174, 192]. Finally, the last two described peaks, P180 and P280, are characterized by a widespread central positivity and appear to mostly reflect PEPs [155, 178].

In contrast to supra-threshold TMS, EEG responses evoked by sub-threshold M1 stimulation have been less investigated. In past, several studies recorded M1 TEPs using the threshold intensity (100% rMT) with the intention to reduce the potential influence of the re-afferent sensory input from the contracting muscles [187, 193, 194]. However, by definition, such stimulation still evoked a (small) MEP in approximately half of the trials, so the topographic features of observed TEPs were expectedly highly similar to those evoked by supra-threshold pulses. Nevertheless, reports of the few groups that applied clearly sub-threshold pulses indicate that the spatiotemporal profile of M1 TEPs strongly depends on the stimulation intensity, with distinct features reflecting the specific level of motor network engagement as well as the presence of the re-afferent signals [44, 118].

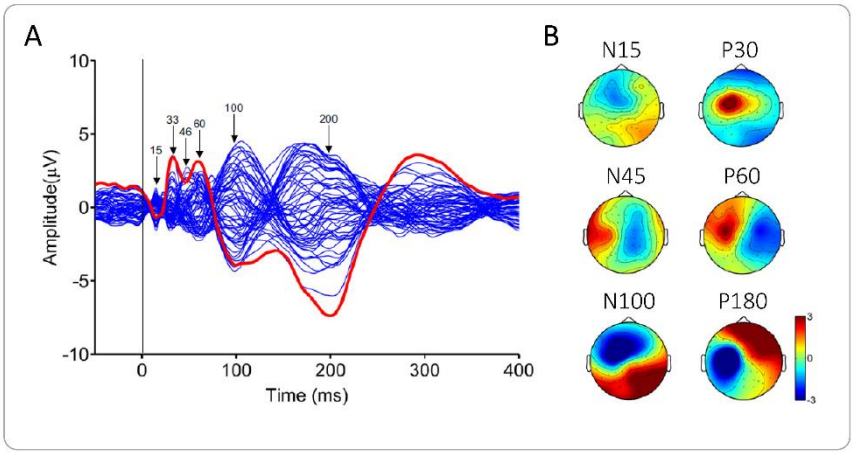

Figure 2.5 Supra-threshold M1 TEPs. **(A)** The butterfly plot of a group average TEP evoked by stimulation of the left M1 (30 subjects). Peak latencies are indicated by arrows, the red trace highlights the signal from the electrode C3 in the proximity of the site of stimulation. **(B)** Topoplots associated to each TEP component *source: Rogasch et al., 2014 [134]*

2.4.3. TEPs from non-motor cortical areas

With the increasingly common use of TMS-EEG, numerous research groups ventured beyond the M1 in order to describe the functional properties of 'silent' (non-motor and non-sensory) cortical areas that are otherwise hardly accessible in healthy awake subjects. However, the stimulation of such regions comes with multiple challenges, the most obvious being the identification of the stimulation site itself. Unlike in the motor cortex, the precision of TMS targeting cannot be verified by the magnitude of recorded MEPs, so the researchers must rely on anatomical landmarks or functional MRI localization, either based on individual data or available atlases. The choice of the optimal stimulation parameters represents another difficulty related to the absence of a known measurable output. Considering the exact placement of the coil, the best current practice is to direct the induced electric current perpendicularly to the longitudinal axis of the targeted gyrus (or, more precisely, to the corresponding sulcus), presumably to most efficiently activate the pyramidal cells in sulcal walls [66, 195]. Alternatively, the optimal coil position can be estimated using MRI-based models of the maximal induced E-field [78, 79]. Finally, when it comes to the strength of stimulation, it seems natural to opt for intensities comparable to the supra-threshold stimulation of the M1. For this purpose, the individual value of rMT can be adjusted according to the depth of the target cortical area [196], or its estimated E-field may be reproduced using MRI-based E-field simulation [197]. Nevertheless, it must be emphasized that even if the final stimulation strength perfectly corresponds to the one used in the M1, its effect is still difficult to predict due to the (mostly unknown) structural and functional differences of individual cortical sites. This is well illustrated for example by the lack of correlation between rMT and the threshold to evoke phosphenes following the stimulation of visual cortex [198].

Despite all the technical difficulties, an impressive number of studies managed to record TEPs following the stimulation of non-motor cortical areas. The dorsolateral prefrontal cortex (DLPFC) represents the most frequent target besides the M1, the quantity of publications ([199-202] to name a few) already allowing to describe a typical profile of DLPFC TEPs. Although this is not yet possible for other cortical regions, clear TEPs have been successfully obtained after the stimulation of various parts of the parietal cortex [200, 203, 204], premotor cortex [205-207], occipital cortex [44, 157, 208, 209] and cerebellum [136]. Taken together, these reports showed that TEPs from non-motor areas tend to have a lower amplitude than M1 TEPs and their spatiotemporal and oscillatory features considerably vary across stimulation sites. Moreover, studies that specifically compared TEPs from different cortical areas repeatedly concluded that while the early components (until 60 – 80 ms post stimulus) seem to be target specific, the later TEP peaks are highly similar across tested sites [114, 184, 200].

2.4.4. TEPs from the angular gyrus

The angular gyrus (AG), or Brodmann area 39, lies in the posterior apex of the inferior parietal lobule, right at the junction of parietal, occipital, and temporal lobes. It forms a horseshoe shape surrounding the upper part of the superior temporal sulcus (upper STS, otherwise angular sulcus) but its morphology and anatomical delimitation are highly variable both across individual subjects and between hemispheres [210]. It is also one of the last regions to develop in the maturing human brain and shows the greatest expansion when compared to brains of non-human primates [211, 212]. Based on its cytoarchitecture, the AG can be subdivided into two distinct areas labelled PGa (located anterior-dorsally) and PGp (posterior-ventrally), as visualized in Fig. 2.6 [213, 214]. These sections also differ in their structural and functional connectivity. While PGa forms stronger connections to the caudate nucleus, the frontal pole, and the cingulate gyrus, PGp preferentially projects to the adjacent occipital cortex and to bilateral parahippocampal and hippocampal gyri [215-218].

Functionally, the AG belongs to the polymodal association parietal cortex [219] and represents one of the connective hubs of the human brain [220, 221]. As such, it participates in a broad range of processes where it seems to act as the interface between the concrete and the abstract (for a review see [222]). It integrates multisensory inputs and mediates the classification and conceptualization of perceived information [222-224], thereby contributing to multiple high-order cognitive functions such as episodic and semantic memory [225], attention [226], or spatial orientation [227]. In agreement with its structural heterogeneity, PGa and PGp seem to attend to different functions attributed to the AG. Furthermore, the region shows considerable lateralization, which corresponds to its inter-hemispheric variability [228]. For example, the cortical activity associated with episodic retrieval is mostly observed in the posterior left AG, whereas attentional reorientation is rather linked to the activation of the anterior right AG [222, 229]. Importantly, the AG of both hemispheres – or rather its posterior-ventral part – also constitutes one of the core nodes of the default mode network (DMN), a collection of large-scale subnetworks mediating internally-driven mental processes [230-232].

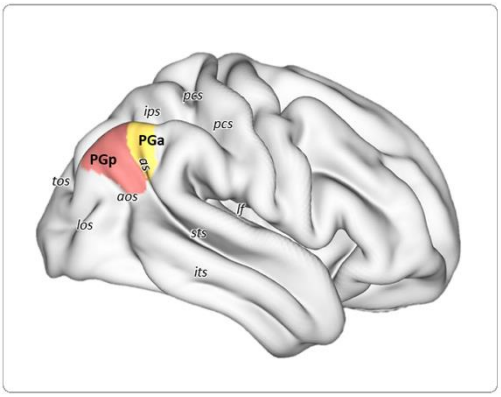

Figure 2.6 Anatomical localization of the angular gyrus. 3D model of the right hemisphere of the human brain shows the average location of the two sub-regions of the AG: PGa is marked in yellow, PGp in red. Abbreviations: *pcs* – post-central sulcus, *as* – angular sulcus (= ascending part of the superior temporal sulcus, *sts*), *ips* – Intraparietal sulcus, *lf* – lateral fissure, *its* – inferior temporal sulcus, *aos* – anterior occipital sulcus, *los* – lateral occipital sulcus, *tos* – transverse occipital sulcus, *cs* – central sulcus, *pos* – parietal-occipital sulcus.
source: Niu et al., 2022, Brain Structure and Function

Its widespread involvement in cognitive processing combined with its accessible location at the lateral surface of the hemisphere make of the AG a promising TMS target. Indeed, TEPs recorded following the AG stimulation might provide information about the functional state of this versatile region and potentially about DMN as a whole. However, only a few TMS-EEG studies to this date focused on the AG specifically, which can be possibly explained by the substantial technical difficulties that TMS of this region presents. It has been clearly shown that the coil placement and orientation determines the presence and magnitude of TMS-evoked muscular contractions, with more lateral positions resulting in higher occurrence of the associated EEG artefact [141]. Because of the anatomic location of the AG, its stimulation requires a posterio-lateral coil placement that is likely to evoke noticeable twitches of temporal and masseter muscles lying under the coil wings, which contaminate resulting TEPs and can cause discomfort to the subject. Furthermore, the precise localization of the target is often challenging, considering the morphologic variability of the AG and its functional heterogeneity mentioned earlier.

In general, parietal stimulation seems to yield TEPs of lower amplitudes as compared to the M1 or other non-motor cortical areas [123, 184, 200, 233], which has been sometimes interpreted as an overall lower excitability of the parietal cortex. This is in line with the finding that complex association cortices with highly variable intrinsic circuitry (such as the regions forming DMN) are less reactive to electrical stimulation than unimodal sensory areas [234]. Nevertheless, all previous studies targeting the AG were able to record clear TEPs using a range of TMS intensities comparable to M1 stimulation [114, 160, 184, 235, 236]. Considering the low number of publications and the variability of stimulation parameters each research group used, it is not yet possible to describe a 'typical' AG TEP. Especially at early latencies, each publication reports different spatiotemporal features of observed components (if they are described at all): while Ross et al. observed an early (~15 ms) bipolar component with a maximum at the site of stimulation [160], Dhami et al. found a component with a similar distribution that peaked around 30 ms [236], whereas Freedberg et al. reported a centro-posterior negativity at latencies between 20 – 60 ms [184]. As expected, the later components mostly resembled the typical vertex potential of PEPs. Interestingly, Ozdemir et al. recently succeeded to locate the sources of AG TEPs in different nodes of the stimulated DMN and to contrast these findings to TEPs from the superior parietal cortex, which mainly originated from nodes of the dorsal attention network [235]. Although coming from an isolated study, these results further confirm the potential utility of AG TEPs.

2.5. Using TEPs to evaluate $GABA_AR$-mediated inhibition

As established in the first introductory chapter, the dynamic equilibrium between excitatory and inhibitory neurotransmission is indispensable for a proper function of brain networks. An impairment of either of those systems, pre- or post-synaptic, may severely perturb E/I of a given neuronal circuit

and lead to its malfunction. Considering the functional specialisation of the interneuron minority and the prominent role the inhibition plays in the regulation of cortical processing, it becomes clear that even a small defect of the inhibitory transmission – and particularly of the fast synaptic inhibition mediated by $GABA_A$Rs – may have devastating consequences. In line with such assumption, multiple neuropsychiatric disorders have been linked either to a deficiency of inhibitory interneurons [38, 237, 238] or to alternations in $GABA_A$R expression and function [239-242]. However, the majority of these findings came from experiments using cellular cultures, animal models or post-mortem human tissues. In fact, until recently, only little was known about the functional state of $GABA_A$R-mediated inhibition in a living human brain. This gap is now slowly being bridged, as the rapid development of TMS-EEG finally provided an easily applied, non-invasive tool for the evaluation of human cortical excitability.

TEPs, or at least some of their components, reflect the strongest and most synchronous elements of the direct neural response to the stimulation. Yet, the electric currents generating these signals can be more or less dependent on the $GABA_A$ergic neurotransmission. Therefore, in order to use TEPs to evaluate the efficiency of inhibition within the investigated – local or large-scale – network, it is first necessary to identify the components that are sensitive to changes in the inhibitory signalling. To this end, the level of $GABA_A$Rs-mediated transmission can be experimentally modulated using different approaches, some of which are described in the following sections of this chapter.

2.5.1. TEPs and pharmacological modulation of $GABA_A$Rs

$GABA_A$Rs consist of five protein subunits forming a transmembrane channel for chloride ions. The most common $GABA_A$R subtypes are composed of two α, two β, and one γ class subunit, and each subunit class comes in multiple possible variants (α1–6, β1–3, and γ1–3) that bestow different qualities to the final receptor complex. The specific composition of $GABA_A$Rs determines their functional properties as well as their distribution across the brain and within individual cells. For example, α1β2γ1 receptors, which represents about 60% of all $GABA_A$Rs, are located at the soma and dendrites of various types of cells throughout the whole brain. By contrast, receptors containing the α5 subunit constitute only around 5% of $GABA_A$Rs and are mostly expressed at dendrites of pyramidal cells in the hippocampus [243-245]. Because of their structural heterogeneity, it is possible to pharmacologically target specific $GABA_A$R subtypes and thereby preferentially influence the inhibitory neurotransmission in specific brain regions.

Apart from two GABA binding sites, the $GABA_A$R complex usually features a site that binds benzodiazepines (BDZ) (it can be found in all subtypes except those containing the α4 subunit). BDZs act as positive allosteric modulators by increasing the total conduction of the chloride channel without changing receptor's affinity to GABA [246]. Profiting from their well-known mechanism of action and good tolerability, BDZs have been previously used in combination with M1 TEPs with the aim to identify

the components generated by the $GABA_AR$-mediated inhibitory transmission. In two separate studies, Premoli et al. observed that BDZs (alprazolam or diazepam) significantly increased the amplitude of the peak N45 and reduced the amplitude of N100 [186, 194]. In addition, the group tested the effect of zolpidem, a drug that preferentially interacts with the BDZ site at α1 $GABA_ARs$ [247], and described a similar increase in N45 without any effect on N100. In agreement with these findings, another study reported an increase of N45 following the administration of a selective α5 $GABA_AR$ antagonist [188]. Therefore, it seems that N45 and N100 of M1 TEPs reflect (besides other brain processes) the synaptic inhibition mediated by $GABA_ARs$, and the magnitude of these components could be potentially used to assess the efficiency of the $GABA_A$ergic neurotransmission within the sensorimotor network.

2.5.2. Short-latency intracortical inhibition

Early TMS studies revealed that the magnitude of MEPs evoked by the stimulation of the M1 can be substantially reduced if a sub-threshold conditioning stimulus (CS) precedes by a couple of milliseconds the supra-threshold testing stimulus (TS) [248-250]. As only later descending I-waves were found suppressed [251, 252], the effect of CS was attributed to SICI exerted by local interneurons. Correspondingly, it has been previously shown that a weak M1 stimulation that normally doesn't evoke any motor response still reliably activates local inhibitory circuits [253]. More recently, a study that explored morphologically realistic models of neuronal circuits in the precentral gyrus reported that axonal terminals of local pyramidal cells have the lowest threshold for TMS [66]. Based on these results, it was proposed that the low-intensity CS might preferentially stimulate the excitatory cells residing in the supplementary motor area, which would then use intercortical feedback loops to activate neighbouring interneurons, thereby inhibiting the motor network and lowering its reactivity to the subsequent TS [57]. Alternatively, the model indicated that certain interneuron populations, such as the basket cells in the lamina IV, might be also sufficiently excitable to be directly recruited by CS [66]. Whatever is the exact chain of events, the brief interstimulus interval (the inhibition is most pronounced if the stimuli are separated by 1 or 2.5 ms [254]) indicated that SICI is likely mediated by the fast synaptic $GABA_A$ergic neurotransmission [255]. This was subsequently confirmed by pharmacological studies showing that BDZs increase the extent of MEP SICI [256, 257] and suggesting that its effect might specifically depend on $GABA_AR$ subtypes bearing α2 or α3 subunits [258].

In the past years, several studies investigated the manifestation of SICI in M1 TEPs with the aim to further characterize the intracortical inhibitory mechanisms within the motor network [44, 174, 194, 259-261]. Yet, their findings are often inconsistent, which likely reflects the considerable variability in the experimental design and used analytical methods. While the earliest study by Paus et al. didn't report any TEP effect of SICI [174], Ferreri et al. found an increase of N100 and a suppression of P60 and P180 [260], whereas Cash. et al observed a decrease in the earlier components P30-P60 [259], and

Rawji et al. reported a reduction of peaks N15, P60 and P180, plus an increase of N45 [261]. Finally, two other independent studies (employing completely different methodology) only observed a SICI-related reduction in later TEP components, namely N100 and P180 in case of Premoli et al. [194] and N100 and P280 in case of Raffin et al. [44]. Taken together, these heterogenous results prove that – in contrast to the straight-forward amplitude reduction described in MEPs – the TEP signature of SICI is more complex and may even change depending on the chosen stimulation parameters.

One of the main advantages of TMS-EEG is the possibility to venture beyond the motor cortex and use TEPs to evaluate the properties of other cortical areas inaccessible through MEPs. However, to this day, only two groups applied the SICI protocol outside of the M1 [44, 259, 262] and both focused on the DLPFC (Raffin et al. additionally investigated SICI in the superior occipital lobe). Although, expectedly, their reports of the absolute TEP modulation vary, the studies clearly showed that the effect of this paired-pulse TMS protocol is specific for each stimulation site [44, 259], a finding likely reflecting the differences in local cytoarchitecture and excitability. Furthermore, it has been suggested that – on top of all the already mentioned factors – the age of subjects might also substantially influence the TEP readout of the paired-pulse stimulation [262]. Therefore, it seems that a thorough evaluation of structural and functional properties of each cortical target is necessary in order to identify the optimal stimulation parameters that would allow to measure SICI in the target cortical area and its connected brain network.

2.6. Summary of aims and objectives

In this dissertation, presented as a collection of publications, we investigated the significance of TEPs and their utility as non-invasive biomarkers of cortical excitability in specific brain regions, namely the M1 and the AG. The aim was to (1) evaluate the contribution of PEPs to the TEP signal by comparing TEPs from these two distinct cortical areas and by comparing M1 TEPs evoked by sub- and supra-threshold stimulation intensity (chapter 3); (2) to determine the significance of individual TEP components by describing the TEP signature of increased inhibitory neurotransmission induced both pharmacologically and with paired-pulse TMS to elicit SICI (chapters 4 and 6); and (3) to characterize in detail the spatiotemporal profile of AG TEPs, to identify the optimal stimulation parameters for their recording, and to determine the AG TEP components of interest (chapter 5).

3. Investigating the origin of TMS-evoked brain potentials using topographic analysis

3.1. Abstract

The combination of TMS and EEG represents an increasingly popular tool to non-invasively probe cortical excitability in humans. The resulting TEPs are composed of several successive components reflecting the propagation of activity from the site of stimulation, thereby providing information on the state of brain networks. However, TMS also generates peripherally evoked sensory activity which contributes to TEP waveforms and hinders their interpretation.

In the present study, we examined whether topographic analysis of TEPs elicited by stimulation of two distinct cortical targets can disentangle confounding signals from the genuine TMS-evoked cortical response. In 20 healthy subjects, TEPs were evoked by stimulation of the left M1 and the left AG. Topographic dissimilarity analysis and microstate analysis were used to identify target-specific TEP components. Furthermore, we explored the contribution of cortico-spinal activation by comparing TEPs elicited by stimulation below and above the threshold to evoke motor responses.

We observed topographic dissimilarity between M1 and AG TEPs until approximately 80 ms post-stimulus and identified early TEP components that likely reflect specific TMS-evoked activity. Later components peaking at 100 and 180 ms were similar in both datasets and attributed to sensory-evoked activity. Analysis of sub- and supra-threshold M1 TEPs revealed a component at 17 ms that possibly reflects the cortico-spinal output of the stimulated area. Moreover, supra-threshold M1 activation influenced the topography of almost all later components. Together, our results demonstrate the utility of topographic analysis for the evaluation and interpretation of TMS-evoked EEG responses.

3.2. Introduction

The combination of TMS and EEG is becoming an established tool in experimental and clinical brain research, and for good reasons. While TMS allows to non-invasively depolarize a selected cortical target to provoke its transient activation [46, 50], the excellent temporal resolution of EEG makes it possible to capture in real time the spread of the evoked activity across the cerebral cortex [107, 108]. TEPs recorded with EEG are composed of a sequence of deflections in scalp voltage that are time-locked to the stimulus, each of its successive components representing an epoch of synchronous activation of a large number of neurons. Such activity corresponds to the immediate brain response to the direct cortical stimulation, making TEPs a unique tool to probe the functional properties of individual brain structures and networks. Specific characteristics of TEP components, such as their amplitude, latency and voltage scalp distribution, can provide information about the strength of the TMS-evoked cortical response, the location of the sources generating this response and, consequently, the functional connectivity across the TMS-activated cortical network [124, 127].

However, several issues must be tackled in order to decipher the information held by TEPs. First of all, it is now widely recognized that TEPs reflect several parallel processes of heterogenous origin. In addition to the genuine TMS-evoked cortical activity, they also include somatosensory and/or auditory-evoked activity related to the fact that TMS pulses unavoidably activate a range of sensory receptors [150, 177, 263]. This presumed peripheral contribution to TEPs received much attention in recent years, culminating with a paper of Conde et al. [150] that compared brain responses elicited by active TMS and realistic sham stimulation. The group reported high similarity of both evoked potentials, suggesting that TEPs predominantly reflect sensory-evoked brain activity. Although their findings have been widely disputed [264] and multiple research groups have since striven to prove that TEPs do contain measurable TMS-evoked cortical activity [154, 178, 184], it still indicates that the functional significance of each identified TEP component must be carefully considered.

The situation further complexifies when it comes to TEPs evoked by stimulation of the M1. In any other cortical area, TMS leads to the activation of corresponding cortico-cortical and cortico-thalamic circuits. While this is also true for sub-threshold M1 stimulation, supra-threshold stimulation of the area causes an additional excitation of the cortico-spinal tract that provokes a contraction in the target muscle. This peripheral event can be easily registered as a MEP, which then represents a readily available measure of the overall motor pathway excitability. Unsurprisingly, this outstanding property of the M1 has made it the most popular cortical target for TMS application. However, the muscular contraction evoked by M1 stimulation elicits an additional time-locked, re-afferent somatosensory brain response that is mixed in the resulting TEP [116, 158], thus complicating its interpretation.

Finally, assuming that one successfully identifies a set of TEP components that can be linked to the cortical process of interest, yet another challenge arises during analysis. Like any other type of event-related brain potentials (ERPs), TEPs are most often evaluated in the time domain where the amplitude and latency of individual peaks represent the principal measured variables. Summarizing the TEP waveform as a series of peaks offers the advantage of substantially reducing the number of considered variables, but it usually requires prior knowledge on the time course and topographic distribution of the elicited responses to allow the preliminary selection of channels and time windows of interest.

Another way to evaluate ERPs, proposed by Murray et al. (2008), is to consider the temporal evolution of scalp topography of the evoked response rather than its amplitude. This approach is based on the notion that the potentials recorded at the scalp reflect the momentary state of global neuronal activity, with all simultaneously active sources contributing with different weights to the signal recorded by each electrode [265]. It implies that two different topographies recorded from the same subject represent the activation of two distinct sets of cortical sources [266]. Therefore, by searching for topographic differences across time and experimental conditions, it is possible to identify time

intervals of differential cortical activity in a purely data-driven fashion. Topography can be also compared across timepoints within a single dataset in order to identify clusters corresponding to the period of activity of a certain set of sources. This approach, known as microstate analysis (for review see [267, 268], stems from an early study [269] that identified short intervals of quasi-stable topographies – microstates – in the resting-state EEG. It was later suggested that microstates might represent the building blocks of information processing [270]. In evoked potentials, microstate segments are closely aligned to observed ERP components and are thought to correspond to a sequence of discrete processing steps triggered by the stimulation [271].

To our knowledge, neither analysis of topographic similarity nor microstate analysis are commonly used to characterize TEPs, despite several non-negligible strengths of these methods. By including the whole set of channels in the form of a single multidimensional vector, a statistics-based topographic analysis avoids the necessity to arbitrarily choose regions of interest. Moreover, by considering the voltage landscape as a whole, this approach effectively deals with the bias introduced by the choice of the reference electrode. The placement of reference inevitably influences the scalp voltage amplitude [272, 273] and by consequence the character of differences observed between tested conditions, as was elegantly illustrated by Murray et al. [271].

TMS pulses delivered over two different cortical targets can be expected to elicit cortical responses that differ at least partly in terms of activated cortical networks. However, the stimulation is also likely to evoke a set of unspecific cortical responses due to the activation of highly distributed connections, as well as the concomitant triggering of somatosensory- and auditory-evoked responses. Furthermore, varying the intensity of the TMS pulse can be anticipated to differentially modulate the magnitude of these different response components, and this effect might be especially remarkable when stimulating the M1, depending on whether the stimulus activates the cortico-spinal tract. In the present study, we tested whether topographic analysis of TEPs elicited by stimulation of two distinct cortical targets, namely the M1 and the AG, or using two distinct stimulation intensities (M1 stimulation below and above the threshold to elicit MEPs) can be used to disentangle target-specific and target-unspecific components of TEPs and, thereby, gain information on the properties of the cortical networks activated by TMS.

3.3. Materials and Methods

3.3.1. Ethical approval

All experiments were conducted according to the latest revision of the Declaration of Helsinki. The protocol and all procedures were approved by the local Ethical Committee (Commission d'Ethique Biomedicale Hospitalo-Facultaire). All participants were thoroughly informed of the protocol and

applied procedure, gave a written informed consent before taking part in any experiment, and were financially compensated for their participation in the study.

3.3.2. Participants

20 healthy right-handed volunteers (10 males, mean age 24) took part in the study. All participants filled a detailed questionnaire and undertook a brief neurological examination to exclude candidates with any contraindication for experimental procedures, such as epilepsy (or familiar history thereof), presence of metal in the body (e.g. insulin pump, pacemaker, metal prothesis), known neurological pathology relevant to the study and use of medication alternating cortical excitability [274].

3.3.3. Experimental design

The data analysed in the present study corresponds to two baseline datasets acquired in a larger study assessing the pharmacological modulation of TMS-evoked potentials (TEPs). The baseline datasets were acquired in two sessions separated by at least one week, conducted in the morning while keeping onset times as similar as possible for each subject. The subjects were asked to sleep sufficiently and refrain from alcohol consumption on the night prior to the experiment, and to avoid caffeinated beverages in the morning before the experiment.

TEPs were recorded following TMS stimulation of the left (dominant) M1 and the left AG. TMS pulses delivered over the M1 were delivered using both a sub-threshold and a supra-threshold stimulation intensity, the latter evoking clear motor contraction in the target muscle, monitored using a surface EMG recording.

3.3.4. EEG recording

The EEG was recorded using a NeurOne EEG system (Bittium NeurOne Tesla; Bittium Corporation, Oulu, Finland) and a 32 channel EEG cap mounted with TMS-compatible Ag/AgCl electrodes (EasyCap GmbH, Herrsching, Germany). The signal was referenced to both mastoids and recorded at a 20 kHz sampling rate with a 5 kHz low-pass filter and DC filter. Electrode impedances were kept below 5kΩ.

A thin layer of plastic was placed over the electrodes and subjects wore an extra rubber cap on top to minimize artifacts caused by the direct contact of electrodes with the TMS coil, and to reduce the bone conduction of the vibration generated by the TMS stimulation. In addition, during the EEG recordings, subjects listened to a masking noise created from an original recording of the TMS click to further reduce possible auditory artifacts.

3.3.5. Neuronavigation and TMS

A 3D T1-weighted structural MRI image of each participant's whole brain was acquired beforehand at the Department of radiology of the Cliniques universitaires Saint-Luc (1×1×1 mm; 3 T Achieva; Philips Healthcare, Amsterdam, The Netherlands). A Visor2 neuronavigation system (Visor

2.3.3; Advanced Neuro Technologies, Enschede, The Netherlands) was used to verify the accurate placement of the TMS coil and to monitor its position throughout the experiment. A 3D model of the scalp and brain surface was reconstructed based on the individual MRI data and co-registered with the real space using landmark-based markers (nasion and tragi) and head-shape matching [275]. The positions of the subject's head and TMS coil were continually registered with a Polaris infrared optical tracking system (Polaris Spectra; Northern Digital Inc. Europe, Radolfzell, Germany).

Both cortical targets (M1 and AG) were identified on subject's brain model and their location was saved in the neuronavigation system to keep the stimulation sites identical across experimental sessions. The TMS pulses were delivered using a figure-of-eight TMS coil having an outer diameter of 75 mm (C-B60; MagVenture, Farum, Denmark), tangentially placed on the scalp and centred over the stimulation target. The stimulation consisted of biphasic pulses delivered manually using a MagPro X100 magnetic stimulator (MagPro X100 with MagOption; MagVenture, Farum, Denmark), inducing electrical current with anterior–posterior posterior–anterior (AP-PA) direction.

M1 stimulation. The stimulation target over the left M1 was defined as the most optimal position to elicit MEPs in the right first dorsal interosseous muscle (FDI). The optimal coil orientation was adjusted individually, with the handle always pointing laterally and posteriorly with an approximate 45° angle from the midline. The rMT was set to the minimal stimulation intensity eliciting MEPs with an amplitude of least 50 μV in at least 5 trials out of 10 [276]. The mean rMT (in % of maximum stimulator output ± SEM, standard error of mean) was 49.3 ± 1.4% and 49.8 ± 1.4% in the first and second experimental sessions, respectively. TMS over the M1 was delivered in three blocks of 60 stimuli with a random 4-6 s inter-trial interval while simultaneously recording EEG and EMG. Three categories of stimuli were applied in a semi-random order, with a total of 60 stimuli of each category (20 per block): (1) supra-threshold single TMS pulses at the intensity of 120% rMT, (2) sub-threshold single TMS pulse at the intensity of 80% rMT and (3) paired TMS pulses combining the two types of TMS stimuli. In this study, only TEPs elicited by single supra-threshold and sub-threshold TMS pulses were analysed.

AG stimulation. The stimulation target over the left AG was identified in the individual MRI based on the position of anatomical landmarks, including the Superior temporal sulcus and the Intraparietal sulcus. The coil was placed with the handle pointing downwards and approximately 10° towards the midline, in a position that corresponds to the orientation of the coil axis across the superior temporal sulcus and perpendicular to surrounding gyri. TMS was applied in a single block of 60 stimuli delivered at 100% rMT with a variable inter-trial interval (4 – 6s).

3.3.6. Pre-processing of the EEG data

The continuous EEG recordings were processed offline using Matlab (MathWorks, Inc., Natick, Massachusetts, United States), Letswave 6 (an open-source EEG/EMG signal processing toolbox, https://www.letswave.org/) and custom scripts. We generally followed the pipeline introduced by Rogasch [139]. The EEG signals were first re-referenced to the average of all scalp channels, the DC shift was removed and a linear detrend was applied. The data were cut into epochs from –1000 ms to 2000 ms relative to each TMS pulse. The large artifact caused by the TMS was removed and replaced using cubic interpolation between -5 and +10 ms, and the signal was down-sampled to the sampling rate of 2 kHz. The interpolation led to a complete removal of the artifact in the signal at most channels, however at some we could still observe a leftover tail of the TMS-evoked muscle artifact with a sharp front edge that could pose a problem for the frequency filter. For that reason, an Independent Component Analysis (ICA, FastICA algorithm [277]) was performed to remove components containing this sharp tail, and in this step epochs of all categories from one recording were concatenated and treated together. Data were then bandpass filtered between 0.1 and 80 Hz (Butterworth, 4^{th} order) and notch filtered at 50 Hz (FFT linear filter, notch width 2 Hz, slope cut-off width 2 Hz). In the next step, individual epochs were visually inspected to remove those containing excessive noise or isolated outbursts thereof. Any trial associated with a missed TMS stimulation (in case of an unexpected head movement causing the coil to slip etc.) was also discarded. On average, the final number of remaining epochs per stimulus category was 48 ± 7 (SD) and there were no significant differences between stimulation conditions.

A second round of ICA was then used to remove remaining non-neural artifacts such as eye blinks, horizontal eye movements, tonic muscle activity and electrode noise. Artefactual components were first identified automatically with the Multiple Artifact Rejection Algorithm (MARA), a linear classifier trained on adult EEG data [278]. The pre-selected components were evaluated based on their topography, time course, and power spectrum density (PSD) to remove only components with clearly artefactual origin. Eye blinks and horizontal eye movements were identified by their specific frontal topography, irregular onset and steep decay of the PSD with a high content of slow oscillations. Tonic muscular contraction was easily distinguished by its marginal topography, no remarkable time-locked activity and a high content of high frequency oscillations. Electrode noise was identified based on topography limited to a single channel, often associated with sudden high-amplitude voltage changes. This second ICA was also used to remove leftovers of the TMS artifact caused by TMS-induced contraction of muscles under the stimulation coil. These artifacts usually showed a bipolar topography in the proximity of ipsilateral temporal or neck muscles.

Since M1 and AG TEPs were recorded within the same stimulation blocks, the majority of above mentioned extra-cerebral artifacts were shared across both datasets. However, certain artifacts, such as the leftover activity due to the muscle contraction, were often specific for the stimulation site. For that reason, an ICA matrix was calculated for each target and the datasets were treated separately. To minimize the risk of introducing differences due to variations in the removal of these artifacts, we verified that the same number and type of common artifacts were removed from M1 and AG TEPs. It is also necessary to emphasize that we took great care not to discard components that were suspected to possibly include TMS-evoked cortical activity, such as topographically widespread changes in signal in the background of a localized artifact, or any component that displayed non-explainable time-locked activity in the average time course. Thus, the cleaned EEG signals most probably included some weak remaining artifactual signals.

As a last step, the EEG epochs were baseline corrected to the interval from 200 ms to 5 ms before the TMS pulse and averaged for each subject and condition.

3.3.7. TEP peak labelling

The TEP waveforms were evaluated within the time interval from 10 to 300 ms post-stimulus. For each stimulation type, individual components were first identified as the local maxima in the time course of the Global Field Power (GFP) that was calculated from the grand average TEPs. GFP corresponds to the standard deviation of voltage across all channels that can be plotted as a function of time (Equation 3.1). As such, it conveys information about the overall strength of time-locked TMS-evoked responses, which itself corresponds to the degree of synchronisation of TMS-evoked cortical activity [272]. The latencies of GFP peaks were extracted automatically and used to search for corresponding deflections in the signal recorded at the vertex electrode. TEP components were then named according to the polarity and approximate latency of these deflections, while keeping in line with the nomenclature established in the literature when possible.

3.3.8. Planned comparisons

To evaluate the effect of stimulation site, TEPs elicited by AG stimulation were compared to the TEPs elicited by sub-threshold M1 stimulation. This paired comparison was justified by the fact that sub-threshold TMS over the M1 does not evoke any contraction in the target muscle, and therefore does not trigger EEG responses related to the processing of recurrent somatosensory signals originating from the TMS-evoked contraction of the hand. TEPs elicited by sub-threshold M1 stimulation should thus be more comparable to TEPs elicited by stimulation of non-motor cortical areas such as the AG.

Then, we compared the TEPs elicited by sub-threshold M1 stimulation to the TEPs elicited by supra-threshold M1 stimulation, with the intention to disentangle the contribution of cortico-spinal activation and somatosensory processing to the M1 response.

For both comparisons, the datasets from the two experimental sessions were included and the factor *session* was added to the statistical analysis to control for possible test-retest variability.

3.3.9. Topographic analysis of TEPs

All steps of the topographic analysis were performed in Ragu, a free Matlab-based toolbox for the analysis of ERPs [279]. Ragu uses a multi-variate approach that considers the entire scalp voltage distribution and allows to make inferences about group differences based on randomization statistics. Our analysis pipeline followed the steps indicated in [280].

Test for outliers. Prior to any further analysis, compared datasets were tested for outliers. All subjects were represented in the form of a single vector composed of all available datapoints. Subjects with datapoints unlikely falling in a normal distribution were automatically identified based on the Mahalanobis distance between subjects [281] and excluded from further analysis.

Test for topographic consistency. A Topographic Consistency Test (TCT) of the TEPs was conducted for each session and each type of stimulus, and the obtained results were then combined across sessions. The TCT identifies time intervals that show strong topographic homogeneity across subjects. Changes in the TEP waveforms that are observed in these intervals can thus be reliably linked to an effect of the experimental manipulation on the TMS-evoked activity. Conversely, the TCT helps to avoid attributing any meaning to changes observed at times of excessive inter-individual topographic variability. The TCT implemented in Ragu uses the GFP of the group-level average TEP data as the quantifier, which is then tested for significance against an empirically obtained distribution of GFP values corresponding to the null hypothesis. This distribution was computed at each timepoint using 5000 permutations, with each iteration randomly scrambling the individual-level signal across all electrodes to create random topographies with a constant GFP and recalculating the group average.

Analysis of topographic similarity. To assess the degree of similarity between topographies of two TMS stimulation conditions (AG vs sub-threshold M1 stimulation; sub-threshold vs supra-threshold M1 stimulation), we used the measure of Global Dissimilarity (DISS, Equation 3.2) also introduced by [272]. DISS corresponds to the distance between two multidimensional vectors each representing one entire scalp voltage distribution across electrodes. The DISS value ranges between 0 (perfect topographic homogeneity) and 2 (complete topographic inversion). For each of the planned comparisons, a single value of DISS was obtained for each timepoint from the group-level averaged TEPs of the compared conditions. A point-by-point statistical randomization test was conducted to determine the time windows of significant difference between conditions. In Ragu, this procedure is referred to as a

Topographic Analysis of Variance (TANOVA), even though it is a non-parametric test unrelated to an analysis of variance (ANOVA). Indeed, the TANOVA computes for each time point an empirical distribution of DISS values under the null hypothesis by running 5000 cycles of randomly assigning individual TEP waveforms to the two compared conditions and re-calculating the DISS. The actual DISS values are then compared at each timepoint to the values from this empirical distribution, thus yielding a time-varying p value.

Finally, the p values obtained for each time point were corrected for multiple comparisons by applying a procedure named "Global Count Statistics", which compares the obtained number of sub-threshold p values with the count of sub-threshold p values in an empirically constructed distribution of p values under the null hypothesis. The level of significance was set to 0.05.

To further characterize observed topographic differences across conditions, mean scalp topographies were calculated per condition for each segment of statistically significant topographic dissimilarity. The voltage difference was compared at each channel and obtained t values were plotted as t-maps. These t-maps allow to visualize where and how much mean topographies differ by comparing the average difference to the variance across observations. Reported p values were obtained by averaging p values provided by TANOVA across all timepoints in each time interval.

Microstate analysis. A microstate analysis of the TEP waveforms was used to assess the temporal properties of observed topographic changes. The optimal number *n* of microstate classes was determined using the cross-validation method proposed by [282], as illustrated in the lower panel of Fig. 3.1. First, the average TEP waveforms of individual subjects were randomly split into a training and a testing dataset. Then, the average of training TEP waveforms was used to compute microstate models with the number of classes ranging from 3 to 12, and the mean spatial correlation C_i of each model with the average of the testing dataset was computed according to Equation 3.3. This process was repeated 50 times for variable subsets of the data. The C_i from all runs was averaged and compared across models to indicate the simplest one yielding the *C* value in the plateau range (the 'elbow position') and the corresponding *n* of microstate classes was retained for the subsequent microstate labelling and analysis.

The *n* class maps were identified in a dataset created by concatenating the group-level average TEP waveforms of compared stimulation conditions (this process is illustrated in the upper panel of Fig. 3.1). Each timepoint in each group-level average TEP waveform was then labelled with the class map that was most correlated with the momentary topography, thus segmenting the TEPs into non-overlapping intervals or microstates. For the purpose of this segmentation, we chose to use the k-means clustering algorithm [271] with 250 iterations. In each cycle, the algorithm drew *n* random template maps (topographies at *n* different timepoints) from the concatenated dataset and computed the spatial correlation *C* between each template and all the remaining topographies in the dataset. In

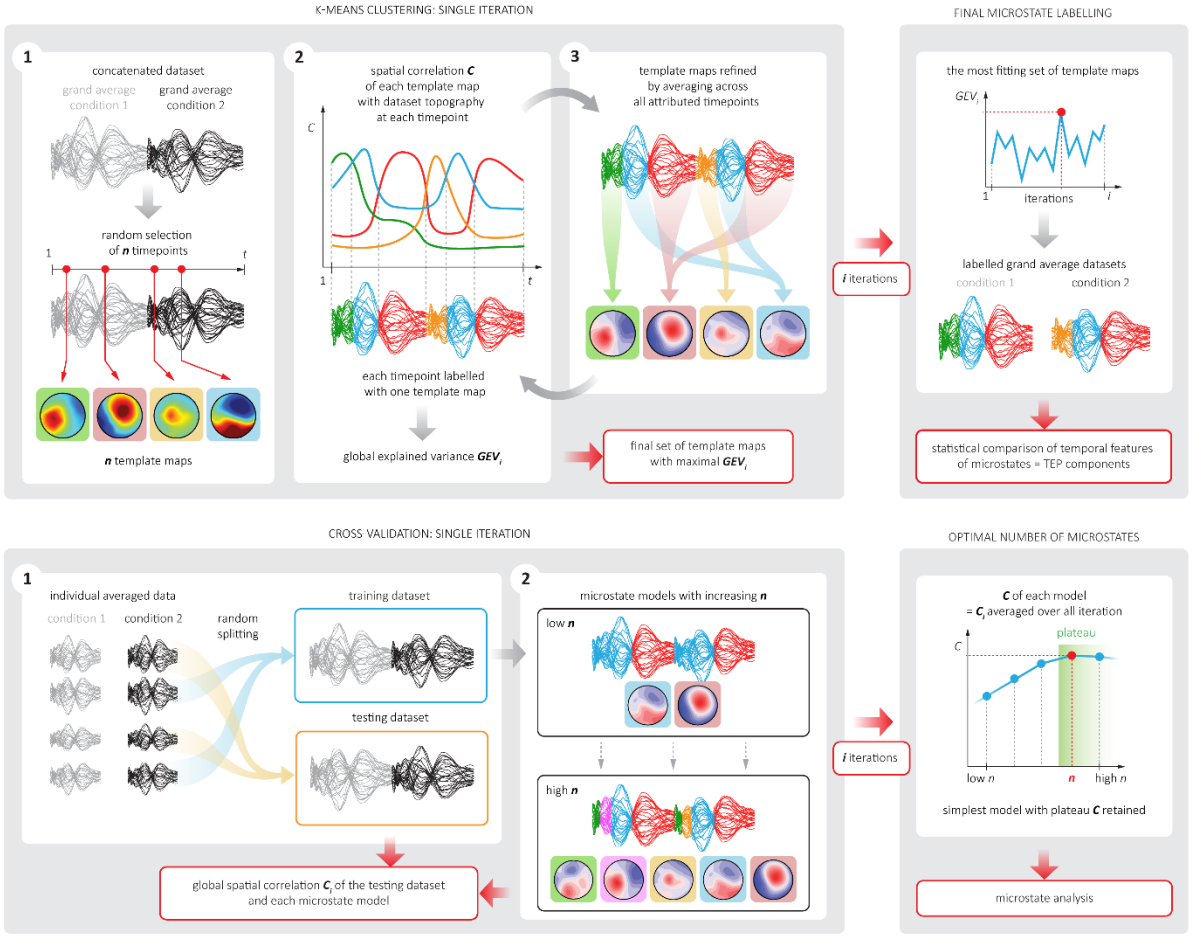

Figure 3.1 Microstate analysis. The upper panel: microstate labelling using k-means clustering algorithm. This process is applied at the level of grand average datasets. In a single iteration (left), a set of microstate class maps is obtained by randomly selecting template topographies of *n* timepoints (1), labelling all timepoints with a single template topography that yields the highest spatial correlation (2) and refining those templates by averaging all timepoints with the same label (3). Each refining cycle, the Global Explained Variance of the template set is calculated (GEV_i) and the set is considered final when no increase in GEV_i can be observed. Therefore, the outcome of one iteration is a set of refined template maps and an associated value of GEV_i. GEV_i obtained in all iterations is then used to identify the most fitting set of template maps, that model is retained, and statistics are computed based on the corresponding microstate labelling (right). **Lower panel: choosing the optimal number of microstate classes using cross-validation**. In a single iteration (left), individual averaged data are split to a training and testing dataset (1), the training dataset is used to prepare a range of microstate models with increasing *n* (using the process shown in the upper panel) (2) and global spatial correlation C_i is computed between each model and the testing dataset. C_i obtained in all iterations is averaged and the *n* of the simplest model yielding *C* in the plateau range is kept for the final analysis (right).

the next step, each timepoint in the dataset was labelled with the template map that yielded the highest *C*, and the Global Explained Variance GEV_i (Equation 3.4) was computed for the given set of templates. All template maps were subsequently re-defined by averaging topographies over all the timepoints labelled with the same template. *C* and GEV_i were re-calculated and the whole process was repeated until no additional increase in GEV_i was observed. Obtained GEV_i was then associated with the final, refined set of microstate class maps, and the next iteration of the clustering process began with yet another random sample of *n* topographies. Finally, the set of *n* class maps that yielded the highest overall GEV_i was retained and backfitted to the group-level average TEP waveforms.

The final microstate model labels every timepoint of the group-level average TEP waveforms with a single microstate class. Using this information, it is possible to compare temporal properties of those classes that are shared across compared datasets. To this end, we considered the following microstate features: (1) mean duration, (2) onset and offset and (3) centre of gravity. To compare these measures between conditions, we quantified the observed effect by computing the difference, in other words the variance, across conditions. Individual datasets were randomized with 5000 permutations to create the distribution of the given measure under the null hypothesis, and the original quantifier was compared to this distribution. The probability of the quantifier being compatible with the null hypothesis was computed as the proportion of trials in the whole empirical distribution that gained values larger than the quantifier.

$$GFP(t) = \sqrt{\frac{\sum_{j=1}^{n}(u_j(t) - \bar{u}(t))^2}{n}} \quad (1)$$

$$DISS_{u,v}(t) = \sqrt{\frac{1}{n} \cdot \sum_{j=1}^{n}\left(\frac{u_j(t)}{GFP_u(t)} - \frac{v_j(t)}{GFP_v(t)}\right)^2} \quad (2)$$

$$C_{u,v}(t) = \frac{\sum_{i=1}^{n} u_j(t) \cdot v_j(t)}{\|u\|(t) \cdot \|v\|(t)} \quad (3)$$

$$GEV = \frac{\sum_{t=1}^{tmax}(GFP_t \cdot C_{t,M_t})^2}{\sum_{t=1}^{tmax} GFP_t^2} \quad (4)$$

Equations 3.1 - Global Field Power GFP, **3.2 - Global Dissimilarity DISS, 3.3 - Spatial Correlation C, and 3.4 - Global Explained Variance GEV**. GFP, DISS and C are calculated for each timepoint t, whereas GEV averages across all timepoints. n is the number of electrodes, u_j and v_j represent the voltage measured at one electrode in two different conditions, while $\bar{u}$ is the mean voltage computed from all electrodes in a single condition. M_t stands for the class map attributed to the timepoint t.

3.4. Results

3.4.1. TEPs elicited by supra-threshold M1, sub-threshold M1 and AG stimulation

For each stimulation condition, clear peaks were observed in the TEP waveforms. These peaks differed in their topography and/or latency across stimulation conditions and showed variable topographic consistency.

In the TEP elicited by supra-threshold M1 stimulation, we identified a sequence of five highly consistent peaks that were labelled N17 (peak latency 17 ms), P30 (32 ms), P60 (57 ms), N100 (111 ms), and P180 (194 ms). Associated peak topographies are displayed in Fig. 3.2A. An additional peak was identified around 45 ms and labelled N45. The topography of N45 was masked by an overlapping P30-P60 complex but was nevertheless distinguishable as a negative deflection superimposed on the positive peak.

Five peaks were also identified in the TEP waveforms elicited by sub-threshold M1 stimulation: P30 (27 ms), N45 (46 ms), P60 (61 ms), N100 (118 ms) and P180 (184 ms). The TCT showed low topographic consistency between 10 and 21 ms, i.e. at latencies corresponding to the N17 observed following supra-threshold M1 stimulation. Low topographic consistency was also observed 33-50.5 ms,

which included the N45. The latencies of these peaks were very similar to the latencies of the peaks elicited by supra-threshold M1 stimulation. However, the peak voltage distribution of all peaks except the P30 visibly differed from that of the corresponding peaks for supra-threshold M1 stimulation, as shown in Fig. 3.2B.

In the TEP waveforms elicited by AG stimulation, 6 components were identified: P25 (21 ms), N40 (37 ms), P55 (55 ms), N75 (75 ms), N100 (114 ms) and P180 (192 ms). Peak topographies are shown in Fig. 3.2c. The TCT revealed topographic inconsistency in three intervals (10-13.5 ms, 26.5-32 ms and 38.5-52 ms), covering most of the duration of the N40 and P55 components.

3.4.2. Analysis of the topographic dissimilarity between sub-threshold M1 TEPs and AG TEPs

Prior the analysis, two outliers were identified and excluded. The DISS analysis identified three intervals of significant topographic dissimilarity between the TEP waveforms elicited by sub-threshold M1 stimulation vs AG stimulation. Since these time windows partially overlapped with intervals of topographic inconsistency identified in both datasets, the inconsistent intervals of both time windows were excluded from further analyses (Fig. 3.3A).

The first interval of significant dissimilarity (21.5-26 ms, $p < 0.001$) partially covered the P30 component of M1 TEPs and the P25 component of AG TEPs. The second interval (54.5 – 80.5 ms, $p < 0.001$) included the P60 component of M1 TEPs and the N75 component of AG TEPs. For both intervals, the M1 TEP topography featured a positive maximum at left central electrodes, whereas the AG TEP

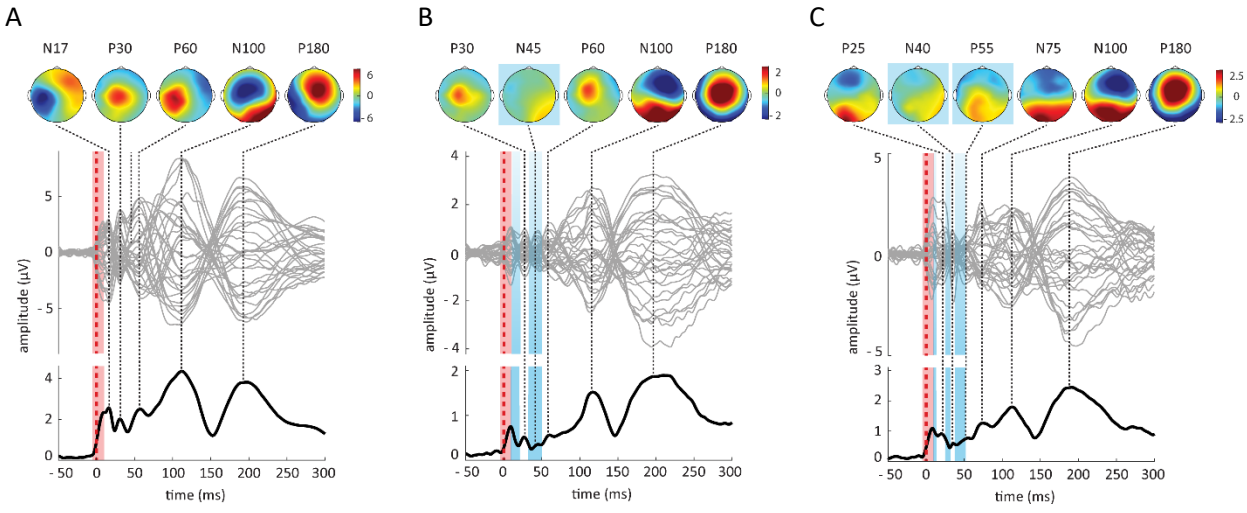

Figure 3.2 TEPs evoked by (A) supra-threshold stimulation of the M1, (B) sub-threshold stimulation of the M1 and (C) stimulation of the AG. In the centre, the butterfly plots show the signal from all analysed electrodes averaged across subjects and experimental sessions. Red dotted lines mark the TMS stimulus, light pink areas indicate the time interval interpolated following the removal of the TMS artifact. The GFP of the signal is plotted in the lower section, its local maxima indicating (dotted lines) the peak latencies of identified TEP components. Areas shaded in light blue correspond to the intervals of topographic inconsistency. In the upper section, the topographies extracted at peak latencies are associated with TEP components, except for N45 in the supra-threshold M1 TEP (panel a, indicated only with the dotted line). Light blue squares around certain topoplots indicate TEP components that fall into intervals of topographic inconsistency and are therefore excluded from further topographic analysis.

topography consisted of a bipolar distribution of voltage maximally negative at anterior electrodes and maximally positive at posterior/occipital electrodes. The t-map mirrored this distribution with the greatest positive t-values at left central electrodes (first interval: C1, t=22.31; second interval: FC1, t=31.83) and the greatest negative t-values at left posterior parietal electrode P3 (first interval: t = -19.02; second interval: t=-15.52).

The third interval of dissimilarity (88.5 – 106.5 ms, $p < 0.05$) covered the N100 component of both M1 TEPs and AG TEPs. In this interval, the mean topographic maps of M1 and AG TEPs were visually rather similar, both datasets showing maximum positive voltages at posterior electrodes and maximum negative voltages at anterior electrodes, but with a lateralized distribution towards the right for M1 TEPs, and a more symmetrical distribution across the two hemispheres for AG TEPs. The t-map shows a diffuse pattern with the positive t-values over the right hemisphere, and negative t-values over the left hemisphere.

No significant topographic differences were observed between TEPs recorded in the two sessions. The p value obtained by TANOVA for the factor *session* (Fig. 3.3A) exceeded 0.05 in two short intervals (149.5 – 152 and 196.5 – 197.5 ms) that were not retained when corrected for cluster duration.

3.4.3. Microstate analysis of sub-threshold M1 TEPs and AG TEPs

The microstate analysis yielded six microstate class maps explaining 90.41% of the total variance (Fig. 3.3b). Up until approximately 80 ms post-stimulus, the M1 TEP and AG TEP waveforms were associated with different microstates.

For the M1 TEP waveform, the P30 and P60 were labelled with the same microstate class having a positive maximum over the left central electrode C1 (Fig. 3.3B: class 4). The intermediate component N45 was not evaluated due to its low topographic consistency.

For the AG TEP waveform, the P25 was labelled with a microstate class having a bipolar topography negative over left frontal electrodes and positive over posterior electrodes (Fig. 3.3B: class 1). The later N75 was characterized by a microstate class showing a widespread frontal negativity maximal over the right hemisphere (Fig. 3.3B: class 3). The N40 and P55 were not evaluated due to their low topographic consistency.

The later TEP components, i.e. the N100 and P180 elicited by both M1 and AG stimulation, were composed of the same sequence of microstates with similar latency and duration. Longer intervals of high GFP were associated with one dominant microstate class per component. The N100 was associated with the class 3 microstate that was also ascribed to the N75 component of AG TEPs described above. The P180 was labelled with a microstate class composed of a positive peak centred over the vertex (Fig. 3.3B: class 5). The periods of lower GFP between components were segmented into short intervals of transitory microstates.

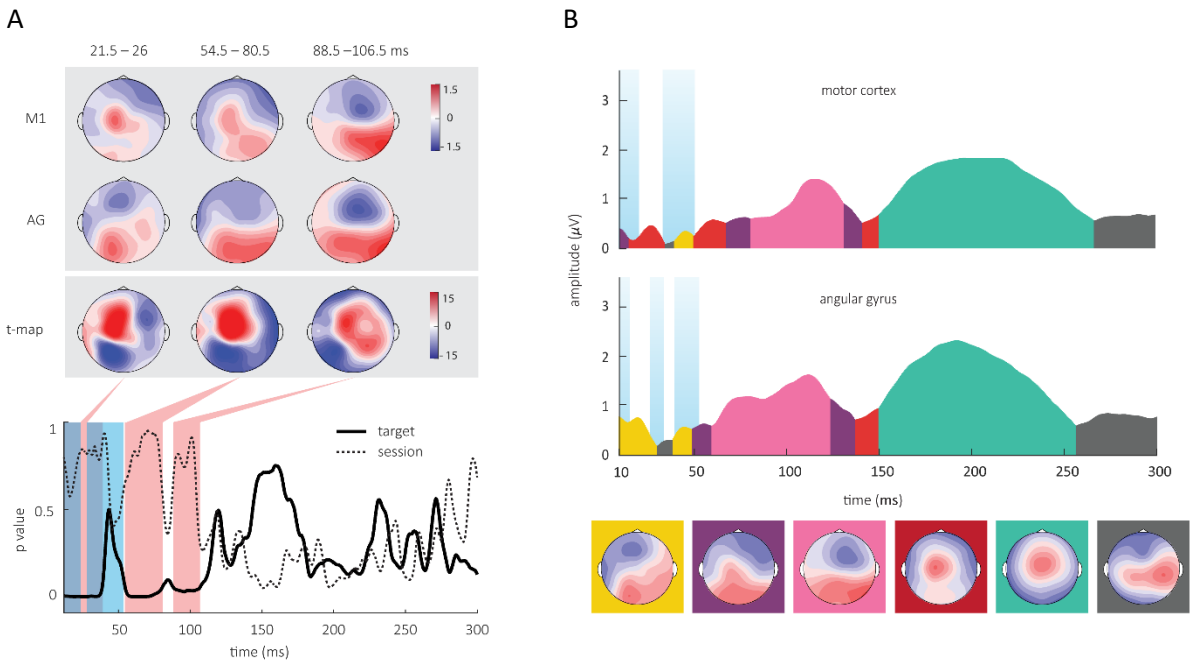

Figure 3.3 Effect of the stimulation site on the TEP topography. (A) Analysis of topographic dissimilarity. The lower section of the figure shows the p values obtained by TANOVA over the analysed time window (10 – 300 ms). The thick full line represents the p value attributed to the topographic dissimilarity between M1 and AG TEPs, the thin dashed line shows the p value of the dissimilarity between TEPs from the two recording sessions. Areas shaded in pink correspond to intervals of $p < 0.05$ (for the comparison of stimulation sites). Blue areas denote the intervals of topographic inconsistency from both datasets combined (purple areas represent the overlap). Upper section shows mean topographies (normalized to GFP) extracted from each interval of interest from the M1 TEP (upper line) and the AG TEP (middle line). The bottom line displays corresponding t-maps (M1 TEP – AG TEP). **(B) Microstate analysis**. The GFP of the M1 TEP (upper) and the AG TEP (lower) is plotted over the analysed time window with the area under the curve coloured in segments corresponding to periods of dominance of individual microstate classes. Template maps of individual classes are color-coded and displayed in the lower section. The intervals of topographic inconsistency are shaded in blue.

3.4.4. Analysis of the topographic dissimilarity between sub-threshold and supra-threshold M1 TEPs

One outlier was identified and excluded from further analysis. The topographic dissimilarity analysis revealed that the topographic distribution of sub-threshold vs supra-threshold M1 TEPs were dissimilar over most of the explored time window, while no differences were detected between TEPs from the two sessions (two short intervals of significance, 77 – 87 and 130.5 – 138 ms, did not survive the correction for cluster duration; Fig. 3.4A). Further exploration of the topographic differences related to stimulation intensity was restricted to the intervals showing topographic consistency across both stimulation conditions. The first identified interval extended 21.5 – 33 ms. The second period of topographic dissimilarity (51 – 221.5 ms) encompassed several TEP peaks having very different topographies. Therefore, it was segmented into three separate intervals of interest (interval 2: 51 – 67, interval 3: 81 – 153.5 and interval 4: 167 – 217 ms) by lowering the significance threshold and only including timepoints with a p value lower than 0.005. A fifth interval of significant dissimilarity was identified towards the end of the explored time window (230.5 – 267.5 ms; Fig. 3.4A).

The first interval of significance (21.5 – 33 ms, $p < 0.01$) covered the P30 component of M1 TEPs. Despite the significant dissimilarity value, the mean maps showed relatively similar topographies with a maximum close to the vertex for both TEPs, shifted towards left central electrodes for the sub-threshold TEP, and more symmetric and widespread for the supra-threshold TEP. This was confirmed by the t-map with negative values over left central electrodes and widespread positive values over the right hemisphere.

The second interval (51 – 67 ms, $p < 0.001$) contained the component P60. For sub-threshold stimulation, the mean topography was very similar to that of the first interval. For supra-threshold stimulation, it took the form of a bipolar topography with maximal positive values over left central electrodes and maximal negative values over right frontal electrodes. The t-map showed a clear pattern of difference with maximum positive t-values over CP5 ($t = 21.79$) and maximum negative t-values over CP6 ($t = -26.95$).

The third interval (81 – 153.5 ms, $p < 0.001$) encompassed the N100. The mean map of the sub-threshold TEP consisted of a frontal negativity shifted towards the right hemisphere and positive voltages over posterior electrodes. For the supra-threshold TEP, it corresponded to a widespread frontal negativity peaking over the left hemisphere. The t-map was characterized by maximally negative t-values over the left central electrode C1 ($t = -27.05$).

The fourth (167 – 217 ms, $p < 0.001$) and fifth (230.5 – 267.5 ms, $p < 0.05$) intervals spanned the P180 component. In the earlier window, the topography of the sub-threshold TEP was centred over the vertex whereas the topography of the supra-threshold TEP was widespread slightly shifted towards the right hemisphere. The t-map shows a clearly defined pattern of difference with maximum negative t-values at CP1 ($t = -23.12$) and the maximum positive t-values at F4 ($t = 17.91$). In the later window of significance, the mean topographies of both sub-threshold and supra-threshold TEPs were relatively symmetric and maximal over the vertex, but the t-map clearly showed that positive scalp voltages spread more posteriorly in the supra-threshold TEP as compared to the sub-threshold TEP.

3.4.5. Microstate analysis of sub-threshold and supra-threshold M1 TEPs

The microstate analysis yielded 8 microstate class maps explaining 91.12 % of the variance (Fig. 3.4B), and confirmed the topographic dissimilarity analysis by attributing different microstates in the compared datasets to the corresponding intervals of high GFP that define TEP components. A single exception was the component P30 that featured the same class map in TEPs evoked by sub- and supra-threshold stimulation. While the supra-threshold TEP waveform was composed of a sequence containing all eight microstate classes (Fig. 3.4B), the topographically consistent sections of the sub-threshold TEP featured only three prominent microstate classes (Fig. 3.4B: classes 2, 4, and 7).

In the next step, temporal features of the microstate classes that figure in both datasets were compared between supra- and sub-threshold TEPs. The microstate class 2, which labelled the P30, showed borderline significant earlier onset ($p = 0.05$) and significantly earlier centre of gravity (COG, $p < 0.05$) in the sub-threshold TEP as compared to the supra-threshold TEP. The microstate class 4, which covered the entire duration of N100 in the sub-threshold TEP and only its beginning in the supra-threshold TEP, showed a significantly longer duration ($p < 0.05$) and later COG ($p < 0.05$) in the sub-threshold TEP. Lastly, the microstate class 7, which encompassed the entire P180 duration in the sub-threshold TEP, appeared only at its end and was shorter lasting ($p < 0.05$) in the supra-threshold TEP. For classes 4 and 7, neither onset nor offset latencies were significantly different between sub- and supra-threshold TEPs.

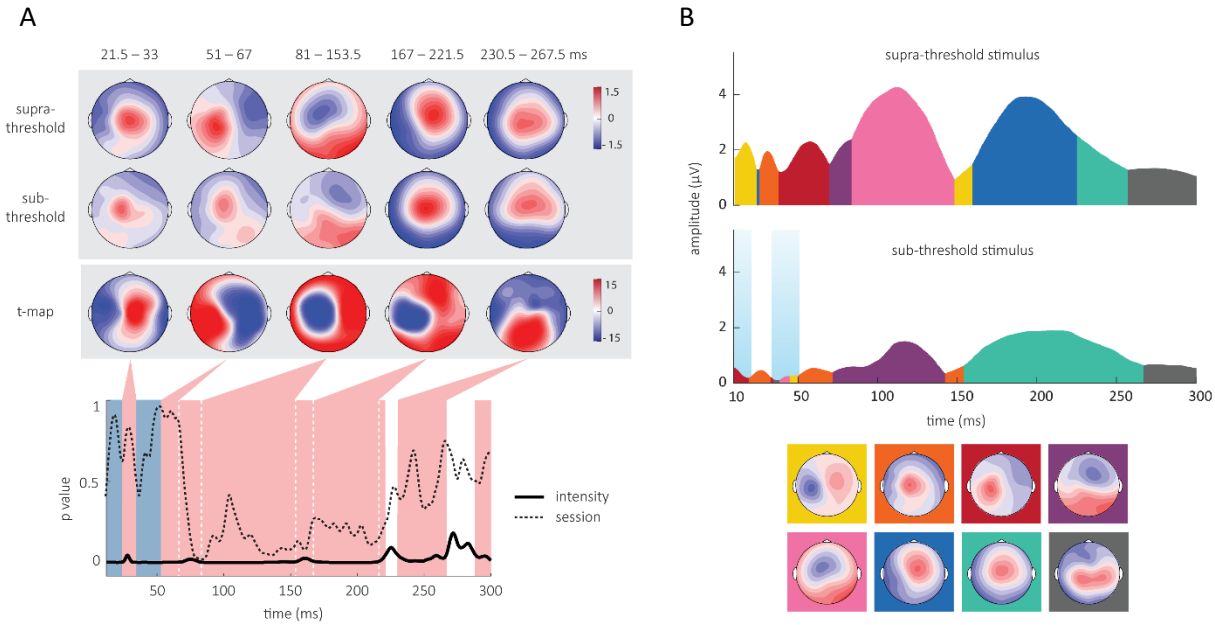

Figure 3.4 Effect of the stimulation intensity on the topography of M1 TEPs. (A) Analysis of topographic dissimilarity. In the lower section of the figure, the p values obtained by TANOVA are plotted over the analysed time window. The thick full line represents the p value attributed to the topographic dissimilarity between sub- and supra-threshold M1 TEPs, the thin dashed line shows the p value of the dissimilarity between TEPs from the two recording sessions. Areas shaded in pink correspond to intervals of $p < 0.05$ (for the comparison of stimulation intensities). White dashed lines border the intervals of $p < 0.005$ that were used for the extraction of mean topographies. Blue areas mark the intervals of topographic inconsistency observed in the sub-threshold TEP (purple areas represent the overlap). The upper section shows mean topographies (normalized to GFP) extracted from each interval of interest from the supra-threshold (upper line) and the sub-threshold (middle line) M1 TEPs. The bottom line displays corresponding t-maps (supra-threshold TEP – sub-threshold TEP). **(B) Microstate analysis**. The values of GFP of the M1 TEP (upper figure) and the AG TEP (lower figure) are plotted over the analysed time window with the area under the curve coloured in segments corresponding to periods of dominance of individual microstate classes. The intervals of topographic inconsistency are shaded in blue. Template maps of individual classes are color-coded and displayed in the lower section; the microstates compared between datasets are highlighted with a black border.

3.5. Discussion

3.5.1. Target specificity of TEPs and the contribution of sensory-evoked responses

In the first part of this study, topographic analysis was used to compare TEPs elicited by stimulation of the primary motor cortex and the angular gyrus, with the aim of distinguishing components corresponding to the genuine cortical activity triggered by TMS stimulation from unspecific components predominantly reflecting cortical activity generated by the peripheral activation of sensory receptors. We assumed that stimulation of each of the two cortical targets would evoke a specific pattern of activation reflecting the direct cortical response to TMS, entangled with additional sensory-evoked activity that might vary in its strength but would have a very similar topographic pattern in both datasets.

Early-latency TEP components. Taken together, our topographic analyses indicate that early-latency TEP components predominantly reflect target-specific activity generated in the proximity of the stimulation site. As such, they likely correspond to the genuine cortical-evoked brain activation that may contain valuable information about the properties of the cortex targeted by TMS and its associated functional networks. While the very early responses, such as the P30 component elicited by M1 stimulation and the P25 component elicited by AG stimulation, appeared to be highly specific for the stimulated region, our data also suggests that other sources of cortical activity, possibly corresponding to early-latency components of a somatosensory-evoked response, might be entangled in the signal of interest from approximately 50 ms. Therefore, any later TEP components should be interpreted with caution. Yet, our conclusion clearly argues against the notion that *all* TEP components are to a great extent generated by unspecific sensory-evoked activity [150].

In our dataset, during the earliest time interval of topographic dissimilarity identified by TANOVA encompassing the P30 component of M1 TEPs and the P25 component of AG TEPs, the t-map closely mirrored the voltage distribution of mean topographic maps, suggesting a clear separation of M1-evoked vs AG-evoked cortical responses. By contrast, in the following interval lasting until approximately 80 ms and covering the P60 component of M1 TEPs and the N75 component of AG TEPs, the t-map highly resembled the one obtained in the previous interval but began to differ from current mean topographic maps. This indicates that the set of cortical sources active during the first interval might remain active during this second interval but the signal becomes mixed with additional background activity that might be shared across both datasets. The subsequent microstate analysis labelled the M1 TEP components P30 and P60 and the AG TEP components P25 and N75 as distinct classes, further confirming the spatiotemporal specificity of these early-latency TEP components.

Our results and their interpretation are in line with previous studies using sham TMS stimulation. Herring et al. compared TEPs evoked by stimulation of the visual cortex to the EEG response elicited

by sham (active TMS delivered at the shoulder). They found that the evoked potentials became highly similar around 80 ms after stimulation onset [157]. Using a similar design while stimulating M1, Biabani et al. reported high temporal and spatial correlation between brain responses to M1 stimulation and sham stimulation starting approximately 60 ms post stimulus [185]. More recently, Freedberg et al. compared TEPs across several cortical targets (the M1, the DLPFC and the posterior parietal cortex) and between active and sham stimulation using cosine similarity, which is another amplitude-free measure that allows to evaluate the global shape of stimulus-evoked brain responses [283]. Similarly to us, they found low spatial similarity across TEPs until approximately 60 ms, after which topographic features started to converge, becoming highly similar around 100 ms [184].

However, it must be pointed out that both datasets showed early periods of topographic inconsistency that were not included in the comparison, thereby limiting our conclusions to a subset of TEP components. We cannot exclude that excessive inter-subject variability in TEP topography indicates an absence of meaningful time-locked activity at these latencies. Or it could correspond to intervals of weak amplitude that is lost in the individual noise, especially when signal averaging relies on a relatively low number of recorded trials [284], as was the case in the present study.

Finally, it is necessary to acknowledge that early TEP components are highly susceptible to the contamination by artifacts related to the TMS-induced contraction of scalp, face or neck muscles [139]. Targeting different cortical areas requires distinct coil placement and likely results in the stimulation of different muscle groups, thereby producing artifacts of specific distribution and magnitude. This might represent a confounding factor when comparing topographies of TEPs evoked by stimulation of different cortical targets, which we tried to avoid by carefully cleaning out the artifacts using ICA.

Late-latency TEP components. At later latencies, both M1 stimulation and AG stimulation triggered high-amplitude responses having very similar topographies, suggesting that they originate from similar cortical sources. This leads us to speculate that late TEP components N100 and P180 could predominantly reflect brain activity triggered by TMS-induced sensory stimulation, in agreement with the body of evidence accumulated in past years [154, 160, 178, 184]. Importantly, the N100-P180 complex could be related at least in part to the so-called vertex potential which can be elicited by any transient sensory stimulus, regardless of sensory modality [161]. We also cannot exclude the possibility that cortical stimulation of a given region may generate cortical responses that are unspecific of the network targeted by TMS.

Such as the vertex potential, the P180 component of TEPs was symmetrically distributed over both hemispheres and maximal at Cz, suggesting its likely association with the sensory response. Such conclusion is further supported by results of a recent study that investigated the contribution of sensory evoked potentials to TEPs by exploring the association between the absolute stimulation intensity and TEP amplitude across all subjects [285]. They assumed that since stimulation intensity is

defined relative to the individual rMT, the strength of direct cortical activation and by consequence the magnitude of corresponding TEPs should be similar across subjects and largely independent of the absolute TMS intensity. By contrast, stimulation of superficial structures may lead to sensory-evoked responses strongly depending on the absolute intensity. A significant regression between both variables was observed at latencies past 170 ms, leading the authors to attribute later TEP components to the response to peripheral stimulation rather than to the direct cortical activation by TMS.

Unlike P180, and unlike the negative component of vertex potentials, the N100 TEP component identified in the present study was lateralized, indicating that additional cortical sources might be active at this time that are common for both TMS stimulation sites but not related to the sensory-evoked vertex potential. Our observations are in line with the findings of two previous studies using different experimental approaches. Rocchi et al. described a lateralized N100 component when comparing sub-threshold M1 TEPs with different sham conditions and various levels of sensory masking [154]. However, they also reported that efficient masking allowed to completely suppress the contribution of sensory-evoked potentials to the recorded TEPs, a statement that is problematic for several reasons. First, because the efficiency of auditory masking varies across subjects and the coverage might be insufficient in individuals requiring higher intensities of TMS because of a high threshold to elicit motor-evoked potentials [155]. Second, there is currently no efficient mean to suppress sensations produced by direct stimulation of peripheral afferents innervating the scalp. In a recent study, Ross et al. attempted to bypass this issue by applying ICA to TEPs evoked by unmasked supra-threshold stimulation of the M1 and the AG in order to isolate and remove signals attributed to auditory-evoked responses [160]. Using this approach, they recovered TMS-evoked cortical activity embedded in the auditory-evoked potential, revealing a new component peaking approximately 120 ms post stimulus and showing similar topography across stimulated cortical regions. Nevertheless, it remains uncertain to which extent ICA is able to separate cortical- and sensory-evoked activity, because the assumption of temporal independence of contributing sources is likely violated due to the time-locked character of all interlaced signals [185].

3.5.2. TEP signature of supra-threshold motor cortex activation

In the second part of the study, topographic analysis was used to compare TEPs elicited by sub-threshold and supra-threshold M1 stimulation with the aim of characterizing the TEP signature of supra-threshold activation of this cortical area.

We envisaged two sources of activity that might additionally contribute to the global topography of supra-threshold M1 TEPs. First, as supra-threshold stimulation of the M1 produces a muscular contraction, these TEPs are probably interlaced with additional somatosensory-evoked activity triggered by the contracting hand muscles. Second, supra-threshold M1 stimulation possibly triggers

additional brain activity in relation to the synchronous excitation of a large numbers of M1 pyramidal neurons. Although it is true that a small fraction of these neurons can fire even when a sub-threshold stimulus is applied [168, 286], we assumed that the corresponding brain response would be weak and therefore would have only a small impact on the topographic pattern of sub-threshold M1 TEPs.

In our dataset, the most remarkable difference between sub-threshold and supra-threshold M1 TEPs was the appearance of an additional early-latency N17 component following supra-threshold stimulation. This early response has been described in other studies where it was referred to as the N15 or N18, and has been attributed to the TMS activation of the ipsilateral M1 [176] or the premotor cortex [130]. Furthermore, the peak-to-peak amplitude of the N15-P30 complex was found to correlate with the amplitude of MEPs [180]. Therefore, this early component could be directly linked to the cortico-spinal output of the M1. It is also possible that similar activity of much smaller magnitude occurs in response to sub-threshold M1 stimulation in a subset of participants, which would explain the period of topographic inconsistency that we identified in sub-threshold M1 TEPs at the latency corresponding to N17.

Almost all subsequent TEP components occurred at similar latencies for sub-threshold and supra-threshold stimulation. The P30 component had a greater amplitude for supra-threshold stimulation as compared to sub-threshold stimulation, but its mean topographical distribution was very similar for the two stimulation conditions, and the microstate analysis labelled it with the same microstate class. Therefore, the P30 could represent a cortical process that is triggered by both sub- and supra-threshold M1 stimulation. Its topography showed a clear positive peak at the proximity of the stimulation site and over the midline, suggesting activity originating from the M1 and/or closely connected cortical areas, possibly including contralateral premotor or sensorimotor cortices, as suggested in previous studies [130, 178, 179]. The P30 could thus reflect activity spread from the M1 and could provide valuable information about the excitability of the M1 and its cortico-cortical connections.

Although peaking at similar latencies, almost all other TEP components elicited by sub-threshold and supra-threshold M1 stimulation exhibited markedly distinct topographies, indicating that they were generated by different combinations of cortical sources. It was previously established that motor re-afference may affect M1 TEPs starting from approximately 40 ms post-stimulus [107, 174]. Coincidentally, the t-map of the P60 component revealed by TANOVA closely resembled the topography of the N20 component of somatosensory-evoked potentials elicited by electrical stimulation of the median nerve [287-289]. The latency of the two components would also match, considering that the earliest change in muscle spindle activity is typically observed around 35 ms after TMS stimulation of the M1 [290]. Finally, a previous study investigating M1 TEPs elicited by stimulation at the threshold intensity for eliciting a motor response reported a significantly larger P60 in TEPs accompanied by a MEP than in TEPs with no peripheral response. Moreover, the source of this

component was localized in both motor and sensory cortex in the stimulated hemisphere [183]. Based on these observations, we hypothesize that the difference in P60 topography could be largely explained by the presence of a somatosensory-evoked potential triggered by the hand muscle contraction following supra-threshold stimulation.

As discussed earlier, the later TEP components N100 and P180 elicited by sub-threshold M1 stimulation can be mostly attributed to sensory-evoked vertex potential caused by the TMS discharge. If so, one would expect supra-threshold M1 stimuli to evoke a stronger response having the same topographic pattern. Yet, our data show clear topographic dissimilarity in the time intervals encompassing both components, with the t-map revealing additional negativity over the stimulated hemisphere in supra-threshold M1 TEPs. A similar observation was previously made by Gordon et al. [158] who attributed this topographic difference to the somatosensory response to the evoked muscular contraction. Alternatively, we speculate that this late-latency activity specific to supra-threshold M1 stimulation might represent an inhibition of the ipsilateral sensorimotor cortex occurring in response to a strong, unexpected excitation of the M1. The N100 component of M1 TEPs has been previously linked to cortical motor inhibition as its amplitude was found increased when subject prepared to resist the TMS evoked contraction [189], decreased during movement [190], decreased when contractions were actively facilitated [147] and correlated with the so-called cortical silent period [191]. It was also suggested that this component is at least partially mediated by metabotropic $GABA_B$ receptors, whose pharmacological activation can enhance the N100 amplitude [186].

3.5.3. Usefulness and limitations of topographic analysis in TEP evaluation

In the present study, we show that the differential engagement of cortical sources contributing to TEPs can be successfully detected and characterized using topographic dissimilarity analysis, and that the spatiotemporal features of individual TEP components can be extracted and compared across datasets using microstate analysis. Together, our results allowed us to identify components of interest for future evaluation of the effect of experimental manipulation, thus demonstrating the practical utility of topographic analysis of TEPs.

The multiple advantages of topographic analysis have been already mentioned: it allows to consider all channels in a single measure, thus minimizing the loss of information; it identifies time intervals of interest in a purely data-driven manner, without the necessity of a prior choice; it helps avoid the bias introduced by the arbitrary choice of the reference electrode. However, similarly to other methods employing point-by-point comparisons, topographic analysis assumes spatiotemporal consistency of TEP components across subjects – an assumption that has been disproved in the past [114]. While the topographic inter-subject variability is partially mitigated by the effect of volume conduction in EEG data, the variability in TEP latency might be problematic, particularly when

considering the very early and very transient TEP components. Furthermore, since topographic analysis relies on normalized scalp voltage maps, it does not provide information on the strength of the observed response. It is therefore suitable to combine it with additional analyses to evaluate the amplitude of the elicited response.

At this point, we propose that the spatiotemporal features obtained by microstate analysis might also serve as a valuable prior for the extraction of the peak amplitude of individual TEP components at the subject level (see chapter 4).

3.6. Conclusion

We have used topographic analysis to characterize the spatiotemporal features of TEPs and to identify TEP components most suitable to provide information about the properties of stimulated cortical areas and associated brain networks. By comparing TEPs from two different cortical areas, we confirmed that early TEP components until approximately 80 ms post stimulus likely represent, at least to a considerable extent, genuine TMS-evoked cortical activity. By contrast, later TEP components N100 and P180 showed site unspecific features, suggesting that they mostly reflect responses to the peripheral activation of sensory receptors, and as such should be interpreted with caution. Next, we evaluated the specific TEP signature of supra-threshold M1 activation as compared to sub-threshold M1 activation. We found that supra-threshold stimulation elicits an early N17 component which presumably corresponds to the activation of M1 neurons of the cortico-spinal tract. Topographical differences between sub- and supra-threshold M1 TEPs were also observed at later latencies, some of which may reflect somatosensory processing of inputs triggered by the muscular contraction. We conclude that topographic analysis might represent an advantageous method for TEP evaluation and interpretation.

4. Evaluation of $GABA_AR$-mediated inhibition in the human brain using TMS-evoked potentials

4.1. Abstract

$GABA_AR$-mediated inhibition participates in the control of cortical excitability, and its impairment likely contributes to the pathologic excitability changes that have been associated with multiple neurological disorders. Therefore, there is a need for its direct evaluation in the human brain, and the combination of TMS and EEG might represent the optimal tool. TEPs recorded by EEG capture the spread of activity across the stimulated brain network. Since this process at least partially depends on $GABA_AR$-mediated inhibition, TEPs may constitute relevant biomarkers of local $GABA_A$ergic function.

Here, we aimed to assess the effect of $GABA_AR$ activation using TEPs, and to identify TEP components that are sensitive to the state of $GABA_A$ergic inhibition. In 20 healthy subjects, we recorded TEPs evoked by sub- and supra-threshold stimulation of the M1, MEPs, and resting-state EEG (RS-EEG). $GABA_ARs$ were activated (1) pharmacologically by oral administration of alprazolam compared to placebo within each subject, and (2) physiologically using a sub-threshold conditioning stimulus to characterize the effect of SICI.

In supra-threshold TEPs, alprazolam suppressed the amplitude of components N17, N100 and P180, and increased component N45. The pharmacological modulation of N17 correlated with the change observed in MEPs and with the alprazolam-induced increase of lower β-band RS-EEG. Only a reduction of N100 and P180 was found in sub-threshold TEPs. TEP SICI manifested as a reduction of N17, P60 and N100, and its effect on N17 correlated with the alprazolam-induced N17 suppression and β increase. Our results indicate that N17 of supra-threshold TEPs could serve as a non-invasive biomarker of local cortical excitability reflecting the state of $GABA_AR$-mediated inhibition in the sensorimotor network. Furthermore, the alprazolam-induced increase of β-band oscillations possibly corresponds to the increased inhibitory neurotransmission within this network.

4.2. Introduction

Fine tuning of the activity of excitatory and inhibitory systems is crucial for maintaining physiological brain functions [291, 292], its dysregulation potentially leading to pathological changes in cortical excitability. In various neurological disorders, including epilepsy [39], schizophrenia [40], amyotrophic lateral sclerosis (ALS) [42] and Alzheimer's disease (AD) [43], the balance is tipped towards increased excitation that can be associated with excitotoxicity. While the original cause of such disbalance is difficult to pinpoint, the suspicion often falls on impaired inhibition. Inhibitory neurons represent only a small portion of all cortical neurons (10-15% reported in rodents; [6]). However, they come in a great variety of morphologic and connectivity types [293, 294], forming a complex and flexible system holding control over principal excitatory neurons and regulating the

dynamics of entire brain networks [11, 295, 296]. For this reason, minor functional impairment of inhibitory neurons could produce extensive changes in brain function.

The most common inhibitory neurotransmitter of the brain is GABA. The release of GABA by GABAergic inhibitory interneurons exerts fast inhibitory effects via postsynaptic activation of $GABA_AR$s that react to the neurotransmitter binding by increasing the membrane permeability for chloride ions [297]. Resulting hyperpolarization of the postsynaptic membrane gives rise to an inhibitory potential at the target neuron that contributes to the synchronisation of network oscillatory activity [11]. The strength of $GABA_AR$-mediated inhibition and therefore the performance of the inhibitory system can be influenced at multiple levels both pre- and post-synaptically, with any change triggering a cascade of compensatory or adaptive processes. Accordingly, neurological disorders that are characterized by an excitation-inhibition imbalance towards reduced inhibition have been previously linked both to the malfunction of inhibitory interneurons [38, 237, 238] and to alternations in $GABA_AR$ expression and function [239-242].

Considering the possible involvement of GABAergic inhibitory dysfunction in a wide array of neurological diseases, it is important to establish reliable methods to assess the functional state of $GABA_AR$-mediated neurotransmission in humans. This might be particularly useful for neurodegenerative disorders such as AD or ALS, where impairment of inhibitory neurotransmission is likely to occur prior to clinical symptoms and where early diagnosis and early treatment could positively influence the prognosis. For this purpose, the combination of TMS and EEG represents a promising tool because it allows to directly probe the functional properties of cortical networks. TMS can non-invasively and painlessly stimulate a precisely defined cortical area [46, 298], and concomitant EEG can capture in real time the spread of the TMS-evoked activity across the brain [107, 108]. Importantly, both methods are long established in experimental and clinical research, with few contra-indications and relatively low cost, which favours them for routine application in large patient groups.

TMS combined with EEG has already been successfully used to evaluate the state of inhibition in the human brain by characterizing the changes in TEPs induced by the experimental activation of $GABA_AR$s. This can be achieved by different means. Receptor function can be modulated pharmacologically with benzodiazepines that enhance $GABA_AR$-mediated inhibition globally, as they act on selected subtypes of the receptor across the whole nervous system. Using this approach, Premoli et al. in their pioneer study identified specific TEP components sensitive to $GABA_AR$ activation [186]. Alternatively, it is possible to trigger $GABA_AR$-mediated inhibition locally by pre-activating inhibitory interneurons at the site of stimulation with a sub-threshold conditioning TMS pulse. This was originally described in MEPs using the so-called “paired-pulse paradigm” in which two TMS pulses are delivered in rapid succession over the M1, a sub-threshold conditioning TMS pulse followed by a supra-threshold TMS pulse. As compared to the amplitude of the MEP elicited by a single supra-

threshold TMS pulse, the amplitude of the MEP elicited by the paired-pulse TMS is markedly reduced, and this effect has been attributed to the triggering of $GABA_AR$-mediated SICI [248, 299]. More recently, several groups also described SICI in M1 TEPs, yet their findings were highly variable as well as the methodology they used [44, 194, 259-261, 300].

In the present study, we aimed to identify TEP-based biomarkers of $GABA_AR$-mediated inhibition in the human brain and to verify its reliability using different approaches. First, we activated the inhibitory system globally using alprazolam, a classic benzodiazepine that acts on $GABA_ARs$ containing α1, α2, α3 and α5 subunits [301]. We described its effect on TEPs evoked by stimulation of the left M1 using both sub- and supra-threshold stimulation intensities by comparing the effects of alprazolam to those of an active placebo. In addition, we recorded resting state EEG to extract previously established biomarkers of benzodiazepine-induced sedation and related them to changes observed in TEPs. Second, we used paired-pulse stimulation to activate local inhibitory interneurons and characterized the effect of SICI in M1 TEPs. We assumed that the increase of $GABA_AR$-mediated neurotransmission produced by the two methods would result in similar changes for M1 TEP components that are specifically dependent on the state of $GABA_AR$ neurotransmission locally within the stimulated cortex, whereas alprazolam could produce additional changes in other M1 TEP components due to its inhibitory effect in the entire brain.

4.3. Materials and Methods

4.3.1. Ethical approval

All experiments were conducted according to the latest revision of the Declaration of Helsinki. The protocol and all procedures were approved by the local Ethical Committee. All participants were thoroughly informed of the protocol and applied procedures, gave a written informed consent before taking part in the study, and were financially compensated for their participation.

4.3.2. Data and code availability

The data presented in this study are not freely available, because the informed consent signed by the participants did not include the agreement to public data sharing. However, it is possible to request the raw or pre-processed datasets from the corresponding author, under the condition of an established inter-institutional agreement of the data transfer. MATLAB and R scripts used to process and evaluate the data are accessible from the GitHub page of the corresponding author (https://github.com/DominikaSulcova/GABA-AD), and the letswave6 toolbox that provided called functions can be downloaded here: https://letswave.org.

4.3.3. Participants

20 healthy volunteers (10 males, mean age 24) took part in the study. All participants filled a detailed questionnaire and undertook a brief neurological examination to exclude candidates with any contraindication for experimental procedures, such as epilepsy (or familiar history thereof), migraine, presence of a metal object in the body (e.g. insulin pump, pacemaker, metal prothesis), confirmed neurological pathology, or use of medication known to alter cortical excitability [274].

4.3.4. Experimental design

Two experimental sessions, each lasting approximately 5.5 h and separated by at least one week, were conducted at the premises of the UCLouvain Institute of Neuroscience (IoNS). The experiments always started in the morning at times as similar as possible in both sessions for each subject. The subjects were asked to sleep sufficiently, to refrain from consumption of alcohol the preceding evening and to avoid caffeinated beverages in the morning. Each session consisted of the baseline recording of resting state EEG (RS-EEG) and TMS stimulation of the left (dominant) M1 combined with EEG for the recording of TEPs and EMG for the recording of MEPs. An additional block of TMS stimulation of the left angular gyrus was performed but the results are not discussed in this publication (see Supplementary materials). Subjects then received a single dose of either alprazolam (Xanax, 1mg) or active placebo (Zyrtec, 10 mg), and the recording was repeated starting 1.5 h after the medication. This timing corresponds to the average peak levels of alprazolam in the blood following oral administration [302, 303]. The order of the two sessions was balanced across subjects. The medication was provided to the participant by a third party so that both subjects and experimenters performing the experimental sessions and analysing the recorded data were blinded to the order of the medication.

4.3.5. EEG recording

The EEG was recorded using the NeurOne EEG system (Bittium NeurOne Tesla; Bittium Corporation, Oulu, Finland) and a 32 channel EEG cap mounted with TMS-compatible Ag/AgCl electrodes (EasyCap GmbH, Herrsching, Germany). The signal was recorded at a 20 kHz sampling rate with a 5000 Hz low-pass filter and a DC filter. The averaged signal from both mastoids was used as reference, an extra ground electrode was placed on the forehead. Electrode impedances were monitored during the session and kept below 5kΩ. Two blocks of RS-EEG with eyes open and closed, each lasting at least 3 min, were recorded at baseline and after the medication, before TMS stimulation. During the recording with eyes open, subjects kept their gaze on a stable point placed in such way that its fixation did not require any muscular effort.

A thin plastic film was placed over the electrodes and subjects wore an extra rubber cap on top of the plastic film to minimize artifacts caused by direct contact of electrodes with the TMS coil. These additional layers also helped to reduce bone conduction of the noise generated by TMS stimulation. In addition, subjects listened to a masking noise created from an original recording of the TMS click to further reduce possible auditory artifacts [151].

4.3.6. EMG recording

Disposable surface gel electrodes were placed over the first dorsal interosseous muscle (FDI) of the right hand using the belly-tendon montage, with the ground electrode placed at the right wrist over the styloid process of radius. MEPs were recorded at a 1,024 Hz sampling rate using the MOBI amplifier (TMSi MOBI; Twente Medical Systems International B.V., Oldenzaal, The Nederlands).

4.3.7. TMS stimulation and neuronavigation

A 3D T1-weighted structural MRI image of each participant's whole brain was acquired beforehand at the Department of radiology of the Cliniques universitaires Saint-Luc (1×1×1 mm; 3 T Achieva; Philips Healthcare, Amsterdam, The Netherlands). The Visor2 neuronavigation system (Visor 2.3.3; Advanced Neuro Technologies, Enschede, The Netherlands) was used to verify the accurate placement of the TMS coil and to monitor its position throughout the experiment. A 3D model of the scalp and brain surface was reconstructed using the individual MRI data and co-registered with the real space using landmark-based markers (nasion and tragi) and head-shape matching [275].The position of the head as well as the TMS coil was continually registered with the Polaris infrared optical tracking system (Polaris Spectra; Northern Digital Inc. Europe, Radolfzell, Germany).

Biphasic TMS pulses were delivered manually using a MagPro X100 magnetic stimulator (MagPro X100 with MagOption; MagVenture, Farum, Denmark). A figure-of-eight TMS coil with an outer diameter of 75 mm (C-B60; MagVenture, Farum, Denmark) was tangentially placed on the scalp and centred over the target in the left M1 (Fig. 4.1A). Target location was determined functionally as the site eliciting the largest TMS-evoked MEP in the relaxed right FDI when stimulating with slightly sub-threshold intensity and inducing electrical currents in the brain with an anterior–posterior posterior–anterior direction. The optimal coil orientation was adjusted individually, with the handle always pointing laterally and posteriorly at an approximate 45° angle from the midline. Target parameters were saved in the neuronavigation system to keep stimulation sites identical in the second experimental session.

The rMT was set to the minimal stimulation intensity eliciting a motor response with the amplitude of least 50 µV in at least 5 trials out of 10 [276]. Its value was verified and adjusted, if necessary, before the data acquisition after medication, in order to record reliable MEPs. The mean rMT at baseline (in % of the maximum stimulator output ± SEM) was 49.3 ±1.4 in the placebo session

and 49.8 ±1.4 in the alprazolam session. This difference was not significant (repeated measures ANOVA: $F(1, 19) = 1.05$, $p = 0.32$).

Three types of TMS stimuli were applied over the M1: supra-threshold single pulses at 120% rMT (testing stimulus, TS); sub-threshold single pulses at 80% rMT (conditioning stimulus, CS); and paired pulse TMS consisting of a CS followed by a TS with an inter-pulse interval of 2.5 ms (CS-TS). 60 stimuli per stimulation type were delivered to the M1 in a semi-random order (maximum 3 repetitions of the same condition) and a randomly varying inter-trial interval (4-6 s). The sequence was split into three blocks of 60 stimuli with simultaneous EEG and EMG recordings, separated by a short break.

4.3.8. Data processing

TEPs, MEPs and RS-EEG were analysed offline in Matlab (MathWorks, Inc., Natick, Massachusetts, United States) using Letswave 6 (an open-source EEG signal processing toolbox, https://www.letswave.org/) and custom scripts.

TEPs. Data pre-processing generally followed a previously established pipeline [139]. The EEG signals were first re-referenced to the common average of all scalp channels. The DC shift was removed and a linear detrend was applied. The continuous EEG recordings were then epoched around the onset of the TMS pulses from –1000 ms to +2000 ms. The large-amplitude artifact caused by the TMS pulse was removed using cubic interpolation (from -5 to +10 ms) and the signals were down-sampled to 2 kHz. The first round of ICA was performed to remove the remaining tail of the TMS-evoked muscle artifact, because the sharp edge of the tail might otherwise interfere with applied frequency filters. The data was then bandpass filtered between 0.1 and 80 Hz (Butterworth, 4^{th} order) and notch filtered at 50 Hz (FFT linear filter, notch width 2 Hz, slope cut-off width 2 Hz). In the next step, data were visually inspected to remove epochs containing excessive noise or isolated outbursts thereof. Any trials associated with a missed TMS stimulation (in case of an unexpected head movement causing coil misplacement, etc) were discarded. The average number of remaining epochs (± SD) was 48.0 ± 6.9 in the placebo session and 47.8 ± 6.9 in the alprazolam session. The second round of ICA was used to remove any remaining artifacts such as eye blinks, horizontal eye movements, persistent muscle activity and electrode noise. Artefactual components were first identified automatically with MARA, a linear classifier originally trained on adult EEG data [278]. Pre-selected components were then manually assessed based on their topography, time course and power spectrum density to remove only components with clear non-neural origin (a detailed characterization of different types of removed artifacts is available in Supplementary materials). All epochs were baseline corrected to the interval from -200 to -5 ms and the trials were averaged for each subject/condition.

Time window between 10 and 300 ms post stimulus was considered for the analysis. Peak latencies of TEP components were identified in the temporal profile of the GFP calculated from the

baseline recordings. Identified TEP components were then named according to their polarity as seen in the signal at electrode Cz (positive = P, negative = N) and their average latency in ms. Based on the results of the topographical analysis performed on baseline recordings [304], we identified three electrodes of interest (EOIs) for each TEP component and each type of stimulus (expectedly, the EOIs were the same for supra-threshold TMS pulses delivered over the M1 in TS and CS-TS conditions). The peak amplitude of each TEP component was extracted at the subject level from the averaged signals measured at the EOIs using a semi-automatic approach (the process of EOI identification and peak amplitude extraction is described in more detail in Supplementary materials, section 4.). This approach allowed to account for individual differences in the latency of TEP components while keeping other extraction parameters constant across subjects.

MEPs. Raw EMG signals were corrected for DC shift, linear detrended and high-pass filtered with 4 Hz cut-off (Butterworth, 4^{th} order). The signals were then segmented around the TMS pulse into epochs ranging from -100 to +400 ms. Epochs with excessive baseline activity were identified and discarded using an automated selection process based on the baseline mean root square (MRS) value (see Supplementary materials), with 56.5 ± 3.4 (SD) epochs retained on average across datasets. The signals were then baseline corrected by subtracting the mean amplitude of the interval between -200 and 0 ms. The peak-to-peak MEP amplitude was extracted for further analysis.

RS-EEG. Raw RS-EEG recordings were down-sampled to 2 kHz, re-referenced to a common average of all scalp channels and bandpass filtered between 0.1 and 45 Hz (Butterworth, 4^{th} order). Following a visual inspection, 2 minutes of clean signal were cut out from each of the two original 3-minute recordings (eyes open and closed). ICA (Infomax algorithm), applied on the concatenated EEG signals, was then used to remove artifacts with clear non-neural origin (e.g. tonic muscle contraction, eyeblinks, electrode noise). The denoised datasets were then segmented in 50% overlapping epochs lasting 12 s for the analysis of δ band oscillations and 4 s for the analysis of higher frequency bands. A Hanning window was applied to each epoch to minimize spectral leakage. The epochs were transformed using the Fast Fourier Transform and averaged across epochs to express mean amplitude for each frequency bin between 0.1 and 45 Hz. EEG channels were clustered into five regions of interest (ROIs; frontal: Fp1, Fp2, Fz, F3, F4, F7, F8; central: FC1, FC2, Cz, C1, C2, CP1, CP2; left temporal: FC5, T7, C3, CP5; right temporal: FC6, T8, C4, CP6; occipital: P3, P4, Pz, P7, P8, O1, O2).

Baseline data of each subject were used to identify the Individual Alpha peak Frequency (IAF) and the Transition Frequency (TF, frequency marking the transition between θ band oscillations and the α peak) as described in [100]. Based on these values, the frequency spectra were split into the following bands: δ (0.1Hz – [TF – 4Hz]), θ ([TF – 4Hz] – TF), lower α1 (TF - [TF + (IAF -TF)/2]), lower α2 ([TF + (IAF -TF)/2] - IAF), higher α3 (IAF - [IAF + (IAF -TF)/2]), lower β1 ([IAF + (IAF -TF)/2] – 20Hz), higher β2 (20 – 30Hz), and γ (30 – 45Hz).

Three RS-EEG measures were selected for further statistical analyses: (1) The average amplitude of lower β frequency band was extracted from the central ROI in the 'eyes-open' dataset and used to characterize the effect of alprazolam, because an increase in lower β oscillations following the administration of benzodiazepines was previously reported in multiple studies and proposed as a RS-EEG biomarker of the benzodiazepine effect [305-308]. (2) The Alpha Attenuation Coefficient (AAC) was calculated as the ratio of the broadband α amplitude in 'eyes closed'/'eyes open' over the occipital ROI. The AAC was previously established as a measure of drowsiness based on the observation that with increasing subjective drowsiness the α amplitude increases with eyes open and decreases with eyes closed [309, 310]. Similar changes in α oscillations were also observed after medication with benzodiazepines [311-313]. Therefore, we expected a decrease in AAC following the administration of alprazolam. (3) The Spectral Exponent (SE) was calculated as the slope of the 1/f-like non-oscillatory spectral component under the log-log transform across the lower part of the spectrum (δ – lower β) using the data averaged across all ROIs (for a detailed description see [314]). SE was previously linked to the excitation-inhibition balance in neural circuits [315] and its increased negativity was observed during states of reduced consciousness [314]. Based on these reports, we expected SE to gain more negative values following the administration of alprazolam.

4.3.9. Statistical analysis

Statistical analyses were performed using Matlab and R [316]. A Linear Mixed Model (LMM) analysis was implemented and interpreted using R packages *lme4* [317] and *lmerTest* [318].

The effect of alprazolam was evaluated in relation to single-pulse TEPs, MEPs, RS-EEG, as well as the extent of SICI in TEPs and MEPs. The post-medication change was calculated as percentage of the post-medication value relative to the baseline value for RS-EEG and MEPs, and as the difference between baseline and post-medication measures for TEP amplitudes. Each obtained outcome variable was then separately evaluated using a LMM model that allowed for a random intercept (Equation 4.1). The predictor of interest was the factor *medication* with 2 levels (placebo, alprazolam). When evaluating alprazolam-induced change in TEPs, the change in rMT was entered as a time-varying covariate after being centred to mean 0. The final p value was obtained using the Kenward-Roger approximation.

SICI in the M1 was quantified for each subject in both sessions at baseline, i.e. before medication. To assess the effect of the paired pulse stimulation on the amplitude of MEPs and individual TEP components, a LMM model with random intercept was used (Equation 4.2). The measured raw amplitude was entered as the dependent variable, the main predictor was the factor *stimulus* with 2 levels (TS, CS-TS) and the session ID was entered as a covariate. Final p value was obtained using the Kenward-Roger approximation.

For the purposes of visualization and correlational analysis, SICI of MEPs was expressed as the percent change of peak-to-peak MEP amplitude elicited by CS-TS compared to the MEP evoked by the TS stimulus alone, while SICI of each TEP component was computed as a simple difference between the amplitude of CS-TS TEPs and TS TEPs. To evaluate possible correlations between the selected variables, Pearson correlation coefficients were computed and tested against 0, with the significance level adjusted using Bonferroni correction in case of multiple comparisons. In certain cases, if the preliminary visualization suggested a non-linear relationship between variables, the data were ranked, and a Spearman correlation coefficient was used instead.

$$(1)\ \Delta\widehat{DV}_{ij} \sim \hat{\gamma}_0 + \hat{\gamma}_1 * medication_{ij} + \hat{\gamma}_2 * \Delta rMT + \hat{u}_{0j} + e_{ij}$$

$$(2)\ \widehat{DV}_{ij} \sim \hat{\gamma}_0 + \hat{\gamma}_1 * stimulus_{ij} + \hat{\gamma}_2 * session + \hat{u}_{0j} + e_{ij}$$

Equations 4.1 – effect of alprazolam, 4.2 – effect of SICI. $\hat{\gamma}_0$ represents the common parameter for the intercept, $\hat{\gamma}_1$ the common parameter for the main predictor, $\hat{u}_{0j}$ stands for the individual variability in the intercept (= random effect), and e_{ij} for the residual error.

4.4. Results

All mean values are reported ± SEM.

4.4.1. TEP features depend on TMS stimulation intensity

Supra-threshold TMS stimulation of the M1 evoked consistent TEPs composed of 6 components that showed latencies similar to those previously reported in the literature: N17, P30, N45, P60, N100 and P180 (Fig. 4.1C). The components were clearly identified as local maxima in the GFP of the group average TEP waveform, except for N45 that might have been overlayed by the peak corresponding to P60. By contrast, only five TEP components were identified in TEPs evoked by sub-threshold TMS stimulation of the M1 at latencies corresponding to P30, N45, P60, N100 and P180 (the earlier N17 component was impossible to distinguish in most individual datasets; Fig. 4.1D). TEPs elicited by sub-threshold stimulation had a lower amplitude and the topography of all components (with the exception of P30) differed substantially from those evoked by supra-threshold stimulation. Baseline M1 TEPs were analysed in detail and compared with TEPs elicited by stimulation of the angular gyrus in a separate publication [304].

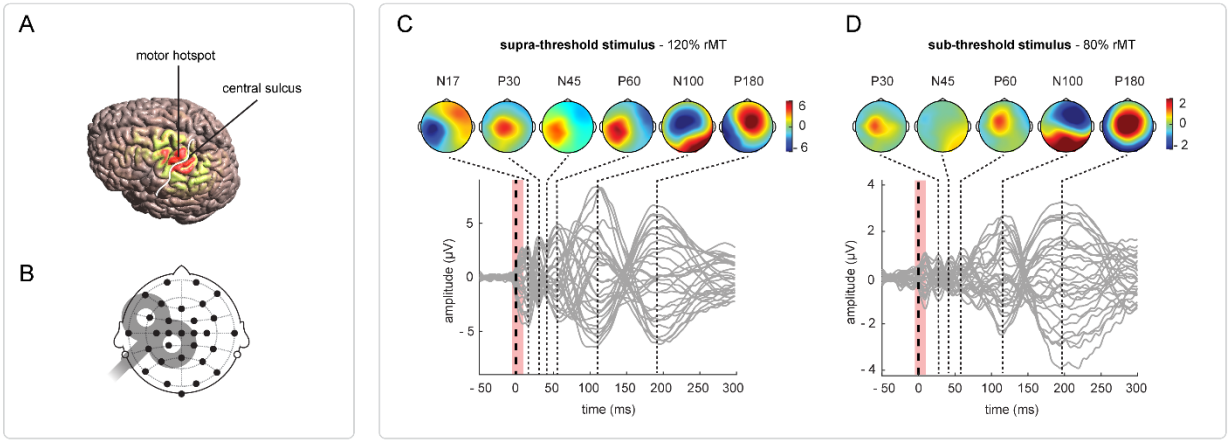

Figure 4.1 TMS-EEG over the primary motor cortex. (A-B) Targeting M1 (A) Magnetic field spreading across the brain surface when targeting the hand area of the left primary motor cortex with TMS (modelled on the default brain with the simulation software simNIBS [97]). (B) Approximate placement of the TMS coil over the head. Black circles represent EEG electrodes in the used setup. **(C-D) Baseline M1 TEPs evoked by supra-threshold** (C) and sub-threshold (D) M1 stimulation. Grey traces represent the signal of all electrodes recorded at the baseline in the placebo sessions (there were no substantial differences between baseline TEPs of both sessions), TMS stimulus is marked by a thick dashed line, the interval interpolated following the removal of TMS artifact is shaded in pink. Dotted lines mark peak latencies of TEP components, associated topographies are shown above.

4.4.2. Alprazolam modulates peak amplitude of specific TEP components

The peak amplitude of individual TEP components served as the main outcome variable when evaluating the effect of medication on TEPs. Mean observed changes and the outcome of the statistical analysis are summarized in Table 4.1. When considering the TEPs evoked by supra-threshold M1 stimulation (Fig. 4.2A,B), an opposite effect of medication was observed for N17 amplitude: while alprazolam led to a decrease of this component, placebo caused an increase. Subsequent TEP components were only minimally influenced by placebo, whereas alprazolam caused an increase of N45 and a reduction of N100 and P180. In addition, a borderline significant reduction caused by alprazolam was found in P60 ($p = 0.05$).

In TEPs elicited by sub-threshold M1 (Fig. 4.2C,D), late TEP components N100 and P180 were clearly suppressed by alprazolam as compared to placebo, while earlier components showed no significant change in amplitude.

4.4.3. Drug-induced change in MEP amplitude is correlated with change in amplitude of TEP N17

When evaluating the effect of medication on the amplitude of single-pulse MEPs, we found that while alprazolam caused an average decrease by 18.8 ± 10.6 %, placebo led to an average increase by 3.8 ± 10.3 % (Fig. 4.2E). However, the alprazolam-induced change was not significantly different from placebo ($F_{1, 18.54} = 3.8$, $p = 0.07$).

We further explored the relationship between the drug-induced changes in MEP and TEP amplitudes. Since the preliminary data visualization suggested possible linear relationships between

MEP and TEP changes, we calculated Pearson's correlation coefficients for MEPs and the 6 components of supra-threshold M1 TEPs (Bonferroni corrected). From all tested components, only N17 showed a significant correlation between both variables when data from both sessions were pooled together ($r(38) = 0.46$, $t = 3.16$, $p < 0.01$, adjusted $R^2 = 0.19$; see Fig. 4.4A). This correlation remained significant and showed very similar slopes when the sessions were considered separately. This indicates that the modulation of N17 amplitude is directly associated with the modulation of cortical motor output.

stimulus	peak	mean change in amplitude		F statistic	df	p value	
		placebo	alprazolam				
M1 120 %rMT	**N17**	1.33 ± 0.58	- 1.44 ± 0.60	10.62	1, 18.54	< 0.01	**
	P30	- 0.22 ± 0.30	0.57 ± 0.59	1.77	1, 18.50	*n.s.*	
	N45	- 0.10 ± 0.49	1.08 ± 0.35	4.91	1, 18.39	< 0.05	*
	P60	- 0.25 ± 0.69	- 1.64 ± 0.68	4.43	1, 17.55	0.05	
	N100	- 0.52 ± 0.66	- 3.48 ± 0.88	7.95	1, 18.50	< 0.05	*
	P180	0.45 ± 0.57	- 1.52 ± 0.55	6.19	1, 18.53	< 0.05	*
M1 80 %rMT	**P30**	- 0.05 ± 0.22	- 0.26 ± 0.26	0.40	1, 18.52	*n.s.*	
	N45	0.04 ± 0.27	0.25 ± 0.20	0.00	1, 17.54	*n.s.*	
	P60	- 0.23 ± 0.20	- 0.52 ± 0.25	0.96	1, 18.46	*n.s.*	
	N100	- 0.04 ± 0.28	- 1.44 ± 0.42	11.19	1, 18.35	< 0.01	**
	P180	- 0.61 ± 0.40	- 2.48 ± 0.43	10.00	1, 18.54	< 0.01	**

Table 4.1 Mean change in TEP amplitude and corresponding statistics. Amplitude change was computed as the difference between measurement post-medication and the baseline, in the table represented in µV ± SEM. Positive numbers mark an increase of the amplitude and vice versa, in case of negative components the voltage measures were multiplied by -1.

4.4.4. The effect of alprazolam manifests in RS-EEG

Alprazolam caused multiple changes in the oscillatory content of the RS-EEG. We observed an overall increase in δ band amplitude, an increase in the amplitude within the high α and both β bands in the eyes open condition, and a substantial suppression of oscillations across all α sub-bands in the eyes closed conditions (Fig. 4.2F,G). For all three RS-EEG measures that were selected for the statistical evaluation, we observed a change in the same direction following the administration of both drugs, which was significantly greater after alprazolam compared to placebo. Mean observed changes as well as the outcome of the statistical analysis are summarized in Table 4.2. As expected, the β increase over the central region proved to be a particularly consistent marker of the effect of alprazolam. The AAC decrease was mostly related to an extensive suppression of the α peak in the eyes closed condition. Lastly, the SE became more negative after alprazolam, which corresponds to a steeper PSD slope.

RS-EEG measure	mean change		F statistic	df	p value	
	placebo	alprazolam				
lower β amplitude	10.04 ± 2.76	58.50 ± 7.64	35.56	1, 19	< 0.001	***
AAC	- 14.37 ± 5.99	- 34.43 ± 5.1	8.99	1, 19	< 0.01	**
SE	- 0.05 ± 0.03	- 0.22 ± 0.06	6.93	1, 19	< 0.05	*

Table 4.2 Mean change in RS-EEG measures and corresponding statistics. The change in lower β amplitude and in the AAC is represented in % of baseline ± SEM. The SE change was computed as the difference between the measurement post-medication and the baseline.

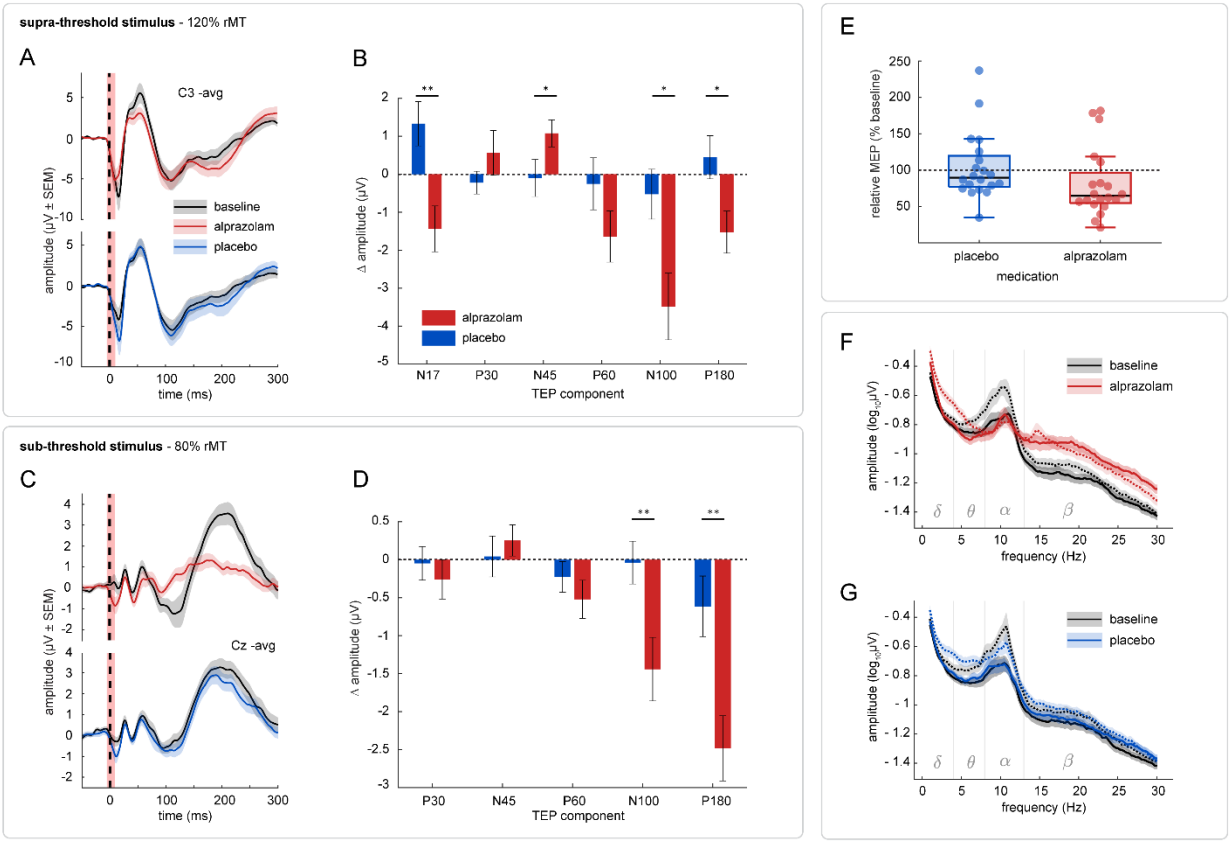

Figure 4.2 Effect of alprazolam. TEPs: (A, C) Group average signals from the most representative electrode for supra- and sub-threshold M1 TEPs are plotted at the baseline and after the medication (baseline: black, post alprazolam: red, post placebo: blue). Shaded areas represent the SEM. **(B, D)** Average modulations of peak amplitudes (± SEM) in supra- and sub-threshold M1 TEPs are illustrated with a bar plot (alprazolam: red, placebo: blue). Positive and negative values correspond to an increase and decrease of amplitude, respectively. In case of negative components, the original voltage measures were flipped to better convey the change induced by the medication. Asterisks denote the significance of the difference between the two sessions (* = $p < 0.05$; ** = $p < 0.01$). **MEPs: (E)** Boxplots show the modulation of peak-to-peak MEP amplitude evoked by supra-threshold stimulation of M1, values are expressed in % of baseline (alprazolam: red, placebo: blue). No significant effect of medication was found. **RS-EEG: (F, G)** Frequency spectra of RS-EEG recordings (central region) from the alprazolam and placebo session are visualized as the log10 of the average amplitude at frequencies 1 – 30Hz (baseline: black, post-alprazolam: red, post-placebo: blue). Full lines represent the signal with eyes open, dotted lines the signal with eyes closed. Shaded areas mark the SEM.

4.4.5. Alprazolam-induced reduction of N17 correlates with the increase in β band amplitude

To further investigate the connection between the TEP component N17 and the state of $GABA_A$ergic inhibitory system, we explored the relationship between the medication-induced change in N17 and the established RS-EEG markers. From the three tested RS-EEG measures, only the change in low β amplitude proved to be significantly correlated with the change in N17 (Fig. 4.4B). Moreover, we observed a different relationship between the two variables depending on the medication – while placebo showed no significant association ($r(18) = 0.01$, $t = 0.06$, adjusted $R^2 = -0.06$), a clear negative correlation was found in measures from the alprazolam session ($r(18) = -0.6$, $t = -3.21$, $p < 0.01$, adjusted $R^2 = 0.39$): greater increases in β were associated with a stronger decrease of the N17.

4.4.6. SICI leads to a selective suppression of M1 TEP components

SICI in the M1 was recorded before medication in both sessions using a paired-pulse TMS protocol. For this purpose, a sub-threshold CS (80 %rMT) was applied 2.5 ms before the supra-threshold TS (120 %rMT), and resulting MEPs and TEPs (CS-TS) were compared to measures evoked by the TS alone. As expected, SICI manifested as a reduction of the MEP peak-to-peak amplitude (Fig. 4.3C) that was suppressed in average by 74.94 ± 5.2 % in the baseline recording of the placebo session and by 75.21 ± 5.51 % in the baseline recording of the alprazolam session. In M1 TEPs, a significant reduction of amplitude was observed for components N17 ($F_{1,58} = 39.37$, $p < 001$), P60 ($F_{1,58} = 12.98$, $p < 001$) and N100 ($F_{1,58} = 10.7$, $p < 01$), and these changes were consistent across both baseline recordings (Fig. 4.3A,B). Mean amplitude modulation of all TEP components and the outcome of the statistical analysis are summarized in the Table 4.3.

The observed decrease in TEP amplitude was correlated to the decrease of MEPs. Preliminary data visualization revealed a possibly non-linear relationship between TEP and MEP variables, so we calculated Spearman's correlation coefficients for ranked data that proved significant for all three SICI-sensitive TEP components (Fig. 4.3D-F): N17 ($\rho = 0.39$, $t(38) = 2.64$, $p < 0.05$, adjusted $R^2 = 0.13$), P60 ($\rho = 0.54$, $t(38) = 3.96$, $p < 0.001$, adjusted $R^2 = 0.27$), N100 ($\rho = 0.55$, $t(38) = 4.08$, $p < 0.001$, adjusted $R^2 = 0.29$).

4.4.7. N17 SICI is correlated with changes induced by alprazolam

We postulated that if both the modulation of the N17 component of M1 TEPs by paired-pulse stimulation and the changes observed after alprazolam administration are due to $GABA_AR$ activation, both should be dependent on interindividual variations in the functional state of $GABA_AR$-mediated inhibition in the M1. To investigate this further, we evaluated the correlation between the N17 SICI produced by paired-pulse stimulation before medication, and the most prominent changes observed

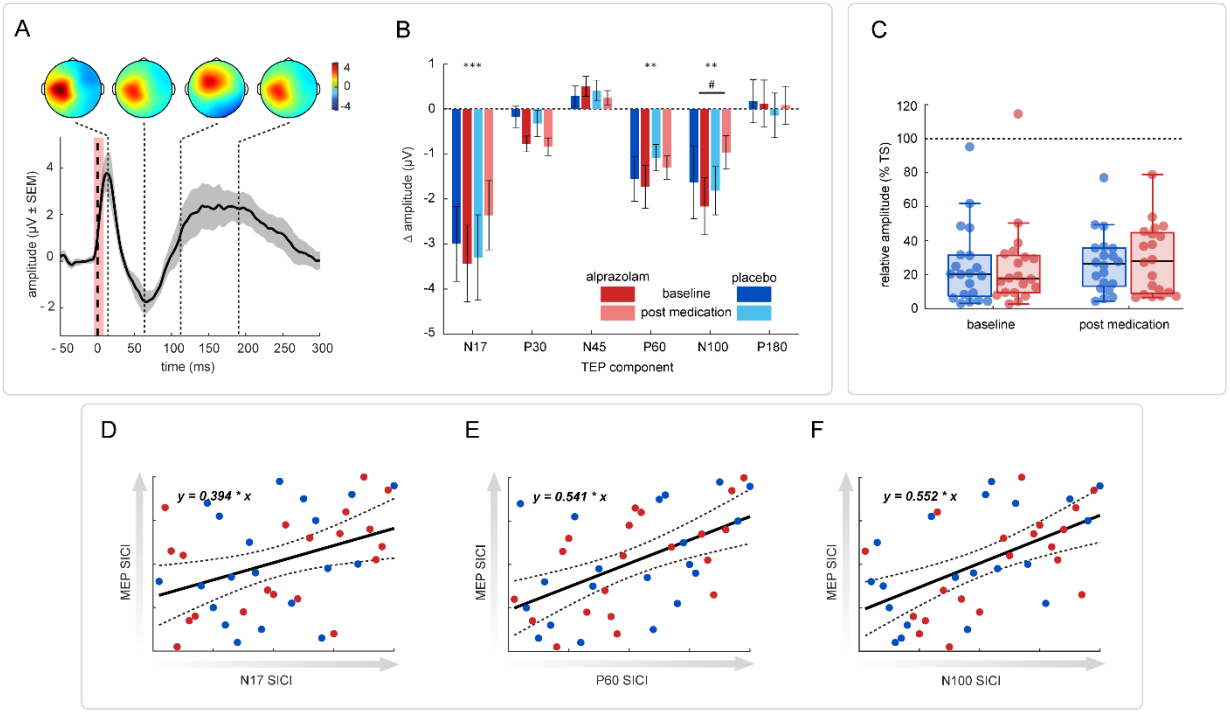

Figure 4.3 Effect of alprazolam. Effect of SICI. TEPs: (A) The time-course and topographic distribution of TEP SICI was obtained by point-by-point subtraction of the single-pulse TEP from the paired-pulse TEP over the whole explored time-window. The signal from C3 electrode is shown, the grey shaded area represents the SEM. The thick dashed line marks the TMS stimulus, the shaded pink area corresponds to the interval interpolated following the TMS artifact removal. Dotted lines mark latencies at which distinct topographical distributions of voltage change could be identified, as illustrated in the upper row. **(B)** The extent of TEP SICI at each TEP component was calculated as a subtraction of the TS TEP amplitude from the CS-TS TEP amplitude. The bar graph shows the average effect of SICI (µV ± SEM) separately for both experimental sessions at the baseline (dark colours) and following the medication (light colours; alprazolam: red, placebo: blue). In case of negative components, the original voltage measures were flipped to better convey the direction of change. Asterisks denote the significance of the change in baseline TEPs (** = $p < 0.01$; *** = $p < 0.001$), the hash sign shows the significance of the SICI x medication interaction (# = $p < 0.05$). **MEPs: (C)** MEP SICI before and after the medication is expressed in % of TS MEP (alprazolam: red, placebo: blue). **Correlation between the extent of MEP and TEP SICI: (D-F)** A significant correlation was found in ranked baseline data for SICI in MEPs and SICI in all three modulated TEP components (N17, P60, N100; alprazolam: red, placebo: blue).

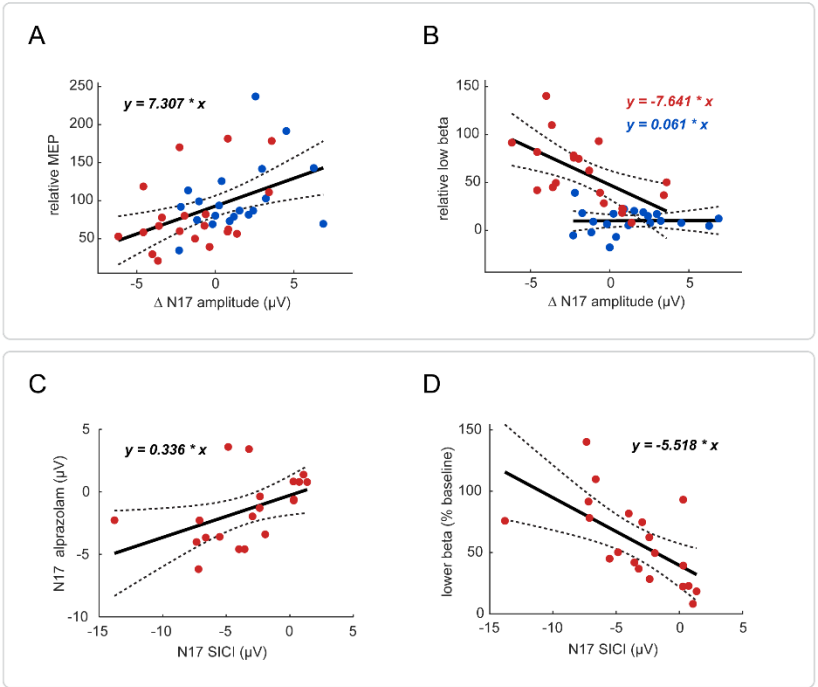

Figure 4.4 Correlational analysis of TEP component N17. (A) A significant linear correlation was found between the drug-induced modulation of N17 and the drug-induced modulation of MEPs. **(B)** In the alprazolam session (red), the modulation of N17 was found correlated to the modulation of low β amplitude, whereas no association was found for placebo (blue). The amplitude change of N17 is expressed as a difference from baseline (µV), the change of MEPs and low β as a relative amplitude (% of baseline). **(C)** The extent of N17 SICI was correlated with the alprazolam-induced modulation of N17 amplitude and **(D)** of the amplitude of lower β oscillations. N17 measures are expressed as a difference (µV), either from TS TEPs (SICI) or the baseline (alprazolam), low β as a relative amplitude (% of baseline).

after alprazolam. More precisely, we selected the alprazolam-induced reduction of N17 and the augmentation of the amplitude in the lower β band. A significant linear correlation was observed between N17 SICI and both measures (with the modulation of N17: $r(18) = 0.47$, $t = 2.28$, $p < 0.05$, adjusted $R^2 = 0.18$; with the modulation of lower β amplitude: $r(18) = -0.61$, $t = -3.3$, $p < 0.01$, adjusted $R^2 = 0.34$; see Fig. 4.4C,D). This indicates that subjects with a larger reduction of N17 following paired pulse stimulation also show a stronger modulation of N17 and β amplitude by alprazolam.

4.4.8. SICI tends to be reduced when $GABA_A$Rs are potentiated by alprazolam

As a last exploratory analysis, we investigated possible interactions between the effect of paired-pulse stimulation and the effect of alprazolam. There was no significant difference between the MEP reduction induced by paired-pulse stimulation after alprazolam medication (70.93 ± 4.6 %) compared to placebo (73.25 ± 3.97 %) (Fig. 4.3C). Similarly, no significant interaction was found between the type of medication and the effect of paired-pulse stimulation on most TEP components (Fig. 4.3B) with the exception of the N100, whose SICI was reduced by alprazolam and increased by placebo. A tendency in the same direction was also noted in the component N17. Mean observed changes in TEP SICI as well as the outcome of the statistical analysis are summarized in the Table 4.3.

peak	time	mean change		F statistic	df	p value	
		placebo	alprazolam				
N17	baseline	- 3.00 ± 0.84	- 3.44 ± 0.85	39.37	1, 58	< 0.001	***
	post med.	- 3.3 ± 0.95	- 2.36 ± 0.77	3.53	1, 54.01	0.07	
P30	baseline	- 0.18 ± 0.24	- 0.78 ± 0.18	3.09	1, 58	*n.s.*	
	post med.	- 0.32 ± 0.3	- 0.84 ± 0.2	0.49	1, 54.06	*n.s.*	
N45	baseline	0.29 ± 0.23	0.5 ± 0.22	3.52	1, 58	*n.s.*	
	post med.	0.41 ± 0.23	0.25 ± 0.19	0.77	1, 54.07	*n.s.*	
P60	baseline	- 1.56 ± 0.49	- 1.73 ± 0.48	12.98	1, 58	< 0.001	***
	post med.	- 1.08 ± 0.29	- 1.3 ± 0.26	0.01	1, 54.03	*n.s.*	
N100	baseline	- 1.63 ± 0.81	- 2.16 ± 0.63	10.7	1, 58	< 0.01	**
	post med.	- 1.82 ± 0.54	- 0.96 ± 0.37	5.89	1, 54	< 0.05	*
P180	baseline	0.17 ± 0.48	0.12 ± 0.52	0.61	1, 58	*n.s.*	
	post med.	- 0.14 ± 0.49	0.08 ± 0.42	0.32	1, 54.06	*n.s.*	

Table 4.3. Mean TEP SICI and corresponding statistics. TEP amplitude change was computed as the difference between the CS-TS TEP and the TS TEP, in the table represented in μV ± SEM. Positive numbers mark an increase of the amplitude and vice versa. Displayed statistics correspond to the effect of interest: at baseline we show the effect of stimulus, post medication we show the interaction between SICI and medication.

4.5. Discussion

4.5.1. TEP signature of pharmacological $GABA_AR$ activation

We investigated the impact of pharmacological activation of $GABA_ARs$ on the amplitude of TEPs evoked by stimulation of the M1, while also distinguishing M1 TEPs elicited by stimulation at sub- and supra-threshold intensities. Furthermore, three established RS-EEG measures were obtained to further characterize the effect of alprazolam and explore their relation to drug-induced changes in TEPs.

We observed a specific alprazolam-induced modulation of both early and late components of supra-threshold M1 TEPs, whereas only late components were significantly affected in sub-threshold M1 TEPs. The alprazolam-induced modulation of the late N100 and P180 components was robust, consistent across TEP datasets, and clearly reflects changes in brain function resulting from a global increase in $GABA_AR$-mediated inhibition. Yet it does not necessarily provide specific information on the state of inhibition in the brain network targeted by TMS. Indeed, there is a growing body of evidence indicating that the N100-P180 complex can be mostly attributed to the brain activity evoked by peripheral sensory stimulation [154, 160, 178, 184, 304]. This is compatible with the notion that these late components relate to the vertex potential typically evoked by transient sensory stimuli [161]. The magnitude of this vertex potential can be expected to depend on the excitability of multiple brain networks as well as the state of populations of spinal or peripheral neurons influenced by $GABA_AR$-mediated neurotransmission. Indeed, previous studies have shown a benzodiazepine-induced reduction of both auditory- and somatosensory-evoked vertex potentials [319-321]. Therefore, when considering sub-threshold M1 TEPs, the alprazolam-induced modulation of N100 and P180 should not be interpreted as a direct measure of cortical inhibition in the stimulated brain network.

On the other hand, the topography of the late components elicited by supra-threshold M1 TEPs differs from that of sub-threshold M1 TEPs, indicating that additional processes are triggered by supra-threshold stimulation of the motor cortex [183, 192, 304, 322], possibly related to the activation of the motor brain network and/or the somatosensory response to the TMS-evoked muscular contraction. The N100 component of supra-threshold M1 TEPs was previously associated with motor inhibition [147, 189-191] that is possibly mediated by local $GABA_BRs$ [186]. Therefore, the N100 reduction following administration of alprazolam might reflect both a suppression of unspecific sensory-evoked activity and a decrease in local sensorimotor inhibition following a weaker M1 activation.

The earlier components of sub-threshold M1 TEPs were not significantly affected by alprazolam as compared to placebo. This lack of effect could be related to the fact that these TEP components are relatively small and show substantial inter-subject variability. In contrast, the early components of supra-threshold M1 TEPs were significantly modulated by alprazolam. In line with the reports of previous studies exploring the effect of benzodiazepines on TEPs [186, 194], alprazolam was associated

with an increase of the N45 component. In past, this component was also found suppressed by a competitive $GABA_AR$ antagonist selective for α5 receptor subtypes [188], whereas dextromethorphan, an antagonist of the N-methyl-D-aspartate receptor for glutamate (NMDAR), led to its augmentation [187]. Therefore, our results add to the accumulating evidence that N45 depends on the balance between $GABA_AR$-mediated inhibition and NMDAR-meditated excitation.

Most remarkably, alprazolam significantly reduced the component N17 of supra-threshold TEPs (labelled N15 or N18 in other studies [176, 180]) when compared to the effect of placebo. This component is of high interest as it likely reflects genuine cortical activity directly evoked by TMS within the stimulated motor network. It is target-specific, seems to be little affected by somatosensory- and auditory-evoked potentials, and its very early latency excludes any contribution of the recurrent somatosensory response to the contraction of the contralateral hand muscle [184, 185, 304]. Furthermore, several previous studies located the sources of N17 to the M1 and/or adjacent nodes of the sensorimotor network [119, 130, 146, 179, 185]. Therefore, since our data clearly shows that N17 is dependent on the state of $GABA_AR$-mediated neurotransmission, the extent of its modulation may be directly linked to the performance of the $GABA_A$ergic inhibitory system within the target brain network. This claim is further supported by the significant correlation between the drug-induced change of the N17 amplitude and the amplitude of MEPs, which confirms the association of this component to the motor output of the M1 and hints on its possible relation to the TMS-evoked cortico-spinal activation.

4.5.2. RS-EEG signature of pharmacological $GABA_AR$ activation

As expected, all three evaluated RS-EEG markers were sensitive to the effects of alprazolam as compared to placebo, the increase of $GABA_AR$-mediated inhibition manifesting as a clear augmentation of lower β-band amplitude and reduction of AAC and SE. In addition, the effect of alprazolam on the amplitude of N17 of supra-threshold TEPs was strongly correlated with the alprazolam-induced modulation of the amplitude of lower β oscillations over central regions.

The increase in β represents an established RS-EEG marker of the benzodiazepine effect [305, 307, 323] and while the origin of this emerging activity has not been reliably identified, it is not unlikely that motor networks significantly contribute to its generation. Oscillatory activity in the β band was in the past linked predominantly to the function of sensorimotor cortices [324], where it was proposed to reflect a process maintaining the ongoing postural setting while inhibiting new movements [325]. Increased β activity, either spontaneous or induced by repetitive brain stimulation, was associated with the slowing of voluntary movements [326, 327], which indicates that it might be associated with states of lower motor excitability. Provided that the magnitude of the TEP component N17 reflects local cortical activation of the motor cortex and/or nearby connected areas, our data support the idea

that both the alprazolam-induced increase in β oscillations over central regions and the alprazolam-induced decrease of the N17 depend on the functional state of $GABA_AR$-mediated inhibition in the motor cortex.

Interestingly, the alprazolam-induced reduction of N17 was not correlated to the other two RS-EEG markers. In case of AAC, the measure reflects the attenuation of α oscillations over occipital regions where α band activity – likely unrelated to motor processing – is most pronounced [305]. In the case of SE, the measure represents the slope of the 1/f-like background component of the EEG frequency spectrum, which is related to the level of arousal and consciousness [314, 328, 329] and is thought to reflect the ratio of global excitatory and inhibitory neurotransmission [330]. The N17 component and both of these RS-EEG markers are thus likely to reflect activity of different brain networks having distinct cytoarchitectural and functional properties. The lack of correlation between the effect of alprazolam on N17 and its effect on the AAC and the SE would indicate that, across individuals, these networks have independent dynamics leading to independent variations in their sensitivity to GABAergic inhibition. Therefore, it might be advantageous to combine TEPs and different RS-EEG measures when evaluating the pharmacologically induced increase in $GABA_AR$-mediated inhibition, as they likely provide complementary information.

4.5.3. TEP SICI and its relation to the effect of alprazolam

In the second part of the study, we activated local inhibitory circuits in the M1 using a sub-threshold conditioning stimulus producing SICI. In both baseline recordings, SICI manifested as a significant reduction of MEP amplitudes, and a concomitant amplitude suppression of TEP components N17, P60 and N100. Interestingly, the spatiotemporal distribution of the SICI effect bore a striking resemblance to the PCA component identified by Biabani et al. [185], which allowed to distinguish real M1 TEPs from the brain response evoked by sham stimulation. Assuming that such component can be attributed to the activity directly evoked by TMS in the stimulated cortical area, our findings suggest that the conditioning stimulus indeed led to a suppression of this genuine activity, likely due to a local increase in $GABA_AR$-mediated inhibition.

Across individuals, the reduction of MEP amplitude was correlated with the reduction of all three TEP components, corroborating the assumption that changes in the magnitude of these TEP components can be linked to changes in corticospinal motor output. Since we previously identified the N17 as the component most reliably reflecting the changes in the $GABA_A$ergic neurotransmission within the M1, we further explored its modulation by SICI in relation to its modulation by alprazolam and found, across individuals, a significant linear correlation between the N17 reduction induced by alprazolam and the N17 reduction induced by paired-pulse stimulation. Furthermore, we found a similar relationship between N17 SICI and the alprazolam-induced increase in low β band oscillations.

In other words, subjects that showed a stronger effect of pharmacological activation of $GABA_A$Rs also showed a stronger effect of SICI, indicating that both phenomena are at least partially mediated by the same mechanism. This further strengthens our assertion that the N17 component can be linked to the functional state of $GABA_A$R-mediated inhibition within the motor cortex.

Our observations of TEP SICI are only in partial agreement with previous studies. These mostly reported a suppression of P60 but also found a decrease of P30 [259, 260, 300], and a decrease [259] or an increase of N45 [260, 261, 300]. In a very recent publication, Rawji et al. additionally showed a suppression of N15 (here N17) and P180 [261]. Contrary to all above-mentioned studies, the early study of Paus et al. reported no effect of SICI in TEPs [174], whereas two more recent studies only found a reduction of late TEP components N100 and P180/P300 [44, 194]. These discrepancies may be explained by the variability of stimulation parameters as well as the analysis pipeline to extract TEP parameters, which ranged from a point-by-point comparison across all electrodes to peak extraction from electrodes of interest in predefined time intervals varying across studies. Here, for each TEP component, the electrodes of interest were selected based on the mean component topography, to prioritize the most prominent generators while possibly neglecting other sources contributing to the final voltage distribution of TEPs. Furthermore, our analysis technique allowed us to extract the amplitude at subjects' peak latency and thereby address the issue of inter-subject variability in the TEP temporal profile [114], which is especially important when evaluating early and very transient TEP components.

Finally, we examined whether the local inhibition induced by paired pulse stimulation is affected by the global activation of $GABA_A$Rs produced by alprazolam. Contrary to previous studies that reported an increase of SICI in MEPs following the administration of positive $GABA_A$R modulators [258, 331-333], we did not observe any significant change of MEP SICI after alprazolam. When considering the influence of alprazolam on TEP SICI, our results are in line with those reported by Premoli et al. who combined paired-pulse stimulation with the administration of diazepam and found a significant reduction of SICI on the N100 component [194]. However, based on the effect of alprazolam we observed in supra-threshold M1 TEPs, we speculate that the observed modulation of N100 SICI might be to a great extent due to the alprazolam-induced suppression of single-pulse N100 amplitude rather than a reduction of the SICI effect itself.

4.6. Conclusion

In the present study, we described the effect of increased $GABA_A$R-mediated inhibition on specific components of M1 TEPs using both pharmacological and paired-pulse activation of $GABA_A$R inhibitory circuits. In supra-threshold M1 TEPs, we identified an early component N17 that was directly associated with the motor output and was found susceptible to both alprazolam and SICI. The

modulation induced by both manipulations was correlated across subjects. In addition, we linked the alprazolam- and SICI-induced reduction of N17 to the increase in lower β band oscillations observed following the administration of alprazolam, indicating that changes in both measures correspond to the increased $GABA_AR$ inhibitory transmission in the stimulated motor cortex and closely connected areas of the sensorimotor brain network. Taken together, we show that the N17 component of supra-threshold M1 TEPs is sensitive to $GABA_AR$-mediated changes in local cortical excitability. Therefore, pharmacological or paired-pulse modulation of this component could be used in clinical settings as a non-invasive biomarker to assess the functional state $GABA_AR$ neurotransmission in sensorimotor cortices. TEP recordings may be further supplemented by RS-EEG measures (lower β amplitude, AAC, SE) to assess the $GABA_AR$ inhibition more globally.

4.7. Supplementary materials

This chapter provides detailed information about the methodology used for pre-processing and data analysis. The methodology description is divided into three sections: First, we describe the pre-processing pipeline of TEPs with particular emphasis on ICA, providing examples of ICA components considered as artifactual and their characteristic features. Second, we introduce microstate analysis of TEPs and demonstrate its utility as a source of prior for peak amplitude extraction. Third, we describe automatized processing of MEPs that allows to identify and exclude trials with excessive baseline activity while minimizing subjective input.

In the fourth section, we present TEPs obtained by stimulation of the left AG that were recorded in addition to TEPs from the M1, MEPs and RS-EEG. Similarly to these measures, we evaluated the effect of alprazolam on AG TEPs and the results of the analysis are presented here. Since this part of the study does not significantly contribute to the overall conclusions we make, for the sake of clarity it was not included in the main publication.

4.7.1. Pre-processing of TMS-evoked potentials

Three types of TEPs (conditions) were recorded in the present study: M1 TEPs obtained by supra-threshold stimulation, M1 TEPs obtained by sub-threshold stimulation, and AG TEPs. Two TEP datasets of each condition were obtained in each of the two experimental sessions, one at the baseline and the other following the medication (alprazolam or placebo). All TEPs were recorded using the NeurOne system (Bittium) with 32 open-circle electrodes (Multitrodes, EasyCap), sampling rate of 20 kHz and mastoid electrodes serving as reference.

The raw signal was pre-processed in several automatized steps:

1. Signal was re-referenced to Cz, mastoids were removed, and the signal was re-referenced again to the average calculated from 30 remaining electrodes
2. DC shift was removed from the whole recording
3. Signal was segmented into epochs relative to TMS stimulus [-1 2]s
4. TMS artifact was cut out between [-0.005 0.01]s and replaced using cubic interpolation
5. Signal was down-sampled by 10, so the size of a single epoch corresponded to 6000 bins
6. Linear trend was filtered out from individual TEP epochs
7. Single trials were split into appropriate categories, missed trials identified during the recording session were removed
8. Data were visually checked for bad channels that were removed and interpolated using the average signal of the 6 surrounding electrodes (this happened for 1 channel in 3 datasets out of 40)

First round of ICA. In the next step, we calculated a square matrix of 30 independent components (ICs), unless a channel was previously interpolated – in that case we lowered the number of components by one. The ICs were visually inspected, and 1-2 ICs (rarely up to 4) were identified as containing the artifact caused by muscular contraction due to superficial TMS stimulation. Such artifact can be easily spotted in the single-trial time-course as a high-voltage deflection with a decay tail and a sharp peak at 10 ms, which corresponds to the limit of the interpolated interval. It shows typical lateralized topography that varies across stimulation sites as well as across subjects according to their anatomy (Fig. 4S.1A).

Identified components were removed, and new signal was created based on the remaining ICs. It was then filtered with a Butterworth bandpass filter (4^{th} order) to remove extreme frequencies, keeping values between 0.1 and 80 Hz. The line noise at 50 Hz was removed with a FFT notch filter cutting out frequencies between 48-52 Hz with a 2 Hz wide Hanning function. Next, the epochs were cropped from [-0.75 0.75]s relative to the stimulus in order to remove possible distortion caused by frequency filters. Finally, each dataset was visually inspected trial-by-trial and epochs that included isolated bursts of high-amplitude activity, extreme drifts etc. were discarded.

Second round of ICA. In the second round, we calculated a rectangular ICA matrix for the total number of channels (30) minus the number of ICs removed in the previous round of ICA. We also extracted specific features of each IC, such as its average time-course and the frequency spectrum up to 45 Hz. As a preliminary step, we used MARA [278], a linear classifier originally trained on adult EEG data, to identify components possibly containing an artifact. Selected ICs were then individually inspected by an experienced researcher. Based on their features, these ICs were classified either as

mixed (containing signal of likely cerebral origin) and retained, or assigned to one of the following categories and removed: (1) eye movements such as blinking and saccades (Fig. 4S.1B); (2) tonic muscular activity (Fig. 4S.1C); (3) decay artifact (Fig. 4S.1D); (4) electrode noise (Fig. 4S.1E); (5) ringing artifact introduced by frequency filters (Fig. 4S.1F).

Final TEP epochs, composed of the signal of remaining ICs, were then baseline corrected by subtracting from each timepoint the average amplitude of [-0.2 -0.005]s relative to the stimulus and averaged, thus resulting in a single TEP waveform per subject per condition.

4.7.2. Microstate analysis as a source of prior for TEP peak amplitude extraction

All TEPs were evaluated between [0.01 0.3]s post stimulus. In the first step, baseline TEPs of each category were characterized using microstate analysis, a method that considers the temporal evolution

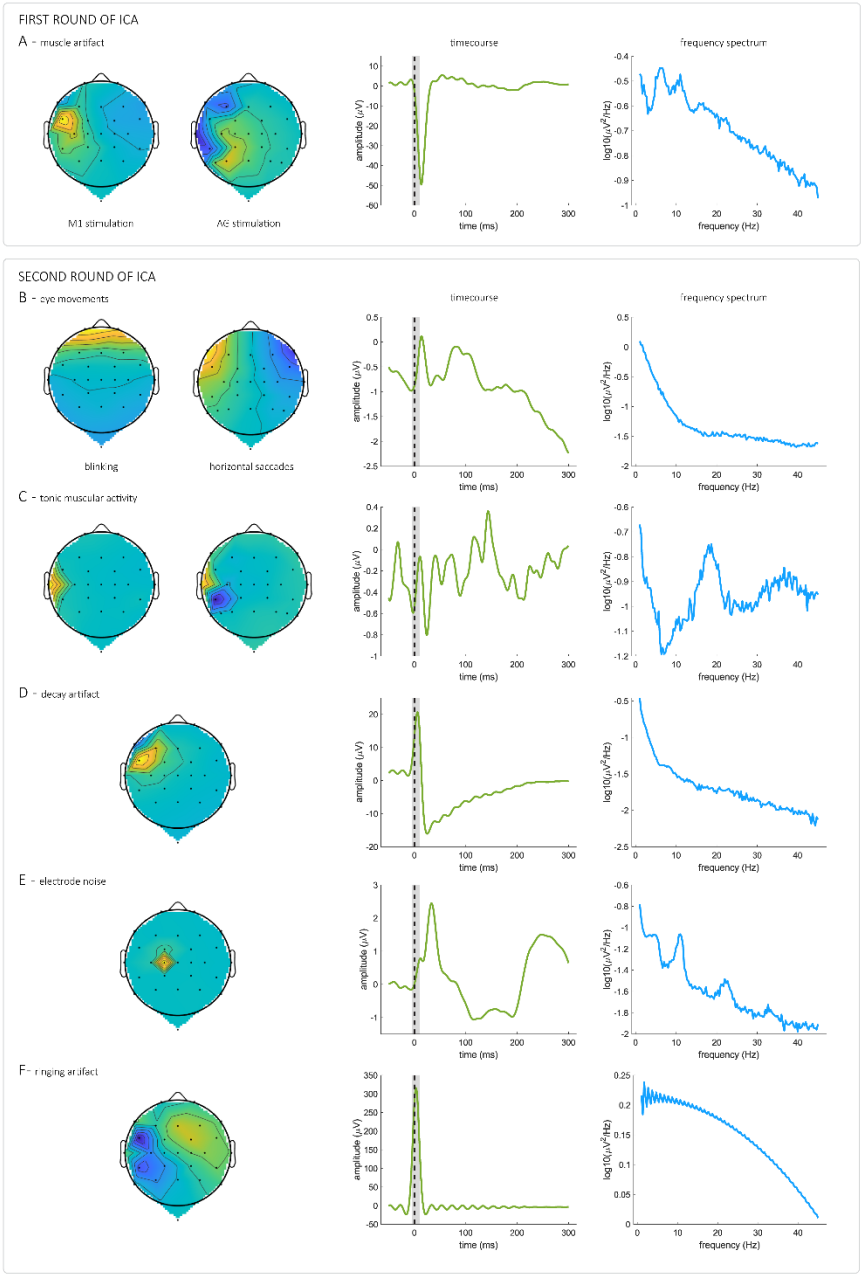

Figure 4S.1 TEP artifacts identified by ICA.
(A) Muscular artifact.
(B) eye blinks (left) and horizontal eye movements (right).
(C) Tonic muscular activity.
(D) Decay artifact.
(E) Electrode noise.
(F) Ringing artifact.

of the whole scalp topography and identifies discrete time intervals when a single topographic pattern dominates [271]. It relies on the assumption that two different distributions of voltage in the same dataset represent the activation of two distinct sets of cortical sources [266]. In practice, all timepoints in a group average dataset are subjected to a clustering process, which defines a number of microstate classes and labels temporally adjacent timepoints with the most fitting class, thereby forming non-overlapping microstate intervals [282]. These segments closely match observed TEP components and in evoked potentials they were suggested to represent a sequence of discrete processing steps triggered by the stimulation [271]. Importantly, microstate analysis evaluates TEPs normalized by their GFP, i.e. the mean amplitude across all electrodes, thus limiting the effect of the inter-subject variability in the response strength. Moreover, by considering the whole voltage landscape, the method deals with the bias introduced by the choice of a reference electrode.

To perform the microstate analysis, we used the open-access Matlab toolbox Ragu and followed the recommended pipeline [280]. For each TEP condition at the baseline, we obtained a sequence of microstate class maps that were associated with individual TEP components (a detailed topographic analysis of baseline TEPs and their comparison was previously published in a separate article [304]). We then used spatiotemporal features of these microstates to inform the subsequent semi-automatic extraction of TEP peak amplitude (Fig. 4S.2). The duration of each microstate provided a base for the calculation of the default width of the extraction window that was kept identical across subjects and tested datasets. The topographic pattern of the microstate was used to identify three electrodes of interest (EOIs) that corresponded to the spatial maximum of the associated TEP component. The signal of these EOIs was averaged and all compared datasets from one subject/condition were plotted together within the exploration window. The microstate latency was used as the starting window latency that was adjusted manually to fit TEP peaks of the individual subject, thus accounting for the substantial inter-subject variability of TEP temporal profile. Finally, local amplitude maxima of all compared datasets (or minima, in case of negative components) were automatically measured in the exploration window. All above mentioned steps were performed using in-house written Matlab scripts.

Using this approach, we extracted a single value for each subject, tested dataset and TEP component, thereby substantially reducing the number of comparisons necessary for the statistical analysis. We chose to evaluate the significance of amplitude changes for each TEP component separately using a linear mixed model that allowed individual variability in the intercept but obtained data could have been assessed by any other classic model. Fig. 4S.3 provides an overview of microstate topographies and identified EOIs for all components of each evaluated TEP condition.

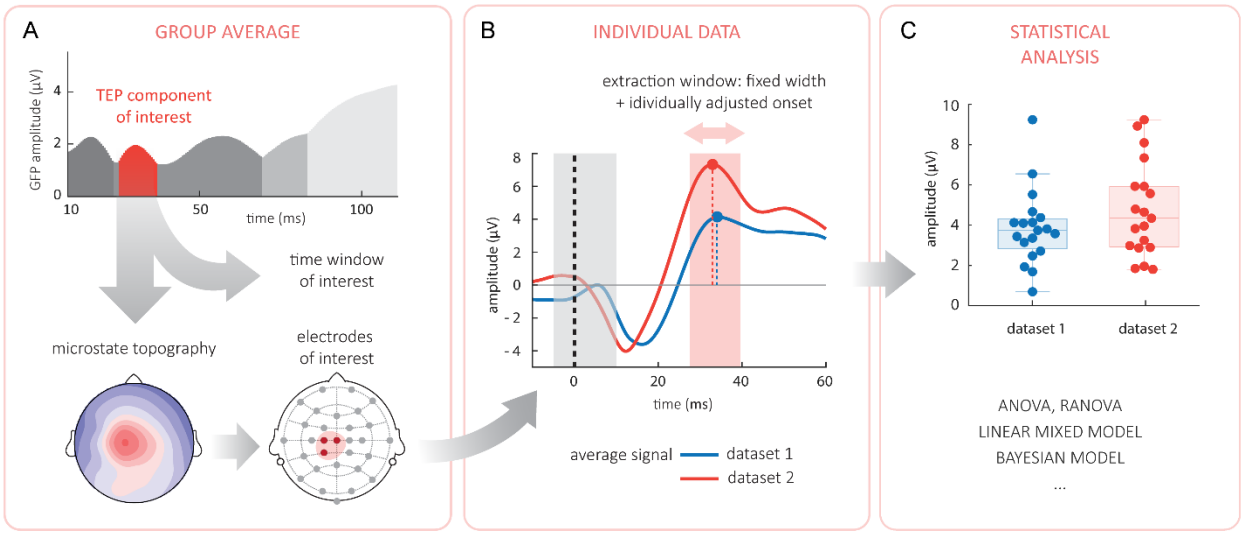

Figure 4S.2 TEP peak amplitude extraction. (A) The result of clustering that attributed one microstate class to each TEP component (visualized as distinct peaks in the GFP of the average signal). Mean microstate topography was used to identify EOIs, latency and the width of the exploration window attributed to the evaluated component. **(B)** The interactive plot displaying at the same time the averaged EOI signal of all compared datasets of a single subject. The onset of the exploration window is manually shifted to include all local peaks. Thereby extracted values can be then included into any type of classic statistical analysis, as visualized in the panel **C**.

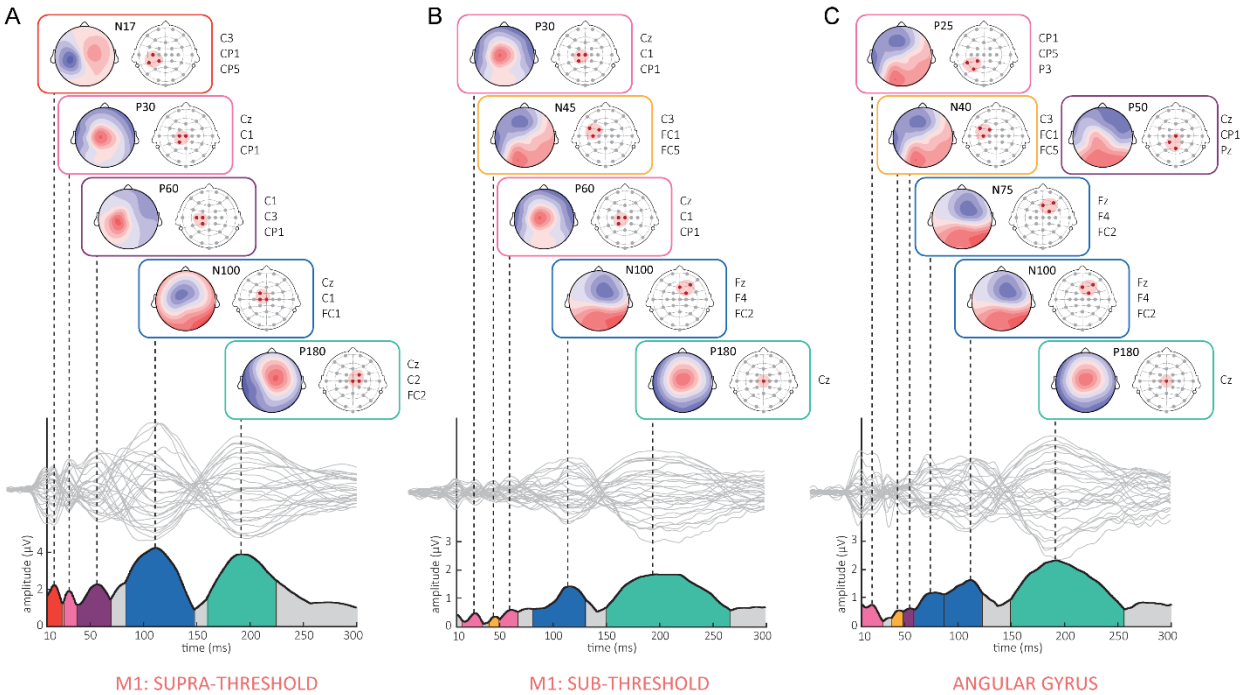

Figure 4S.3 Microstate topographies and EOIs of TEP components. Each vertical panel corresponds to one TEP condition: A - supra-threshold M1 TEPs; B - sub-threshold M1 TEPs; C - AG TEPs. In the bottom part, the GFP of the average baseline TEP is shown and the duration of microstates assigned to TEP components is shaded in corresponding colors. In the middle, average baseline signal from individual electrodes is plotted in light gray and dashed vertical lines mark peak latencies of TEP components. In the upper part, microstate class maps are linked to each TEP components and EOIs are visualized at the EEG layout, labels displayed on the side. N45 in supra-threshold M1 TEPs was not identified therefore the spatiotemporal features of N45 in sub-threshold M1 TEPs were used for the amplitude extraction.

4.7.3. Pre-processing of motor-evoked potentials

MEPs were recorded using an EMG system connected to the neuronavigation (TMSi MOBI, sampling rate 1024Hz) in parallel to TEPs when delivering the supra-threshold stimulus over the M1. Raw EMG signals were automatically pre-processed in the following steps:

1. Signal was corrected for DC shift
2. Frequencies below 4 Hz were filtered out with a Butterworth high-pass filter (4^{th} order)
3. Signal was segmented into epochs relative to TMS stimulus [-0.2 0.4]s
4. Linear detrend was applied to individual epochs
5. Single trials were split into appropriate categories, missed trials identified during the recording session were removed

In the next step, we identified and discarded trials with excessive baseline activity, as it might indicate a state of increased excitability, possibly of sub-cortical origin. To this end, we used an in-house written Matlab script that automatized this procedure, thereby minimizing the subjective input. The cleaning comprised two distinct steps. First, a root mean square (RMS) value of the baseline was calculated for each trial and epochs whose RMS exceeded the value of mean RMS ± 3 SD were discarded. The process was then repeated in remaining epochs until no outliers were identified. Second, an arbitrary threshold was selected based on normally observed EMG noise (we set it at ± 15µV) and epochs showing larger amplitude at the baseline were also excluded. An output figure obtained after the cleaning of a single dataset is shown in Fig. 4S.4.

Finally, we baseline-corrected the signal by subtracting the mean amplitude of the interval between [-0.2 0]s relative to the stimulus and extracted the peak-to-peak MEP amplitude at single trial level. Mean values were calculated for each subject/tested dataset and included in the statistical analysis.

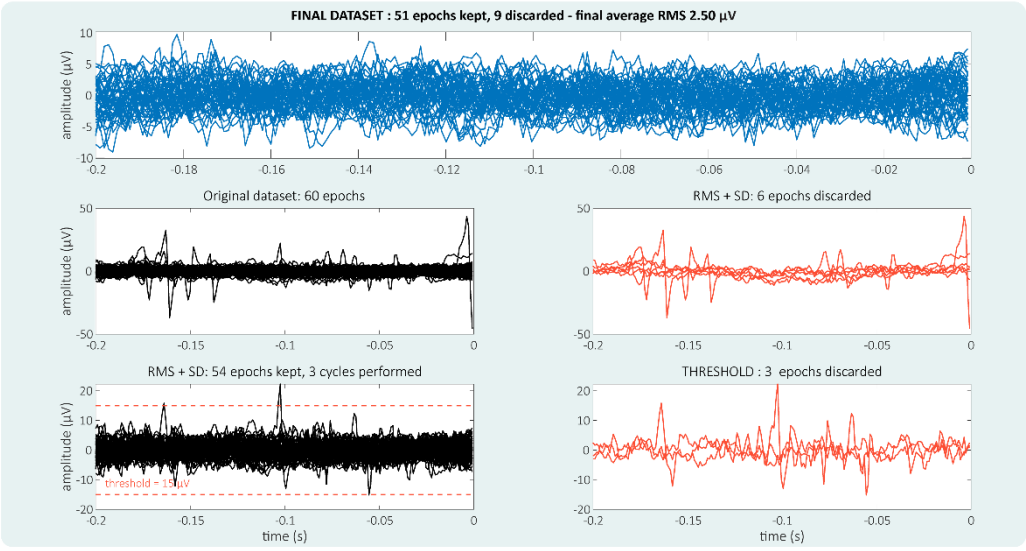

Figure 4S.4 Example of the output figure of the MEP cleaning process.

4.7.4. TMS-evoked potentials from the angular gyrus

AG TEPs. The stimulation target in the left AG was determined in the individual MRI using the position of the STS and the intraparietal sulcus (Fig. 4S.5A). Using neuronavigation, the coil was positioned with the handle pointing downwards and 10° towards the midline, thus placing the coil axis perpendicularly to the STS and across the AG (Fig. 4S.5B). 60 TMS stimuli of 100% rMT were delivered over the target in a single block with a variable inter-trial interval (4– 6 s) while simultaneously recording EEG. At the baseline (before any medication), AG TEPs had a distinct spatiotemporal profile composed of early components P25, N40, P50 and N75 followed by late components N100 and P180 (Fig. 4S.5C). While the early components were clearly different from those observed in M1 TEPs, the N100-P180 complex showed features generalized across target sites (for a detailed analysis of baseline AG TEPs see [304]).

The effect of alprazolam. The peak amplitude of individual TEP components served as the main outcome variable when evaluating the effect of medication on AG TEPs. Mean observed changes and the outcome of the statistical analysis are summarized in Table 4S.1. Like in sub-threshold M1 TEPs, only late components N100 and P180 of AG TEPs were clearly suppressed by alprazolam as compared to placebo, while earlier components showed no significant change in amplitude (Fig. 4S.5D-E).

stimulus	peak	mean change in amplitude		F statistic	df	p value	
		placebo	alprazolam				
	P25	- 0.30 ± 0.36	0.31 ± 0.36	1.40	1, 18.54	*n.s.*	
	N40	- 0.31 ± 0.19	0.02 ± 0.27	1.02	1, 18.54	*n.s.*	
AG	**P50**	- 0.13 ± 0.23	- 0.69 ± 0.26	2.64	1, 18.54	*n.s.*	
100 %rMT	**N75**	- 0.35 ± 0.42	- 0.14 ± 0.35	0.17	1, 18.47	*n.s.*	
	N100	- 0.70 ± 0.36	- 1.74 ± 0.46	5.07	1, 18.31	< 0.05	*
	P180	- 0.20 ± 0.47	- 3.18 ± 0.73	12.76	1, 18.54	< 0.01	**

Table 4S.1 Mean change in TEP amplitude and corresponding statistics. Amplitude change was computed as the difference between measurement post-medication and the baseline, in the table represented in μV ± SEM. Positive numbers mark an increase of the amplitude and vice versa, in case of negative components original voltage measures were multiplied by -1.

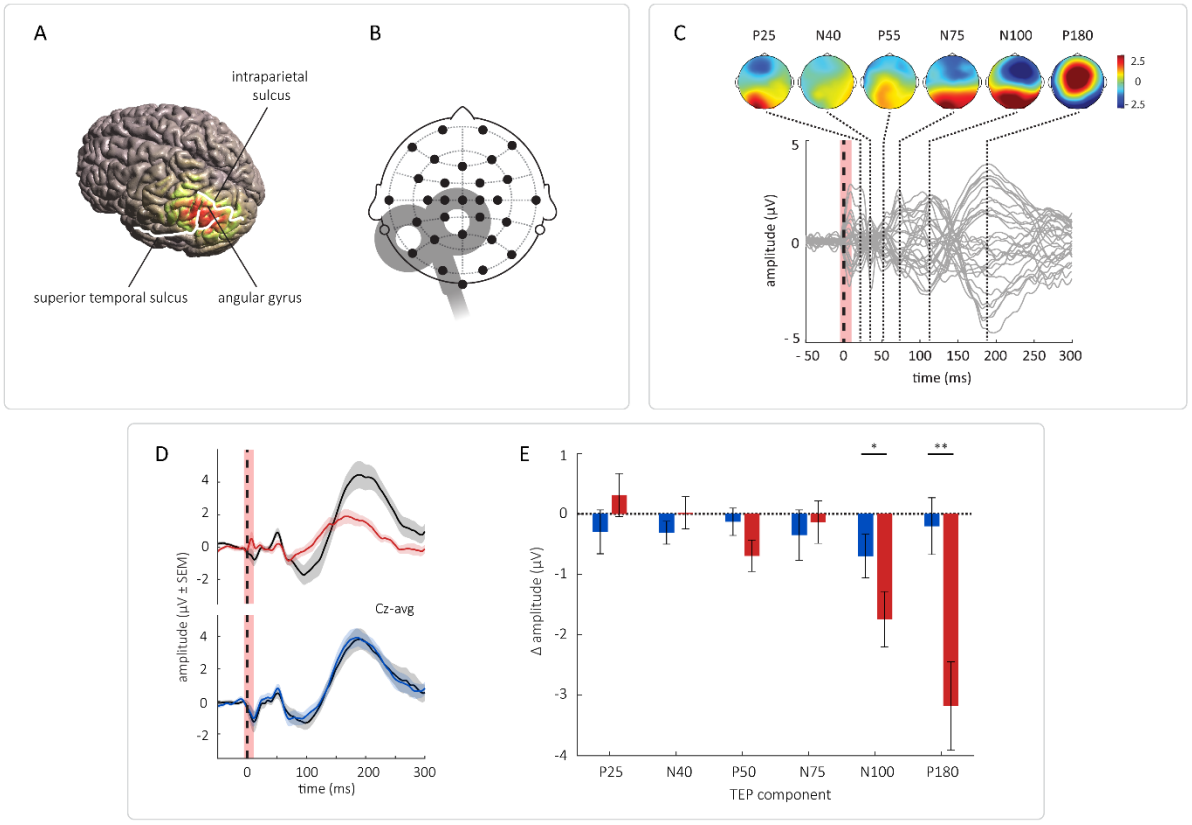

Figure 4S.5 AG TEPs. (A) A brain model showing the spread of evoked magnetic field across the cortex when stimulating the left AG. Anatomical landmarks are highlighted in white. **(B)** An approximate placement of the TMS coil over the head showing the EEG layout. **(C)** AG TEPs in a baseline recording of one experimental session. Grey traces represent the signal of all electrodes recorded at the baseline in the placebo sessions (there were no substantial differences between baseline TEPs of both sessions), TMS stimulus is marked by thick black dashed line, interval interpolated following the removal of TMS artifact is shaded in pink. Dotted black lines mark peak latencies of TEP components, associated topographies are shown in the upper part of each figure. **(D)** Group average TEPs before and after the medication from the most representative electrode (Cz). Baseline: black, post alprazolam: red, post placebo: blue. Shaded areas represent the SEM. **(E)** Modulation of peak TEP amplitude. Bar height corresponds to the mean change ± SEM. Positive numbers mark an increase of the amplitude and vice versa, in case of negative components the original voltage measures were flipped to better convey the change induced by the medication. Asterisks denote the significance of the difference between the two sessions (* = $p < 0.05$; ** = $p < 0.01$).

5. Exploring the properties of the left angular gyrus using TMS-evoked potentials

5.1. Abstract

The AG is involved in numerous cognitive processes and its structural alterations have been reported in multiple neuropsychiatric diseases. Because abnormal excitability or connectivity of cortical hubs such as the AG could precede structural alterations and clinical symptoms, there is a need for diagnostic tools assessing the functional state of these brain regions. The combination of TMS and EEG can provide such functional readouts by probing how the cortex responds to direct stimulation.

The aim of the presented study was to characterize TEPs elicited by AG stimulation, determine optimal stimulation parameters, and identify the TEP biomarkers of AG function. In 19 subjects, we recorded AG TEPs using four TMS orientations (defined by coil placement and current direction) and three intensities and compared their spatiotemporal features using topographic dissimilarity and microstate analyses. We also explored the link between AG TEPs and TMS-evoked muscle activity.

The early AG TEP components of interest (P25, N45) showed topographic variability dependent on tested stimulation parameters. The P25 topography was sensitive to TMS orientation and less to intensity, whereas the N45 topography was highly dependent on the coil placement and intensity, while the current direction had little impact. TMS-evoked muscular activity showed similar tendencies and the dominant topography of N45 was strongly related to this muscular activity, indicating that the component may reflect somatosensory-evoked responses to this peripheral activation.

We conclude that the earliest AG TEP component P25 likely reflects neural processes triggered by direct AG activation and could provide an index of local excitability. However, N45 must be interpreted with caution as it may mostly reflect peripherally evoked activity. The coil orientation can be optimized to minimize muscular contractions.

5.2. Introduction

Located right at the junction of temporal, occipital and parietal lobes, the AG represents a highly connected cortical hub [220, 221, 334] that is implicated in a vast range of cognitive processes (for an exhaustive review see [222]). It integrates converging multimodal input from diverse brain regions and is thought to bind this input with existing concepts and contexts, thereby allowing its correct categorization and, ultimately, interpretation [222-224]. As a core node of the DMN, the AG contributes to the resting-state brain activity involving episodic simulation and manipulation with previously acquired knowledge [230-232, 335]. The left AG in particular has been associated with verbal semantic processing [336-338] and episodic memory retrieval [339-341], which relates to its strong connectivity to the hippocampal region [211, 215].

Due to its widespread involvement in higher cognitive processes, any damage or functional impairment of the AG inevitably impacts cognitive performance [342]. At the same time, structural and

connectivity abnormalities of the AG have been reported in a great variety of neurologic and psychiatric disorders including Alzheimer's disease [343-345], schizophrenia [346, 347], amyotrophic lateral sclerosis [348, 349], and Huntington's disease [350]. It is likely that these pathologic alterations are preceded by more subtle changes in local cortical excitability and connectivity. Therefore, there is a strong incentive to explore functional properties of the AG and associated brain networks, particularly in early-stage patients and preclinical populations.

However, the majority of previous studies used fMRI to assess the AG in the context of large-scale brain networks. This imaging technique approximates indirectly the activity of target brain regions by measuring the hemodynamic brain response [351, 352], so the signal only shows relatively slow fluctuations of cortical activation [353]. By consequence, fMRI does not allow to capture the underlying neural dynamics occurring at the millisecond timescale that could provide specific information about the local excitability or the causal connectivity within stimulated brain networks [92].

It is now possible to obtain such measures by combining the spatial precision of TMS with the high temporal resolution of EEG. While TMS stimulates cortical neurons of the selected region [46, 50], EEG records their immediate response to this TMS perturbation and the subsequent spread of evoked activity through the brain [107, 108]. The magnitude and spatiotemporal distribution of TEPs can be thus used to evaluate the excitability of the stimulated cortex [108, 180, 354] and gain insight into the causal connectivity within corresponding brain networks [124, 126, 127, 355].

To this date, only few TMS-EEG studies have targeted the AG and the experimental settings they used, including the exact location of the site of stimulation, varied from one study to another [114, 160, 184, 203, 235, 304]. Nevertheless, the available data indicate that it is possible to record AG TEPs that are stable across sessions and have spatiotemporal profiles specific for individual subjects [114]. Furthermore, EEG source reconstruction revealed a target-specific propagation of activity from the stimulated AG across different nodes of the DMN, thereby hinting at the utility of AG TEPs for the evaluation of this resting-state network [235].

Taken together, AG TEPs show the potential to become a clinically relevant tool for the assessment of local cortical excitability of the AG as well as the perturbational connectivity in the DMN. But before employing it to study pathological states, it is crucial to characterize the physiological profile of AG TEPs, to identify the components that genuinely reflect the activity within the stimulated network, and to find the optimal combination of stimulation parameters. It is generally agreed that the stimulation intensity as well as the orientation and direction of the magnetic field in relation to the target cortical area determine which neuronal populations are stimulated by TMS and how efficiently [49, 57]. Because neuronal cells seem to be most susceptible to electric currents flowing in the direction from the dendrites to the axon, cortical columns in sulcal walls should be most activated when the magnetic field is oriented perpendicularly to the axis of the targeted gyrus [356]. However,

the horseshoe shape of the AG offers several possible ways to place the TMS coil, each orientation presumably prioritizing different parts of that cortical area. This is a particularly relevant notion when we consider that the AG is not a homogenous region but rather consists of several subdivisions that show distinct cytoarchitecture [214, 357], connectivity profile [211] and function [228, 358, 359]. Therefore, it can be expected that different combinations of stimulation parameters may activate the target area with variable efficiency and/or preferentially engage with different brain circuits. Moreover, stimulation parameters may also differentially influence undesired activation of peripheral nerves and muscles [141, 150].

In the present study, we aimed to describe the spatiotemporal profile of TEPs evoked by stimulation of the left AG, to assess the impact of different stimulation parameters on the recorded responses and, if possible, to identify TEP components reflecting the activity directly evoked within the AG. To this end, we applied TMS to the posterior-ventral part of the AG, an area that previously showed strong connectivity to the hippocampus and other nodes of the DMN [211, 215]. The TEPs were recorded using four different stimulation orientations and three stimulation intensities and compared across conditions using the analysis of topographic dissimilarity and the microstate analysis [282, 304]. Based on the assumption that two different topographies represent the activity of two distinct sets of cortical generators [266], these two methods allow making inferences about changes in underlying TEP sources without estimating their exact location. Finally, we explored the association between the magnitude of TMS-evoked contraction of head muscles and some of the prominent features of AG TEPs identified by the topographic analysis.

5.3. Materials and Methods

5.3.1. Ethical approval

The protocol and all applied experimental procedures were approved by the Ethical Committee of Catholic University of Louvain and University Clinics Saint-Luc. All performed experiments were conducted according to the latest version of the Declaration of Helsinki.

5.3.2. Participants

19 healthy volunteers participated in the study (9 males, mean age ± SD: 23.78 ± 3.34 years). Before enrolling, candidates filled a questionnaire to control for contraindication to experimental procedures [274]. Accepted subjects gave a written informed consent and were financially compensated for their participation. All performed procedures were conducted according to the Declaration of Helsinki and approved by the Ethical Committee of Catholic University of Louvain and University Clinics Saint-Luc.

5.3.3. Experimental design

TEPs were recorded from the AG using different stimulation orientations defined by the position of the TMS coil - across or along the STS – and the direction of the electric current in the TMS coil - normal or reversed phases (Fig. 5.1C). For each of the resulting four combinations, we tested three stimulation intensities based on the individual rMT – 100, 120 or 140% rMT. The experiments were conducted in two sessions (approximately 3.5 h) separated by one week, each testing one coil position (Fig. 5.1D).

5.3.4. EEG recording

The EEG was recorded with the NeurOne EEG system (Bittium NeurOne Tesla; Bittium Corporation, Oulu, Finland) using a 32 channel EEG cap mounted with TMS-compatible Ag/AgCl electrodes (EasyCap GmbH, Herrsching, Germany) (Fig. 5.1B). The signal was referenced to FCz and recorded at 20 kHz sampling rate with 5000 Hz low-pass filter and DC filter, with electrode impedances kept below 5kΩ. Subjects were seated in a comfortable chair and fixing their gaze to a stable point. A layer of thin plastic and another textile cap were placed over the EEG cap to minimize EEG artifacts caused by the contact of electrodes with the TMS coil and subjects were listening to a custom masking noise [151] to minimize auditory artifacts.

5.3.5. TMS stimulation and neuronavigation

A 3D T1-weighted structural MRI of the head was acquired in advance (1×1×1 mm; 3 T Achieva; Philips Healthcare, Amsterdam, The Netherlands) and 3D models of the brain surface and the scalp were reconstructed in the Visor2 neuronavigation system (Visor 2.3.3; Advanced Neuro Technologies, Enschede, The Netherlands). The posterior-ventral AG was located on the brain model dorsally to the ascending branch of the STS (Fig. 5.1A), its position was projected on the scalp model and two TMS coil targets were created, one with the axis along the STS and the other perpendicular to it. The model was co-registered with subject's head using landmarks (nasion and tragi) and head-shape matching [275]. The position of the head and the TMS coil was monitored with a Polaris optical tracking system (Polaris Spectra; Northern Digital Inc. Europe, Radolfzell, Germany) and the neuronavigation ensured the accurate coil placement throughout the stimulation.

Biphasic TMS pulses were delivered manually using a MagPro stimulator (MagPro X100 with MagOption; MagVenture, Farum, Denmark) with a figure-of-eight coil (75 mm; MagVenture, Farum, Denmark) placed tangentially to the scalp and aligned with the target. The intensity of stimulation was determined based on the rMT, which was identified as the minimal intensity eliciting a motor response with an amplitude ≥ 50 μV in at least 5/10 trials [49]. The average (±SD) rMT corresponded to 44.3 ± 8.5% of the maximum stimulator output. Each experimental session contained 8 blocks of 75 TMS

pulses (jittered interstimulus interval 4-6 s) that were randomly assigned one of the tested stimulation intensities (Fig. 5.1D), delivering 100 stimuli in total for every condition.

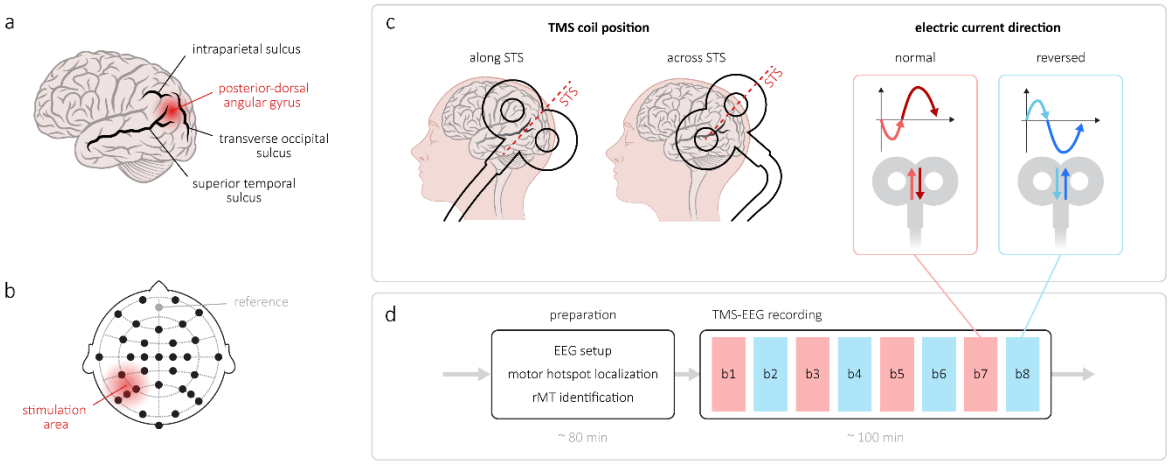

Figure 5.1 Experimental design. (A) The target site was located in the posterior-dorsal AG on the gyral crown defined relative to the position of the most prominent sulci marked in the figure. **(B)** EEG layout used in the study comprised 32 active electrodes (black), the reference is shown in grey, the red shading approximates the area under the TMS coil. **(C)** Four tested stimulation orientations were defined as the combination of two different TMS coil placements – along and across the axis of the superior temporal sulcus (STS; marked in red) and two directions of the electric current in the coil – normal (prominent second phase in dark red) and reversed (prominent phase in dark blue). **(D)** One experimental session contained 8 blocks of TMS-EEG (each approximately 6.5 mins long) with the coil placement constant but the current in the coil alternating between the blocks.

5.3.6. Data pre-processing

EEG recordings were pre-processed offline using Matlab (MathWorks, Inc., Natick, Massachusetts, United States), Letswave 6 (an open-source EEG/EMG signal processing toolbox, https://www.letswave.org/) and custom scripts following the pipeline introduced by Rogasch [139].

The signal was re-referenced to the common average, epoched (-1000 to 2000 ms relative TMS), and the DC shift and linear trend were removed. The large muscle artifact was replaced by cubic interpolation (-5 to +10 ms) and the signal was downsampled to 2 kHz. A first round of Independent Component Analysis (ICA, FastICA algorithm [277]) was performed to remove components containing the sharp leftover tail of the muscle artifact. Data were bandpass filtered (0.1-80 Hz, Butterworth, 4^{th} order) and notch filtered (50 Hz, FFT linear filter, width 2 Hz, slope 2 Hz). All epochs were visually inspected to discard those containing excessive noise, the average final number of epochs per condition was 83.7 ± 7.9.

A second round of ICA was used to remove remaining artifacts, such as eye movements, tonic muscle activity and electrode noise, as well as the remains of the muscular artifact. Suspicious components were identified with the Multiple Artifact Rejection Algorithm (MARA) [278] and

evaluated visually based on their topography, time course and frequency content. For detailed information on this step, please consult the supplementary material of [360].

Finally, the TEPs were baseline corrected (-200 to -5 ms) and group averaged.

5.3.7. Data analysis and statistics

AG TEPs were evaluated between 10 and 300 ms post stimulus. The peaks within this window were identified in the group average waveforms separately for each stimulation orientation (intensities pooled) and labelled according to their prominent polarity (P = positive, N= negative) and approximate peak latency (ms). Latencies were extracted from local maxima of the Global Field Power (GFP; Equation 1) [272].

Topographic analysis was performed in Ragu (Matlab toolbox for randomization-based analysis of EEG event-related potentials [279]) and using custom Matlab scripts. First, outliers were identified based on the Mahalanobis distance between subjects [281] and excluded. The subsequent steps followed the pipeline indicated in [280], always using 5000 permutations for the randomization and the level of significance set to 0.05. Here, we provide a brief outline of the process and invite the reader to see [361] for a detailed description. Because topographic analysis operates with normalized data, it disregards potential differences in TEP amplitude. Therefore, we additionally evaluated the influence of stimulation parameters on the magnitude of AG TEP components. These results are reported in the Supplementary materials.

Planned comparisons. The effect of two factors on AG TEPs as well as their interaction were evaluated: (1) *TMS orientation*, with four levels corresponding to different combinations of TMS coil position and electric current direction (*along-normal*, *along-reversed*, *across-normal*, and *across-reversed*); (2) *TMS intensity,* with three levels (100, 120, and 140% rMT). All comparisons were made while considering the spatiotemporal features of TEPs (analysis of topographic dissimilarity and microstate analysis) as well their magnitude (analysis of GFP amplitude).

Test for topographic consistency. TCT was conducted separately for each tested condition to identify time intervals showing significant topographic homogeneity across individuals. The GFP of the group average TEP was used as a quantifier and tested against an empirically obtained distribution computed from signals spatially scrambled at subject level.

Analysis of topographic similarity. TEP topographies were compared using the measure of Global Dissimilarity introduced by [272]. For each planned comparison, DISS was calculated based on group average TEPs (normalized at subject level by GFP) and a point-by-point statistical randomization test (TANOVA) was conducted to determine the time intervals of significant difference. The clusters of significant p values were corrected for multiple comparisons by applying a Ragu procedure called “Global Duration Statistics”, which determines the minimum necessary number of consecutive

significant time points based on the data obtained by randomization. For each factor, we calculated the momentary percentage of total explained variance (%EV), which allowed us to identify temporal maxima of topographic dissimilarity. Mean TEP topographies were extracted at these latencies and post-hoc comparisons were performed using channel-wise paired t-tests. Obtained t values were plotted as t-maps to describe the distribution and magnitude of topographic differences. The significance level was Bonferroni corrected, only significant comparisons were reported.

Microstate analysis. Microstate analysis was used to evaluate temporal properties of observed topographic differences. First, the optimal number *n* of microstate classes was determined using the cross-validation method [282]. In the next step, *n* microstate classes were identified using the k-means clustering algorithm [271] with 250 restarts. Each timepoint within each group average TEP was then labelled with the class map that yielded the highest spatial correlation with the momentary topography, thereby segmenting the waveform into intervals of dominance of one of the *n* microstate

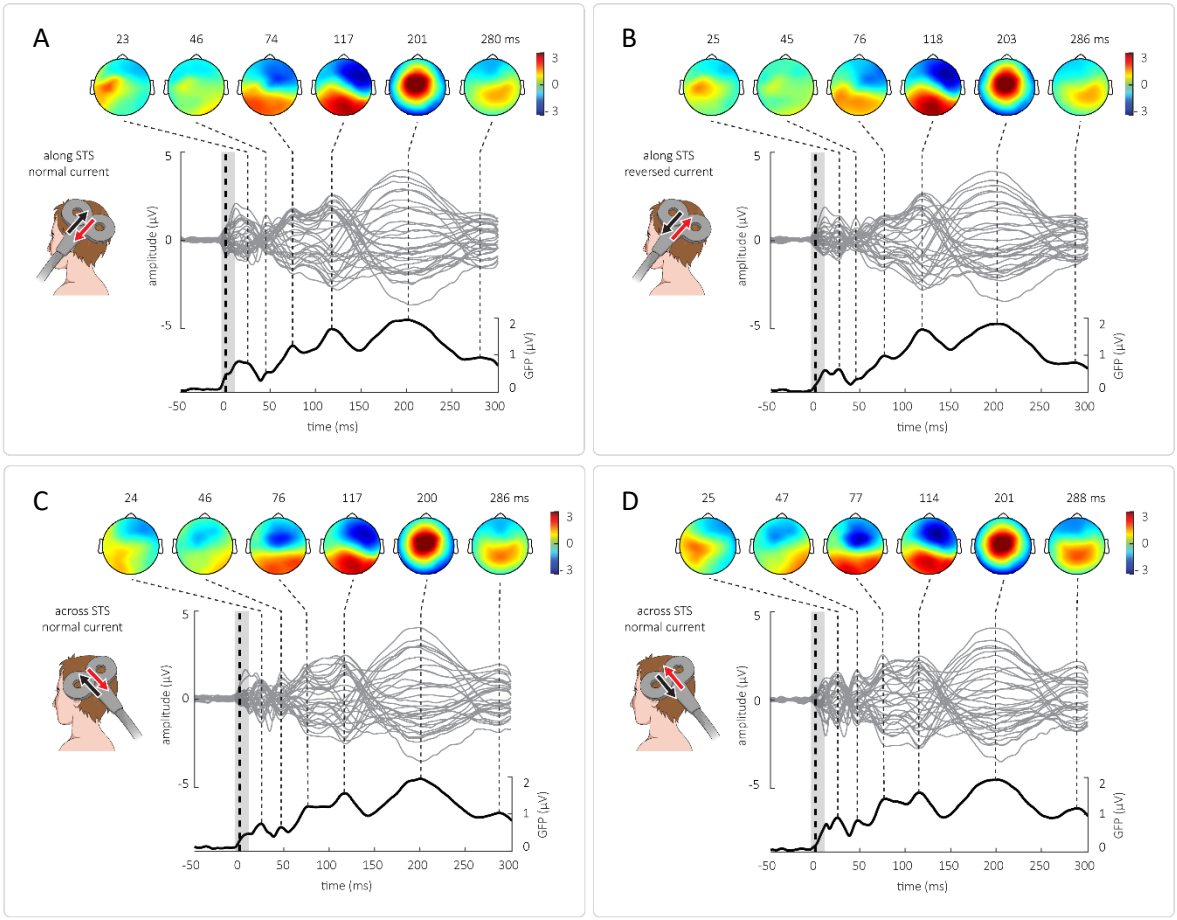

Figure 5.2 Spatiotemporal profile of AG TEPs obtained with the TMS coil placed along (A, B) or across (C, D) STS and the current flowing in the normal (A, C) or reversed (B, D) direction. For the purposes of visualization, TEPs evoked by all three intensities were averaged. The current direction in the coil is marked by a black (phase 1) and a red (phase 2) arrow. Grey lines in the middle section represent the signal of all recorded EEG channels, the TMS stimulus is denoted by a thick dashed line and the interpolated interval is shaded in light grey. The GFP of the average signal is plotted at the bottom and identified TEP components are marked by dotted lines that are associated with peak topographies displayed in the upper section; peak latencies in ms post stimulus are noted above.

classes. We then compared temporal properties (*onset*, *offset*, and *mean duration*) of each class across datasets. For each comparison and microstate, we quantified the observed effect by computing its variance across levels and tested it against an empirically obtained distribution of values true under the null hypothesis.

5.4. Results

In the text, we will refer to TEP datasets by the combination of stimulation parameters used: *orientation (along/across) – current (normal/reversed) – intensity (100/120/140)*.

5.4.1. Spatiotemporal characteristics of AG TEPs

One individual was identified as outlier and excluded (final n = 18) and remaining datasets were tested for topographic consistency, which was confirmed for the whole duration of the analyzed time window (10 – 300 ms post stimulus) with the exception of five short intervals: 34 – 51 ms in *along-reversed-120*, 12 – 19 and 32.5 – 39 ms in *along-reversed-140*, 50.5 – 61 ms in *across-normal-100* and 10 – 14.5 ms in *across-normal-140*. These epochs were not removed from subsequent analysis but were considered when interpreting the results.

AG TEPs of all conditions comprised six components that were distinguishable already at the individual subject level. To describe their general properties, data from the three stimulation intensities were pooled together for each stimulation orientation (Fig. 5.2). Peak latencies of these components as identified in the group average GFP were similar across all four datasets, whereas their associated topographies visibly differed in the three earlier peaks (Fig. 5.2, upper rows). For future reference, AG TEP components were labelled consistently in all conditions: P25, N45, N75, N100, P200 and P280.

5.4.2. Topographic dissimilarity

Effect of stimulation orientation. TANOVA identified two intervals of significant dissimilarity: 10-59 ms and 66-106 ms. Within these intervals, local maxima of total explained variance (%EV) were found at 22, 43 and 81 ms post stimulus (Fig. 5.3A). These latencies, corresponding to AG TEP components P25, N45 and N75, were then used to extract mean topographies for all compared datasets (Fig. 5.3B). Six post-hoc paired t-tests were performed at all three latencies but only comparisons at 43 and 81 ms were found significant. In both cases, a significant difference was observed between conditions of opposite coil position (*along – across,* t-maps shown in Fig. 5.3C), while no significance was found for the effect of current direction. At 43 ms (N45), the t-maps of all *along – across* t-tests showed very similar patterns, with a positivity centro-anterior on the stimulated hemisphere. The t-value distribution was less uniform at 81 ms (N75) but still featured in all four cases

a centro-frontal ipsilateral positivity. The locations of t-map maxima and minima and the associated t-values are summarized in Table 5.1.

Effect of stimulation intensity. TANOVA identified three intervals during which the topography significantly changed with the increasing stimulation intensity: 38-70 ms, 74.5-118 ms and 224-300 ms. Local maxima of %EV were found at 47, 92 and 258 ms, corresponding to AG TEPs components N45, N75 and P280 (Fig. 5.3D,E). At each %EV peak latency, post-hoc t-tests were performed to compare datasets evoked by two neighbouring stimulation intensities. At 47 ms (N45), the topography changed significantly between 100 and 120% rMT as well as between 120 and 140% rMT and both associated t-maps had a similar distribution pattern with the minimum localized frontally at the stimulated hemisphere and the maximum posteriorly at the opposite hemisphere. In addition, the topography was found significantly different when comparing datasets evoked by 120 and 140% rMT at 258 ms (P280), with the corresponding t-map showing an increase in positive values posterio-centrally (Fig. 5.3F, Table 5.1).

Interaction of stimulation orientation and intensity. One interval at 71.5-96 ms was retained by TANOVA as significant, with a local %EV maximum at 80 ms corresponding to the component N75 (Fig. 5.3G,H). Six post-hoc t-tests were used to compare all datasets at 100% rMT and at 140% rMT. While neither of the comparisons at 100% rMT proved significant, highly significant differences were found at 140% rMT when topographies with opposite coil position (*along* - *across*) were compared. All t-maps showed similar patterns, with positivity at the stimulated hemisphere (Fig. 5.3I, Table 5.1).

comparison		%EV peak latency (ms)	t maximum		t minimum		significance
			value	channel	value	channel	
TMS orientation							
current direction	*along-normal*	43	7.55	O2	-9.92	F3	n.s.
	– along-reversed	81	5.00	C2	-6.98	Fz	n.s.
	across-normal	43	7.20	F3	-5.26	P8	n.s.
	– across-reversed	81	10.62	FP2	-11.39	C3	n.s.
coil orientation	*along-normal*	43	23.22	C1	-9.56	F7	p < 0.01
	– across-normal	81	19.35	C3	-16.31	T8	p < 0.01
	along-normal	43	21.14	C3	-16.17	P8	p < 0.001
	– across-reversed	81	11.07	FC1	-13.81	CP6	n.s.
	along-reversed	43	22.55	C1	-11.07	CP6	p < 0.01
	– across-normal	81	22.24	C3	-15.02	T8	p < 0.001
	along-reversed	43	24.72	FC1	-18.74	P4	p < 0.001
	– across-reversed	81	15.69	FC1	-11.50	FC6	n.s.
TMS intensity							
120 – 100% rMT		47	11.3	O1	-22.56	FC1	p < 0.001
		258	16.48	CP2	-15.14	P7	n.s.
140 – 120% rMT		47	11.93	CP6	-16.13	FC1	p < 0.01
		258	18.49	Pz	-26.01	F8	p < 0.001
Interaction: comparison at 140% rMT							
current direction	*along-normal – along-reversed*	80	5.64	F8	-4.60	Fz	n.s.
	across-normal – across-reversed		6.96	FP2	-7.93	F4	n.s.
coil orientation	*along-normal – across-normal*		22.35	C1	-21.65	FC6	p < 0.001
	along-normal – across-reversed		19.50	CP1	-25.17	FC6	p < 0.001
	along-reversed – across-normal		22.39	C1	-19.30	CP6	p < 0.001
	along-reversed – across-reversed		-17.37	C3	-20.38	FC6	p < 0.01

Table 5.1 Post-hoc evaluation of topographic dissimilarity

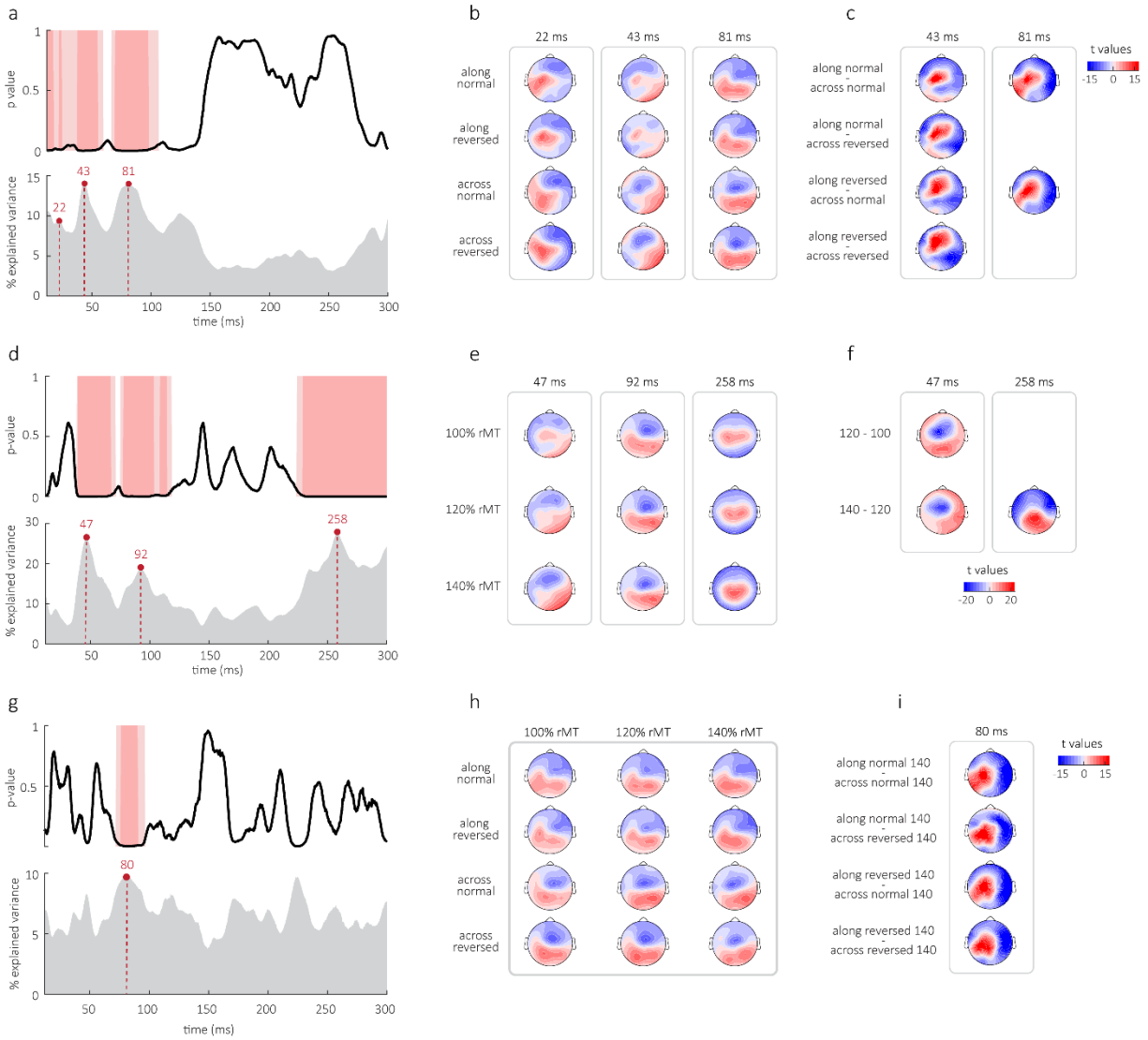

Figure 5.3 Analysis of topographic dissimilarity for different stimulation orientation (A, B, C), intensity (D, E, F) and the interaction of both factors (G, H, I). (A, D, G) Upper plots show p-values obtained by TANOVA in the analyzed time window (10 – 300 ms). Areas shaded in light pink correspond to intervals of $p < 0.05$, dark pink areas to intervals of $p < 0.01$. Bottom plots show percentage of explained variance attributed to given factor at each timepoint, peak latencies are marked by red dotted lines. (B, E, H) Mean topographies normalized to GFP that are associated to peak %EV latencies. (C, F, I) T-maps show the distribution of t-values obtained in post-hoc comparisons. Only the significant comparisons are shown.

5.4.3. Microstate analysis

The model (92.3% explained total variance) yielded six microstate classes (Fig. 5.4A) and attributed a prominent topography to each TEP component (Fig. 5.4B). Intervals of low TEP amplitude, particularly around 50 ms, were associated with rapidly switching short-lasting microstates, suggesting moments of topographic instability or transition (Fig. 5.4B,C). Analysis of temporal features was performed for all microstate classes, significant results were obtained for classes 2, 3 and 4.

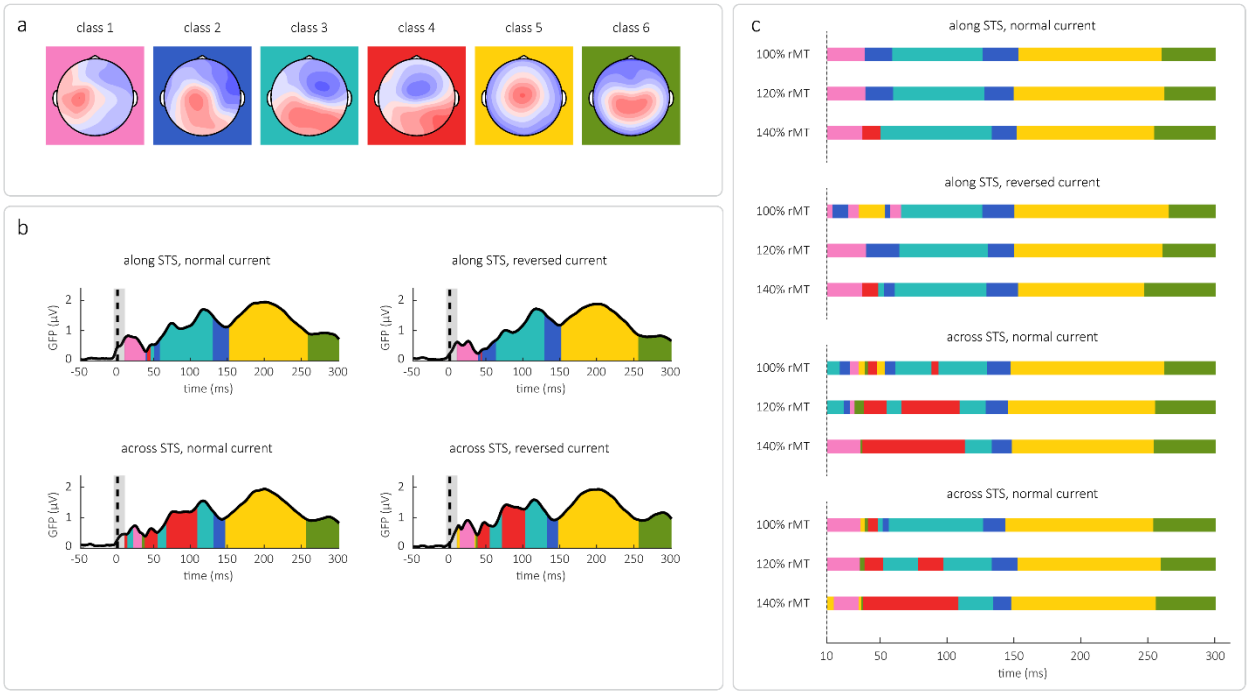

Figure 5.4 Microstate analysis. (A) 6 microstate class maps generated by the model with assigned colours. **(B)** GFP plots of TEPs averaged across tested intensities for each stimulation orientation are split into intervals corresponding to microstate classes to illustrate how microstates correspond to TEP components. **(C)** Microstate sequences of TEPs of all conditions; timepoints labelled with different microstate classes are colour-coded according to panel A.

Microstate class 2 appeared at the falling slope of component N100 and in most *along* datasets and in *across-100* datasets, it also appeared at the rising slope of N75. This was reflected in statistically significant effect of both orientation ($p < 0.001$) and intensity ($p < 0.001$) on its overall duration. We observed that class 2 lasted longer in *along-normal* and *along-reversed* datasets (on average 23 and 45 ms) than in *across-normal* and *across-reversed* datasets (15 and 16 ms). Its duration was reduced with increasing stimulation intensity (100% rMT – 40 ms; 120% rMT – 18.5 ms; 140% rMT – 17.5 ms) and this trend was more pronounced in *across* datasets (borderline significant).

Microstate class 3 represented the peak topography of both N75 and N100 in all datasets except for *across-normal-140* and *across-reversed-140*, where it was replaced at N75 latency by microstate class 4. While the occurrence of class 3 in *along* datasets changed only slightly with stimulation intensity, we saw its progressive suppression in *across* datasets as the intensity increased. This corresponds to the significant effect of orientation-intensity interaction on class 3 onset. Mean onset (ms) for 100 / 120 / 140% rMT: *along-normal* – 59.5 / 60 / 51; *along-reversed* – 66 / 65 / 49; *across-normal* – 62 / 55 / 114; *across-reversed* – 49 / 53 / 109.

The most pronounced differences between tested conditions were observed in temporal characteristics of microstate class 4. While it was missing in most *along* datasets, only appearing in a short interval in *along-normal-140* and *along-reversed-140* at latencies corresponding to N45, it was detectable in all *across* datasets where it also gained with the increasing stimulation intensity over the

class 3 at the latency of N75. This is reflected in the significant effect of stimulation orientation and intensity, as well as their interaction, on the overall duration of class 4. Mean duration (ms) for 100 / 120 / 140% rMT: *along-normal* – 0 / 0 / 13; *along-reversed* – 0 / 0 / 12; *across-normal* – 12 / 61 / 77; *across-reversed* – 8 / 33 / 71. In addition, we found a significant effect of stimulation orientation on the class 4 offset. Mean offset (ms): *along-normal* – 46; *along-reversed* – 44; *across-normal* – 109; *across-reversed* – 103.

5.4.4. Contribution of muscular contraction

During the study, a suspicion was raised that topographic differences observed between *along* and *across* AG TEPs may be related to the characteristics of face muscle contractions directly evoked by TMS rather than differential activation of target brain networks. Therefore, an exploratory analysis was carried out to evaluate the contribution of this muscular artifact. A high-amplitude evoked potential peaking within 10 ms post stimulus and showing typical peripheral distribution (Fig. 5.5A) was recovered from untreated EEG data (TMS artifact was removed between -2 and 3 ms) and attributed to the muscular contraction. Its magnitude was quantified at the subject level as the average GFP_{muscle} at 3-10 ms post stimulus (only electrodes from the stimulated hemisphere were included; Fig. 5.5B). At this point, two additional subjects were identified as outliers based on their GFP_{muscle} values and removed (final $n_{muscle} = 16$). Group visualization revealed that *across* datasets were associated with a larger muscular artifact that showed a steeper increase with stimulation intensity as compared to *along* datasets, while the influence of current direction apparently less important (Fig. 5.5C). Mean GFP_{muscle} values are summarized in Table 5.2.

Microstate analysis indicated that the most remarkable difference between *along* and *across* datasets was the occurrence of the topographic pattern attributed to the microstate class 4 at the N45 latency. To investigate the association of the muscular artifact magnitude and this specific topography, all data were grouped by coil position, sorted, and split into four categories of increasing GFP_{muscle} (Fig. 5.5D, upper panels). TEP topographies was extracted at 45 ms from processed datasets averaged within each category. We observed that in both *along* and *across* datasets, larger muscular artifacts were associated with more prominent class 4 topography (Fig. 5.5D, lower panels). Its appearance was less pronounced in *along* datasets, which corresponded to a comparatively weaker average muscular artifact.

dataset		average GFP_{muscle} (µV ± SEM)	dataset		average GFP_{muscle} (µV ± SEM)
orientation	intensity (%rMT)		orientation	intensity (%rMT)	
along normal	100	21.46 ± 7.62	across normal	100	42.27 ± 14.48
	120	37.55 ± 12.52		120	62.01 ± 15.37
	140	59.18 ± 18.52		140	100.45 ± 19.30
along reversed	100	22.28 ± 8.70	across reversed	100	47.29 ± 15.43
	120	25.62 ± 6.98		120	72.44 ± 19.78
	140	38.76 ± 11.25		140	117.24 ± 28.23

Table 5.2 Magnitude of TMS-evoked muscular contraction.

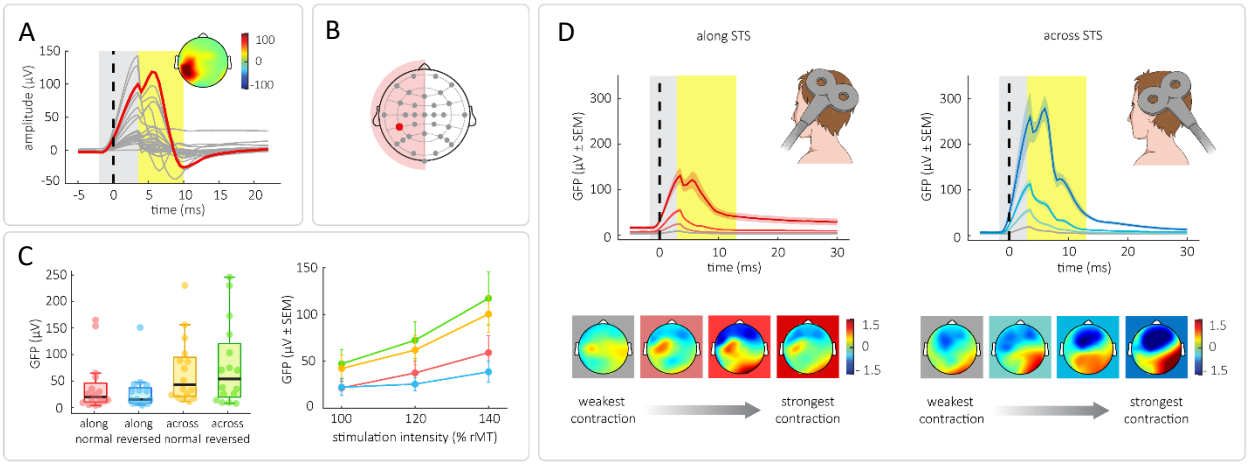

Figure 5.5 Quantification of evoked muscular contraction. (A) Average signal from all datasets showing the time-course and topography of the artifact attributed to muscular contraction; grey lines represent the signal of all electrodes, CP5 is highlighted in red. The time interval of TMS artifact interpolation is shaded in light grey, yellow area represents the time of interest over which the GFP_{muscle} was calculated. The topography was extracted at the latency of the CP5 peak (5 ms post stimulus). **(B)** EEG layout used in the study with the CP5 electrode highlighted in red marking the approximate site of stimulation. Only the signal from channels at the left (stimulated) hemisphere were used to calculate mean GFP_{muscle} used to quantify the strength of muscular twitch. **(C)** Mean group values of GFP_{muscle}; red – along-normal, blue – along-reversed, yellow – across-normal, green – across-reversed. Left panel shows individual data with all intensities averaged; black bars mark median values, box whiskers connect lower and upper quartiles to nonoutlier maxima and minima. Right panel shows group average values (± SEM) for all datasets. **(D)** Increasing muscular artifact in along (red, upper panel) and across (blue, upper panel) datasets with the corresponding topography at 45 ms (lower panels). The interval of TMS artifact interpolation is shaded in light grey, yellow area represents the time of interest over which the GFP_{muscle} was calculated.

5.5. Discussion

In the present work, we characterized the spatiotemporal profile of AG TEPs and showed that its topographic features depend on TMS coil orientation and stimulation intensity. Specifically, when investigating the effect of coil orientation, we found topographic dissimilarity across tested conditions at latencies corresponding to components P25, N45 and N75, indicating that different cortical sources were active or that the same sources contributed differently to the global activity. However, it appears that this variability cannot be solely attributed to differences in activity of the stimulated area.

One major concern when interpreting TEPs is the inevitable contamination by peripherally evoked sensory potentials [150, 185]. The magnetic field and coil vibration activate a range of receptors in the

soft tissues of the head, thereby triggering SEPs, while the clicking sound of TMS produces AEPs. By comparing active TMS with sham stimulation, multiple studies showed that PEP contribution to TEPs increases with time and must be considered as soon as 50-60 ms post stimulus [158, 159, 184, 185, 362, 363]. Therefore, P25 and N45 should be the most relevant components of AG TEPs to probe the functional status of the AG.

Several arguments indicate that P25 is likely to reflect activity due to direct cortical activation of the AG network. We previously compared TEPs evoked from the primary motor cortex and the AG (coil placed across STS) and found that the P25 topography is highly target specific [361]. Here, we observed significant topographic dissimilarity of P25 of AG TEPs evoked by different stimulation orientation, yet the patterns were similar enough to be pooled into a single microstate. This subtle variability could be explained by differential engagement of local neuronal sub-populations depending on their sensitivity to different features of the induced electric field. Moreover, another recent study succeeded to locate P25 cortical generators in the stimulated AG as well as the ipsilateral ventral medial prefrontal cortex [235], an area also belonging to the DMN [364]. Therefore, P25 of AG TEPs likely represents a valuable non-invasive biomarker of the functional state of the AG network.

By contrast, our data suggest that the later component N45 might be prone to contamination by somatosensory-evoked input triggered the TMS-evoked twitch of head muscles. When the TMS coil is placed over a head muscle, the stimulation triggers a muscular contraction [365] which, in turn, activates mechano-sensitive somatosensory afferents. Because coil placement determines the character of muscle activation, distinct coil orientations are likely associated with differences in the strength of muscular activation and somatosensory feedback, leading to variable degrees of TEP contamination by somatosensory-evoked cortical activity. Such difference might be especially pronounced when stimulating targets with lateral projection on the scalp, such as the AG. Indeed, we observed that the muscular contraction was stronger when TMS stimulation was delivered *across* as compared to *along* the STS and augmented with increasing stimulation intensity. Most importantly, the effects of TMS coil orientation and stimulation intensity on the N45 topography followed the effects on TMS-evoked muscular activity.

Furthermore, the microstate analysis revealed that N45 elicited by AG stimulation *across* the STS was dominated by a bipolar topographic pattern (microstate class 4) centred over the contralateral hemisphere, whose occurrence and duration increased with stimulation intensity. This topography bears a striking resemblance to that of mid-latency SEPs evoked by electrical stimulation of mixed peripheral nerves of the face accompanied by a muscle twitch [287, 366, 367]. Independently of coil position, this pattern became more pronounced as the magnitude of the muscular artifact increased. Moreover, considering the influence of individual anatomy on muscular contractions, variable occurrence of muscular activation could explain the inter-subject topographic inconsistency of the N45

component, previously also described for motor cortex TEPs [361]. Therefore, TEP changes at the latency of N45 should be interpreted with caution, especially when simultaneous changes in evoked muscular activity occur.

5.6. Conclusion

In summary, we show that topographic features of early AG TEPs are dependent on TMS stimulation parameters, thus reflecting differential engagement of underlying brain sources. We conclude that the earliest component P25 of AG TEPs likely corresponds to brain activity evoked by direct activation of the AG and as such could serve as a biomarker of excitability within the AG and the connected DMN. In contrast, the subsequent component N45 seems to be influenced by the presence of TMS-evoked peripheral muscle activity and should be interpreted with caution. While all tested TMS coil positions efficiently activate the AG, placing the coil along STS minimizes muscular contractions and should be preferred when recording AG TEPs.

5.7. Supplementary materials: Influence of stimulation parameters on AG TEP magnitude

5.7.1. Material and methods

The analysis of topography provides valuable information about the qualitative changes in the EEG signal, but since it operates with normalized data, it disregards the quantitative changes in the EEG amplitude. For this reason, we also performed all planned comparisons considering the magnitude of AG TEPs, which was expressed as GFP and evaluated using a point-by-point randomization-based test implemented in Ragu. 5000 permutations were run to obtain an empirical distribution of values true under the null hypothesis and p value was extracted as a function of time. The clusters of significant timepoints were retained only when surviving the 'Global Duration Statistics' correction.

5.7.2. Results

While we did not see any effect of stimulation orientation on the GFP, the effect of stimulation intensity was expectedly found significant over the whole considered time window. When considering the interaction of both factors, an interval of significance was identified at 17 – 56.5 ms post stimulus, which includes the earliest TEP components P25 and N45 (Fig. 5S.1A). Remarkably, a sharp local maximum of %EV was localized at 42 ms post stimulus (Fig. 5S.1B) and the time interval covering N45 (30.5 – 55 ms) was characterized by very low p values ($p < 0.01$).

To further explore the effect of interaction at N45, GFP was averaged across the interval of $p < 0.01$ at the level of individual subjects and mean values were extracted for each tested condition (Fig. 5S.1C). We observed that when the stimulation intensity of 100% rMT was used, response strength was greater in *along* datasets than in *across* datasets, While the GFP values generally increased with the stimulation intensity, this increase was much steeper in *across* datasets, leading to larger GFP

values at 140% rMT in *across* than *along* datasets. The trend was further accentuated when visualized as the GFP change with increasing intensity (Fig. 5S.1D).

Average values (µV ± SEM) obtained for each condition (100 / 120 / 140% rMT): *along-normal* – 1.14 ± 0.11 / 1.26 ± 0.11 / 1.47 ± 0.14; *along-reversed* – 1.08 ± 0.08 / 1.27 ± 0.12 / 1.32 ± 0.10; *across-normal* – 0.94 ± 0.06 / 1.26 ± 0.11 / 2.03 ± 0.22; *across-reversed* – 0.99 ± 0.06 / 1.41 ± 0.12 / 1.98 ± 0.19.

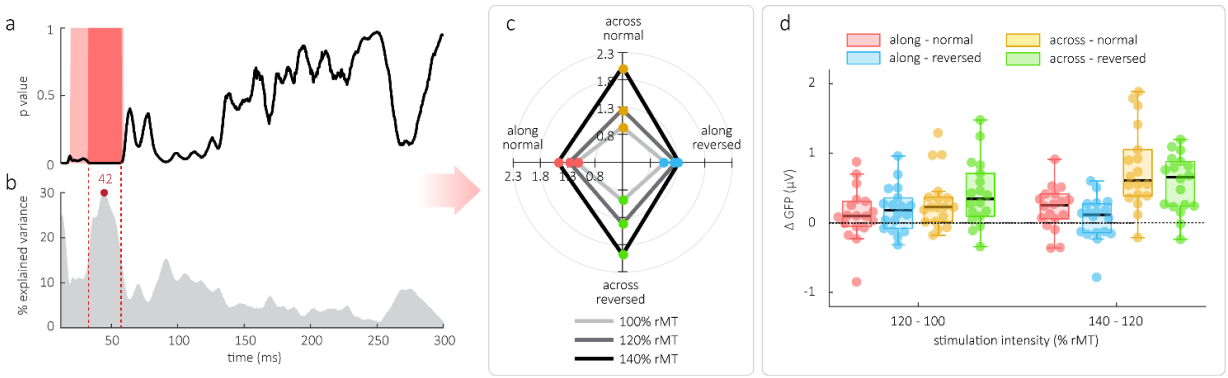

Figure 5S.1 Analysis of TEP amplitude. (A) P-values obtained by permutation-based ANOVA across the whole analysed time window (10 – 300 ms) for the interaction between factors stimulation orientation and stimulation intensity. Area shaded in light pink corresponds to the interval of $p < 0.05$, dark pink area to the interval of $p < 0.01$. **(B)** Percentage of explained variance attributed to each timepoint. Red dotted lines indicate the time interval that was used to extract the mean GFP; the peak latency is denoted by a red dot. **(C)** Radar plot showing the mean GFP averaged across the interval of interest in all compared conditions. The axes represent levels of stimulation orientation; levels of stimulation intensity are marked by full lines (see legend). **(D)** The change in mean GFP with the increasing stimulation intensity. The change was calculated at the individual level as a simple subtraction of the GFP at lower intensity from the GFP at the higher intensity. Levels of stimulation orientation are distinguished by colour (see legend), black bars mark median values, box whiskers connect lower and upper quartiles to nonoutlier maxima and minima.

6. Probing intracortical inhibition in the angular gyrus using TMS-EEG

6.1. Introduction

In previous chapters, we discussed the utility of TEPs for non-invasive exploration of functional properties of cortical areas and brain networks of interest, and we particularly focused on the evaluation of local $GABA_AR$-mediated inhibition. We showed that pharmacological activation of $GABA_ARs$ with BDZs has a specific effect on M1 TEPs that is correlated to the effect of TEP SICI evoked by paired-pulse stimulation, so it seems that both measures can be used to assess the state of cortical inhibition, at least when the sensorimotor network is concerned. We therefore propose that if both approaches provide similar information, it might be safer and more advantageous to focus on TEP SICI when assessing the state of local inhibition. The medication with BDZ leads to a considerable state of sedation, may not always be well tolerated, prolongates the duration of the experiment and, most importantly, influences the $GABA_ARs$ globally over the whole brain, which may represent a serious drawback when investigating a specific area/network of interest.

With this reasoning in mind, we decided to use the SICI paradigm to explore the state of $GABA_AR$-mediated inhibition within the AG, more precisely in its posterior-ventral area that belongs to the DMN. As discussed in chapter 5, we previously described in detail the spatiotemporal profile of single-pulse AG TEPs and identified the combination of stimulation parameters that minimizes the contraction of head muscles, and by consequence the interference of SEPs with the TEP signal. We applied these parameters in the present study, where we explored the effect of paired-pulse stimulation of the AG on the recorded TEPs with the aim to describe the AG TEP signature of local inhibitory activity. We chose to evaluate three different CS intensities (60, 80, and 100% rMT) in combination with a TS of 120% rMT – an intensity that previously reliably evoked a single-pulse response. In addition, we recorded single-pulse CS TEPs in order to evaluate how the CS TEP variability relates to the potential differences in the effect of AG TEP SICI.

The following chapter contains a full description of the study design and the methodology used for data acquisition, pre-processing and preliminary analysis. We then present the preliminary results, but no discussion is included and the results are only commented in the general discussion (chapter 7) of the manuscript.

6.2. Materials and Methods

6.2.1. Ethical approval

All applied procedures were approved by the Ethical Committee of Catholic University of Louvain and University Clinics Saint-Luc and the experiments were conducted according to the latest version of the Declaration of Helsinki.

6.2.2. Participants

18 healthy volunteers participated in the study (7 males, mean age ± SD: 25.2 ± 4.7 years). Before being accepted, the candidates were informed about the protocol and experimental procedures. In addition, they filled a questionnaire to control for any contraindications for magnetic resonance imaging and transcranial magnetic stimulation, such as epilepsy (or familiar history thereof), presence of a metal object in the body (e.g. insulin pump, pacemaker, metal prothesis), confirmed neurological pathology or use of medication affecting cortical excitability [274]. All participants gave a written informed consent when entering the study and were financially compensated for their participation upon its conclusion.

6.2.3. Experimental design

The participants were asked to sleep sufficiently, and to avoid alcohol in the evening and caffeinated beverages in the morning before the experiment. TMS-EEG data acquisition was done in a single experimental session that lasted approximately 3 hours and took place always in the morning. TEPs were recorded in 9 blocks, each containing 77 stimuli of all 7 conditions (11 stimuli per condition), so that each condition comprised in total 99 stimuli. Four different intensities of single pulse TMS were used – 60 (spCS1), 80 (spCS2) , 100 (spCS3) and 120 (spTS) % of subject's rMT – as well as three different combinations of paired pulse TMS (CS1-TS, CS2-TS, CS3-TS) with a constant interstimulus interval of 2.5 ms. Individual trials were delivered in a semi-random order (max. three stimuli of the same type in a row) and separated by a variable interval within the range of 4-6 s. The stimulation blocks were separated by 5 min pauses when the subjects were asked to perform a short sequence of physical exercises (squats, launches, etc.) to maintain an acceptable level of arousal.

6.2.4. EEG recording

EEG was recorded with the NeurOne EEG system (Bittium NeurOne Tesla; Bittium Corporation, Oulu, Finland) using 32 channel EEG cap mounted with TMS-compatible Ag/AgCl electrodes (EasyCap GmbH, Herrsching, Germany). As distinct from the usual layout, the mastoids were removed and channels P5/6 were added to increase recording density over the parietal cortex. The signal was referenced to an additional electrode placed at the FCz position and recorded at 20 kHz sampling rate with 5000 Hz low-pass filter and DC filter. Electrode impedances were kept below 5kΩ during the whole session. During the TEP acquisition, subjects were seated in a comfortable chair in a slightly reclined position and were instructed to keep their gaze fixed on a stable point. A thin layer of plastic and a second textile cap were placed over the EEG cap to minimize artifacts caused by a direct contact of electrodes with the TMS coil, to reduce the bone conduction of the vibration accompanying the

stimulation, and to prevent the conductive gel from drying. In addition, subjects were listening to a masking noise generated from a recording of the TMS click [151] to minimize the auditory artifacts.

6.2.5. Neuronavigation

A 3D T1-weighted structural MRI of each subject's brain was acquired in advance at the Department of radiology of the Cliniques universitaires Saint-Luc (1×1×1 mm; 3 T Achieva; Philips Healthcare, Amsterdam, The Netherlands). Based on this data, a 3D model of the brain surface and the scalp was reconstructed in the Visor2 neuronavigation system (Visor 2.3.3; Advanced Neuro Technologies, Enschede, The Netherlands) and used to localize the target. In each individual brain model, an experienced researcher identified the posterior-ventral AG lying dorsally from the ascending branch of the STS in the horseshoe curve of the gyrus. This location was projected on the scalp model and a coil target was centred over it with the axis aligned with the upper STS, as this orientation was previously identified as the most advantageous when targeting the AG [368].

At the beginning of the session, the 3D model was co-registered with subject's head using landmark markers (nasion and tragi) and head-shape matching [275]. The real-space position of the head and the TMS coil was continually monitored with the Polaris infrared optical tracking system (Polaris Spectra; Northern Digital Inc. Europe, Radolfzell, Germany), and Visor2 was used to ensure the accurate placement of the real TMS coil and its stable position throughout the stimulation.

6.2.6. TMS stimulation

Biphasic TMS pulses in reversed phase order were delivered manually using a MagPro X100 magnetic stimulator (MagPro X100 with MagOption; MagVenture, Farum, Denmark) with a figure-of-eight TMS coil (outer diameter of 75 mm; MagVenture, Farum, Denmark). The coil was placed tangentially on the scalp and aligned to the AG coil target. The intensity of TMS stimulation was determined based on subject's rMT, which was identified as the minimal stimulation intensity eliciting a motor response from the first dorsal interosseus muscle of the right hand (contralateral to the stimulated hemisphere) with the amplitude of least 50 µV in at least 5 trials out of 10 [49]. The average rMT (± SD) corresponded to 44.6 ± 7.6% of the maximum stimulator output.

6.2.7. Data pre-processing

EEG recordings were processed offline using Matlab (MathWorks, Inc., Natick, Massachusetts, United States), Letswave (an open-source EEG/EMG signal processing toolbox, https://www.letswave.org/) and custom scripts.

To clean the EEG signal, we followed the pipeline introduced by Rogasch [139]. The signal was re-referenced to the average of all electrodes, the data were cut into epochs from –1000 ms to 1000 ms relative to the TMS pulse and the DC shift and linear trend were removed. The large artifact caused by

the TMS was cut out between -5 and +10 ms and replaced using cubic interpolation, then the signal was down-sampled to the sampling rate of 2 kHz and epochs of each condition were parsed into separate datasets. The first round of ICA (FastICA algorithm [277]) was performed to remove components containing the peaky leftover of the TMS-evoked muscle. Data were then bandpass filtered between 0.1 and 80 Hz (Butterworth, 4^{th} order) and notch filtered at 50 Hz (FFT linear filter, notch width 2 Hz, slope cut-off width 2 Hz). All epochs were visually inspected and those containing excessive noise were discarded, as well as any trials when the TMS coil missed the target. On average, 84.2 ± 8.4 (SD) epochs were retained for each condition.

In the next step, the second round of ICA was used to remove remaining artifacts of a extra-cerebral origin, such as eye blinks, horizontal eye movements, tonic muscle activity and electrode noise, as well as the last remains of the artifact caused by the TMS-induced muscle twitch. Artifactual components were first identified automatically with the MARA, a classifier trained on adult EEG data [278]. These were then evaluated by an experienced researcher based on their topography, time course and power spectrum density. When selecting the components to remove, we opted for a conservative approach and retained those that could not be reliably categorized. For detailed information on the characteristics of different types of TEP artifacts that we identified, please consult the supplementary material of [360].

Finally, the TEPs were baseline corrected to the interval from 200 ms to 5 ms before the TMS pulse and averaged for each subject and condition.

6.2.8. Preliminary data analysis

Prior any analysis, the outliers were identified based on the Mahalanobis distance between subjects [281] and excluded (this step was performed using Ragu toolbox for topographic analysis of EEG event-related potentials [279]). Retained datasets were then evaluated between 10 and 300 ms post stimulus.

In single-pulse TEPs, the peaks within the analysed time window were automatically identified as local maxima in the GFP calculated from the average single-pulse waveform. The components were labelled according to their prominent polarity (P = positive, N= negative) and peak latency, consistently with existing literature. Because our previous study indicated that components peaking later than 80 ms post stimulus are highly contaminated by somatosensory and auditory evoked potentials [361] (see chapter 3), we only focused on AG TEP components occurring at earlier latencies. To assess the TEP peak features, TOIs were first estimated based on the average GFP and the amplitude and latency of each single-pulse TEP were then extracted semi-automatically from the GFP of individual subjects. To this end, the TOI span was kept constant but its onset was adjusted to reliably cover the GFP peak in each subject, which allowed us to respect the inter-individual differences in peak latency. A repeated

measures analysis of variance (rm-ANOVA) was performed to evaluate the effect of stimulus intensity on GFP peak measures (the Greenhouse–Geisser correction was applied if needed). In case of significant finding (alpha was always set to 0.5), multiple post-hoc paired t-tests (Tukey's honest significant difference) were performed to identify significant comparisons.

The effect of paired-pulse stimulation was first evaluated in datasets obtained by a subtraction of single-pulse TS TEPs (120% rMT) from each of the paired-pulse TEPs. Again, the TOIs were identified in the group average GFP, the peak magnitude and latency was extracted from the individual GFP data and obtained values were compared across conditions using rm-ANOVA and post-hoc paired t-tests. In addition, we visualized the voltage distribution of the change. For this purpose, the peak topography was normalized at the individual level by the corresponding GFP and then averaged across subjects.

In the next step, we used the Ragu software to compute AG TEP microstates (four datasets were included in the analysis: spTS TEPs + three paired-pulse TEPs) and to associate them with identified TEP components. The optimal number *n* of microstate classes was determined with cross-validation in the range from 3 to 10 using 250 restarts [282]. Each timepoint of each group average TEP was then labelled with one of the *n* classes and the grand mean was used to describe the general microstate sequence of AG TEPs (for a more detailed description of the microstate analysis, we refer the reader to the original tutorial paper [280] or to our previous publication [361]; see chapter 3). The microstate class maps labelling the early TEP peaks were used to identify 3 EOIs, their signals were pooled together and used to extract peak amplitude and latency of each evaluated component. These values were then compared between TS and all three paired-pulse conditions, and the statistics were obtained using rm-ANOVA as described before.

6.3. Preliminary results

6.3.1. Single-pulse AG TEPs

Prior any further analysis, three individuals were identified as outliers and excluded (final n = 15). Four consistent AG TEP components were identified in the GFP of all averaged single-pulse datasets: P25 (peaking at 23 ms), N75 (73 ms), N100 (116 ms), and P180 (188 ms). Because of the questionable origin of N100 and P180, only the two earlier components were further evaluated. Based on the single-pulse average GFP, TOIs were determined for P25 (15 – 40 ms post stimulus) and N75 (55 – 80 ms) and used to extract the mean peak topography. P25 was characterized by a positivity at the stimulated hemisphere that showed a variable pattern across individual single-pulse TEPs. By contrast, N75 showed a voltage distribution consistent across all single-pulse conditions with a positivity posterior on the stimulated hemisphere and a negativity anterior on the contralateral hemisphere (Fig. 6.1A).

Next, the GFP peak latency and amplitude were extracted from each TOI at the subject level. Average group values are shown in Table 6.1, amplitude values are also visualized in Fig. 6.1B. While

the rm-ANOVA did not find any significant differences for the GFP peak latency, the four single-pulse conditions differed significantly in their GFP peak amplitude: P25 – $F(3, 42) = 4.81$, $p < 0.01$; N75 – $F(3, 42) = 12.33$, $p < 0.001$. Post-hoc testing revealed that in case of P25, the effect was mainly driven by the difference spTS-spCS2 ($t = 0.35$, $p < 0.01$), whereas multiple paired t-tests came out as significant in case of N75 (all except spCS1-spCS3 and spCS2-spCS3; Fig. 6.1B).

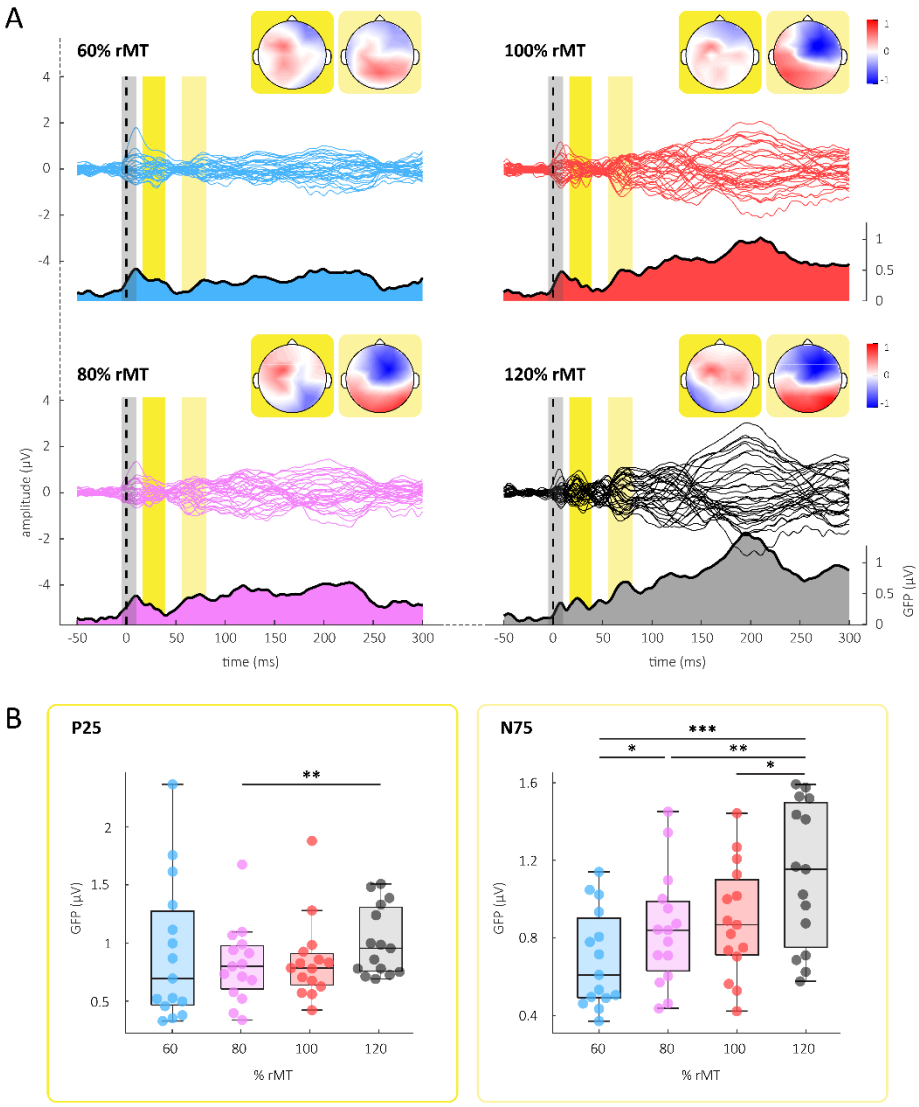

Figure 6.1 Single-pulse AG TEPs. **(A)** Spatiotemporal features of single pulse TEPs. Color-coded: blue – 60% rMT (spCS1), pink – 80% rMT (spCS2), red – 100% rMT (spCS3), black – 120% rMT (spTS). Each subplot contains a butterfly plot of the group average TEP (middle section) and the associated GFP (bottom). The TMS pulse is marked by a black dashed line, the interpolated interval is shaded in grey. Average peak topographies (normalized to GFP at subject level) of TEP components P25 (TOI shaded in dark yellow) and N75 (light yellow) are displayed in the upper section. **(B)** Peak amplitudes of P5 and N75. Group medians are marked by a horizontal line inside each box, the whiskers connect lower and upper quartiles to nonoutlier maxima and minima. The asterisks mark the significance of individual comparisons (* p< 0.5, ** p<0.01, *** p<0.001).

6.3.2. Paired-pulse AG TEPs

In the first step, we aimed to visualize at which latencies the paired-pulse protocol led to a change in the TEP profile by exploring the difference between paired-pulse TEPs and the spTS TEP. Visual inspection of these subtracted waveforms revealed that the maximum change occurred around latencies 15, 50, 100 and 180 ms post stimulus, with all peaks clearly visible in all three datasets (Fig. 6.2A, left panel). To better characterize these peaks, we computed GFP and extracted GFP peak latency and amplitude for each subject. Obtained average group values are shown in Table 6.2, amplitude values are also visualized in Fig. 6.2B. When compared across conditions, the latency of GFP peaks did not evince any significant variability, whereas the amplitude differed significantly in all but the earliest peak: 50 ms – $F(2, 28) = 5.11$, $p < 0.05$; 100 ms – $F(2, 28) = 10.13$, $p < 0.001$; 180 ms – $F(2, 28) = 8.06$, $p < 0.01$. Post hoc testing further showed that at 50 ms, the change in TEP amplitude was significantly larger when CS1-TS and CS3-TS conditions were compared ($t = 0.34$, $p < 0.05$), while in both following latencies, both comparisons with CS3-TS were found significant (100 ms: CS3-TS – CS1-TS – $t = 0.44$, $p < 0.01$; CS3-TS – CS2-TS – $t = 0.43$, $p < 0.01$; 180 ms: CS3-TS – CS1-TS – $t = 0.48$, $p < 0.05$; CS3-TS – CS2-TS – $t = 0.29$, $p < 0.05$).

stimulus	**15 ms**		**50 ms**	
	mean latency ms ± SD	**mean GFP** µV ± SD	**mean latency** ms ± SD	**mean GFP** µV ± SD
CS1-TS - spTS	14.8 ± 5.7	1.4 ± 0.8	49.2 ± 12.4	1.0 ± 0.5
CS2-TS - spTS	15.1 ± 4.4	1.3 ± 0.5	50.4 ± 11.4	1.1 ± 0.4
CS3-TS - spTS	14.8 ± 3.8	1.3 ± 0.4	52.8 ± 11.5	1.3 ± 0.5
	100 ms		**180 ms**	
	mean latency ms ± SD	**mean GFP** µV ± SD	**mean latency** ms ± SD	**mean GFP** µV ± SD
CS1-TS - spTS	99.7 ± 21.3	1.0 ± 0.4	179.5 ± 30.1	1.1 ± 0.3
CS2-TS - spTS	101.2 ± 16.6	1.0 ± 0.3	180.5 ± 32.7	1.3 ± 0.4
CS3-TS - spTS	101.8 ± 20.0	1.5 ± 0.4	174.8 ± 30.4	1.6 ± 0.6

Table 6.2: paired-pulse AG TEPs – GFP peak amplitude and latency of subtracted datasets corresponding to the maximum change elicited by the paired-pulse stimulation.

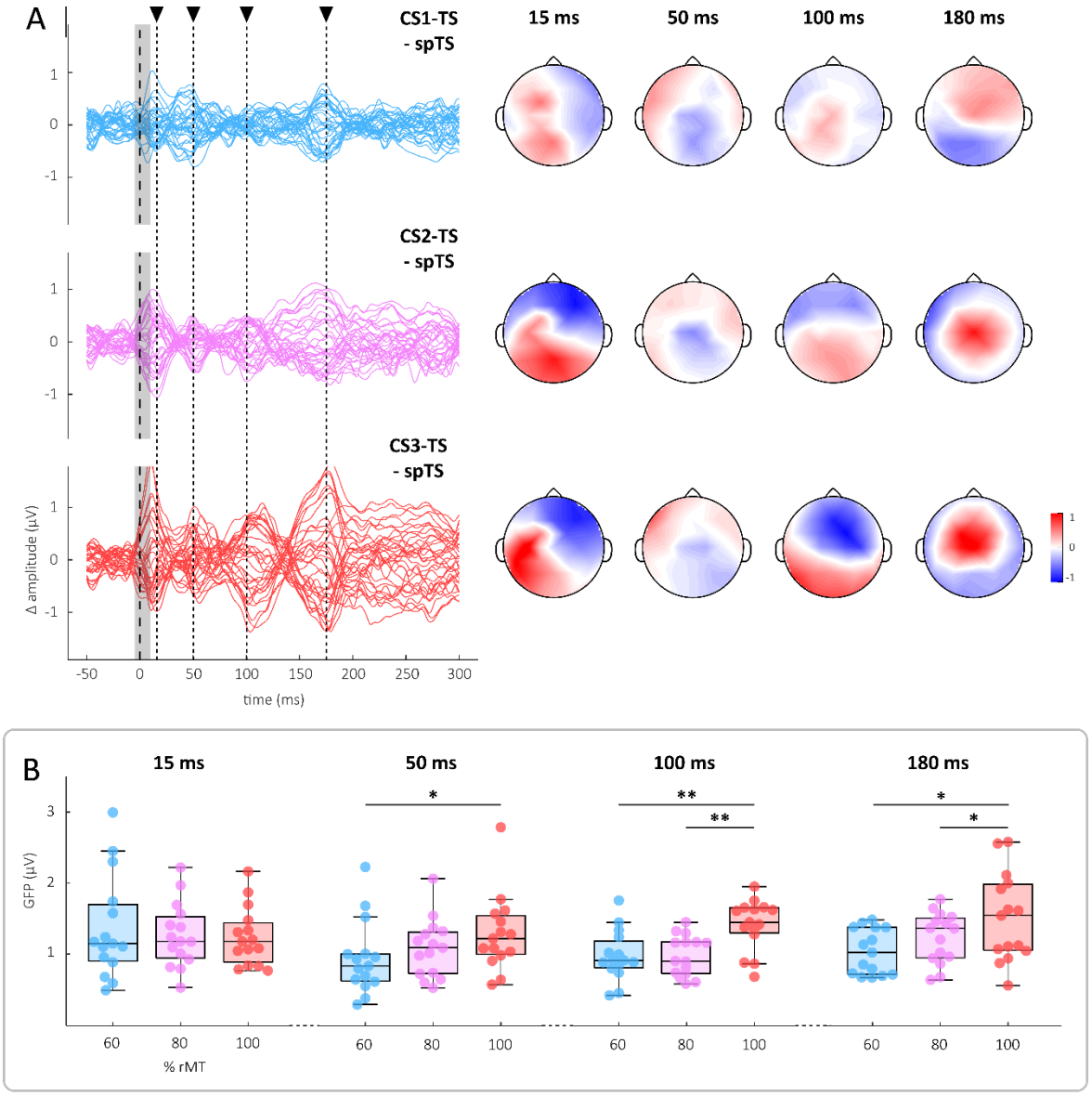

Figure 6.2 Subtraction of spTS TEPs from paired-pulse TEPs. (A) Spatiotemporal features of the paired-pulse effect. The left panel shows the time course of the difference between paired-pulse TEPs and single pulse TS TEPs. Colourcoded: blue – CS1-TS - spTS, pink – CS2-TS - spTS, red – CS3-TS – spTS. Four peaks were indentified in the signal at approximate latencies 15, 50, 100 and 180 ms post stimulus that are marked with thin vertical dashed lines. A thick dashed line denotes the TMS stimulus, the interpolated interval is shaded in grey. The topographies associated to the peak latencies are displayed in the right panel. **(B)** Quantification of the paired-pulse evoked change at individual identified GFP maxima. Colourcoded: blue – CS1-TS - spTS, pink – CS2-TS – spTS; red – CS3-TS - spTS. Significant difference between groups is marked by asterisks (* $p < 0.05$, ** $p < 0.01$).

In addition to the analysis of GFP peak altency and amplitude, we also extracted normalized topographies at individual peak latencies in order to visualized the distribution of change (Fig. 6.2A, right panel). The average topography at 15 ms showed a voltage increase over the stimulated hemisphere and bilaterally in the back, and the pattern was quite similar in all three tested conditions. At 50 ms, we observed a centro-posterior decrease in the voltage mostly pronunced over the non-stimulated hemisphere, with a pattern similar across conditions. At 100 and 180 ms, the change

distribution was similar for CS2-TS and CS3-TS conditions and resembled the mean topography of AG TEP components N100 and P180. By contrast, the topohraphy of CS1-TS change differed from the rest, at 100 ms showing a voltage increase located centro-posterior and shifted towards the stimulated hemisphere, while at 180 ms it revealed an increase in voltage frontally and decrease posteriorly.

In the next step, to further evaluated the effect of paired-pulse stimulation on early AG TEps, we characterized the spatiotemporal features of four compared datasets (spTS, CS1-TS, CS2-TS, and CS3-TS) by attributing to each condition a sequence of non-overlapping microstates. The chosen model yielded 6 different microstate classes which explained 92.4% of the global topographic variance (Fig. 6.3A). In the following steps, we again limited the analysis to early peaks P25 and N75. We expected components P25 and N75 to be labelled with a distinct microstate class, however, P25 was repeatedly split into two classes with very different topographies. We speculated that two different processes may take place at these early latencies and decided to characterize them separately as components P20, which was associated to the microstate class 1 with a large positivity at the site of stimulation, and P30, characterized by a localized fronto-central positivity at the stimulated hemisphere (class 2). The component N75 was labelled with class 3 with a typical posterior positivity peaking at the site of stimulation and frontal negativity peaking at the contralateral hemisphere.

Finally, microstate class maps attributed to each component of interest were used to identify electrodes of interest, as illustrated in Fig. 6.3B. The signal of these EOIs was then used to extract peak amplitude and latency of P20, P30 and N75 - obtained average group values are shown in Table 6.3, amplitude values are also visualized in Fig. 6.3C. Although visual inspection suggests that there may be group differences in amplitude of all three components, rm-ANOVA only returned significant statistic for the amplitude of P30 ($F(3, 42) = 3.49$, $p < 0.05$), and this result is driven by a single significant comparison between CS2-TS and CS3-TS ($t = 0.44$, $p < 0.01$).

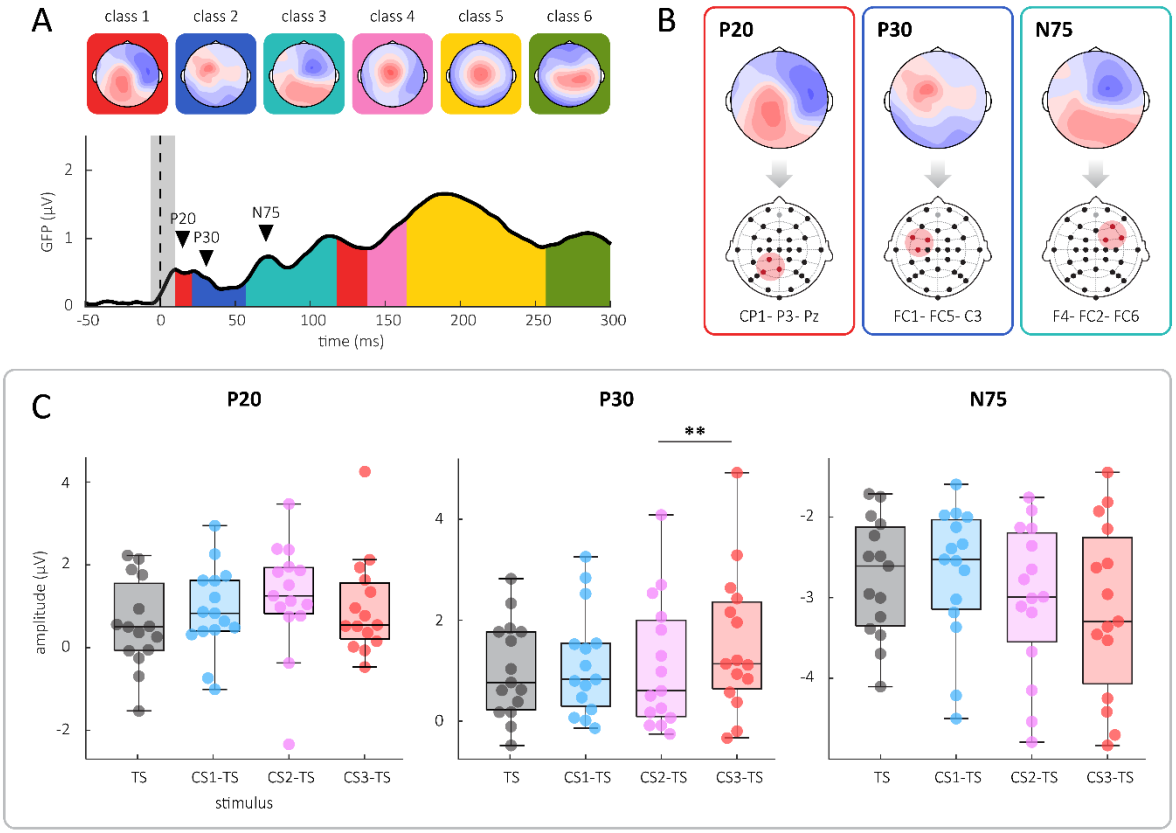

Figure 6.3 Paired-pulse effect on AG TEP amplitude. (A) The microstate sequence in the average dataset. The lower panel shows the time course of the average GFP with successive intervals labelled with different microstate classes. A dashed line denotes the TMS stimulus, the interpolated interval is shaded in grey. The topographies associated with individual microstate classes are displayed in the upper panel. **(B)** Three early microstates of interest cover TEP components P25 – split in P20 and P30 – and N75. Based on their class maps (upper row), three EOIs (lower row) were attributed to each component. (C) Peak amplitudes extracted from the EOI signal of each TEP component. Colourcoded: black – spTS, blue – CS1-TS, pink – CS2-TS, red – CS3-TS. Significant difference between groups is marked by asterisks (* $p < 0.05$).

stimulus	P20		P30	
	mean latency ms ± SD	mean amplitude µV ± SD	mean latency ms ± SD	mean amplitude µV ± SD
spTS	21.0 ± 5.7	0.6 ± 1.1	36.9 ± 16.0	1.0 ± 1.0
CS1-TS	19.4 ± 4.1	0.9 ± 1.0	36.9 ± 14.7	1.1 ± 1.0
CS2-TS	19.3 ± 4.1	1.2 ± 1.3	37.5 ± 13.8	1.1 ± 1.3
CS3-TS	19.2 ± 4.6	1.0 ± 1.2	33.8 ± 13.7	1.5 ± 1.4

	N75	
	mean latency ms ± SD	mean amplitude µV ± SD
spTS	80.0 ± 17.6	-1.7 ± 0.7
CS1-TS	83.0 ± 19.0	-1.7 ± 0.8
CS2-TS	81.3 ± 18.4	-2.0 ± 0.9
CS3-TS	81.8 ± 20.5	-2.2 ± 1.1

Table 6.3: paired-pulse AG TEPs – TEP peak amplitude and latency.

7. General discussion

7.1. Early TEPs as biomarkers of local cortical excitability

The immense potential of TMS-EEG for exploration and assessment of functional properties of the human brain is undeniable. The findings presented in this manuscript contribute to the great bulk of existing literature confirming that TEPs reflect, at least in part, neural activity evoked by the direct and selective stimulation of cerebral cortex, and as such can provide valuable information about the excitability and connectivity of the target brain network. However, the interpretation of TEPs, and by consequence their practical use as biomarkers, is considerably complicated by their contamination by various types of artifacts. While some of these are relatively easily removed, others - such as AEPs and SEPs of different sources – likely influence the TEP signal along its entire time course and it is impossible, with the currently available tools, to completely prevent or remove their contribution. Certainly, the use of efficient noise masking, realistic sham stimulation and sophisticated data processing can greatly improve TEP quality (and is highly recommended), but all these methods come with key limitations that are still waiting to be resolved. Until that happens, we must accept the inevitably heterogenous origin of TEPs and carefully estimate the significance of any changes in TEP features induced by experimental manipulations.

Yet, it is possible that the impact of peripherally evoked sensory potentials (PEPs) on the final TEP profile is not constant but changes in time according to the relative magnitude of these artifacts to the strength of the signal of interest. We know from purely auditory or somatosensory experiments that the amplitude of PEPs tends to increase in time, with the first detectable peaks being relatively weak and spatially localized and the later ones – such as the famous vertex potential – strong, widespread, and likely reflecting the successful integration of the perceived stimulus. Conversely, the cortically evoked brain response might have a decreasing tendency, starting as a strong but chaotic and 'unnatural' activation of the target cortical area that possibly spreads to other connected regions, yet, as it comes out of context and has no intelligible content, it is quickly dampened by the safeguard inhibitory mechanisms of the brain. If this is the case, we could expect the early TEP components to be mostly generated by the activity within the stimulated network, the late ones to be dominated by the PEP signal, and the intermediate ones to reflect a variable mix of both. Therefore, by focusing on the early latency TEPs, we could ignore the artifactual contribution and use this signal to characterize the functional state of the target area. The question remains, what precisely 'early' means? Which TEP components can be still considered as mainly pertaining to the activity within the stimulated brain network, and which are already too corrupted by simultaneous PEPs?

Our observations presented in this dissertation provide some responses to these questions, while being largely in agreement with the hypothesis introduced above. In the first paper, we compared TEPs

evoked by stimulation of two different cortical areas, the left M1 and the left AG, and found that the topographic features of both signals are highly dissimilar at early latencies and gradually converge to be almost identical in the late components N100 and P180. Because we assume that PEPs evoked by both stimuli have similar spatiotemporal features (although their magnitude might vary between targets), it is likely that these late peaks reflect the sensory brain response. Admittedly, relying solely on our results, we cannot exclude the possibility that this target-unspecific response represents a natural convergent outcome of any TEP independently on the target. However, as multiple other studies reached the same conclusion as us while employing a range of different approaches [154, 160, 178, 184], the PEP involvement in the generation of components N100 and P180 seems indisputable.

In the first study, the earlier TEP components were attributed to the activity within the stimulated network, although some common topographic features were observed as early as 50 ms post stimulus and we speculated about their link to the sensory response. These inferences can be further developed based on the findings presented in the third paper. There, while stimulating the AG, we showed that even small changes in the coil orientation may lead to a differential recruitment of the underlying head muscles, which clearly translates into differences in the resulting TEP topography. More precisely, we identified a bipolar pattern that strongly resembles the typical distribution of early SEPs and appears at the latency corresponding to the AG TEP component N45. Coincidentally, in AG and sub-threshold M1 TEPs across all studies, most datasets showed significant topographic inconsistency around 45 ms post stimulus, marking a period of excessive inter-subject variability surprisingly conserved in time and across conditions. We propose that this could be explained by the individual differences in the presence and magnitude of the TMS-evoked muscular artifact, which would lead to a variable manifestation of the associated bipolar topography of N45. Importantly, these findings indicate that TEPs may be contaminated by PEP already as early as 40 – 50 ms post stimulus and that the muscular contraction might considerably augment their contribution relative to the signal of interest.

If we assume that our conclusion is true and N45 in AG and sub-threshold M1 TEPs contains a large contribution of the SEP in response to the TMS-evoked twitch of head muscles, a doubt is also cast upon the origin of this component in supra-threshold M1 TEPs. In the first paper, we showed that the topography of almost all peaks of M1 TEPs changes drastically if the stimulation provokes a measurable contraction in the hand muscle. While the very early component N17 was linked to the cortico-spinal output of the motor network and proposed as a possible biomarker of its excitability (see chapter 7.2), later peaks (except of P30) were clearly influenced either by the recurrent sensory response or by the continuing activation of sensory-motor circuits. At medium latencies, the TEP profile was dominated by a strong, supra-threshold specific P60, and although a deflection in voltage could be observed at the latency of N45, the microstate model did not define this component by a separate class map. Therefore, we can speculate that such subtle peak may in fact reflect the

superposition of a high-amplitude cortical activity generating the P60 topography and a weak SEP (or powerful but occurring only in a subset of subjects) that would normally produce the previously described bipolar pattern. This would, of course, strongly undermine the validity of the component N45 as a biomarker of the excitability in the motor or any other target network.

At this point, however, it must be emphasized that our hypothesis about the origin of N45 reposes largely on the results of a single exploratory study in AG TEPs and needs to be properly tested in a planned experiment. It would be necessary to establish a clear correlation between the amplitude of N45, the specific topographic pattern we identified and the magnitude of the evoked muscle twitch, and this validation should be done in responses recorded from several stimulation sites. An emphasis should be placed on supra-threshold M1 TEPs, since N45 was the most explored in this data and, in many instances, considered informative of the target network excitability. It would be also interesting to see, if it is possible to suppress the occurrence of N45 by preventing the face muscles from contracting, for example by using local anesthesia.

Finally, hereby documented early PEP contribution to TEPs and its apparent link to the somatosensory stimulation justifies – and requires – the future employment of advanced neuronavigation and targeting techniques that would enable precise localization and optimal stimulation of the cortical site of interest. Presumably, optimizing of all stimulation parameters would allow to minimize the TMS intensity necessary for effective engagement of the target neuronal population and thereby reduce (if not completely avoid) the stimulation of peripheral receptors. Ideally, the target site would be identified based on personal characteristics, such as structural or functional brain connectivity [369], and the coil placement would be determined using realistic E-field modelling [75-77]. The routine use of a MRI-based neuronavigation system seems now almost obligatory, as it substantially improves the reproducibility of the stimulation by ensuring the correct coil placement throughout one and across multiple sessions [370]. Further improvements could be achieved by implementing a real-time EEG visualization tool, such as the one recently introduced by Casarotto et al., that allows to map the whole cortical area under investigation, find the site associated with the clearest TEP response and determine the minimal efficient TMS dosage [371].

To conclude, our findings support the pre-existing notion that early TEP components reflect (at least to a large extent) the activity in the stimulated brain network, although it now became clear that PEPs substantially contribute to the signal already at the medium latencies. Such contamination possibly occurs even earlier that we assumed, at latencies corresponding to the component N45, which is possibly linked specifically to the SEP triggered by the twitch of head muscles. These observations allowed us to identify early TEP components of interest that may represent promising biomarkers of cortical excitability in the target brain areas – the M1 and the AG – and the associated networks.

7.2. TEP signature of $GABA_AR$-mediated inhibition

It is generally recognised that the TEPs, like any EEG signal, mainly reflect strong, highly synchronous shifts in the electric charge within large neural populations – but we are in dark as to which type of activity of which neurons is responsible for individual TEP components. To efficiently use TEPs to assess the functional properties of the stimulated network, it is thus vital to determine the character of the underlying neural events. One cannot simply assume that a larger amplitude equals greater cortical excitability, since a single component can be generated both by excitatory and inhibitory processes. As argued in the previous section, hereby presented findings support the claim that the early latency TEPs – specific for the site of stimulation – correspond mostly to the brain activity evoked within the stimulated network. In this section, we will discuss how these components relate to the local cortical excitability and specifically to the state of the fast inhibitory neurotransmission mediated by $GABA_ARs$.

We addressed this question in the second study presented in this manuscript, where we explored two different ways of experimental modulation of the inhibitory signalling: pharmacological $GABA_AR$ activation using alprazolam (its effect was evaluated in all three TEP datasets) and paired-pulse TMS stimulation designed to elicit SICI (only recorded in supra-threshold M1 TEPs). Because both interventions presumably increase the fast $GABA_AR$-mediated inhibitory activity, we assumed that they would modulate the supra-threshold M1 TEPs in a similar fashion. In line with our expectations, we observed in both cases a clear suppression of the early peak N17 and the magnitude of these changes was correlated in individual subjects. Such findings are particularly exciting, considering the high target specificity of this component and its likely association to the cortico-spinal motor output (as discussed at length in chapter 3). Therefore, our first two studies together confirm the validity of N17 as a biomarker of motor network excitability and highlight its relevance for the evaluation of local $GABA_A$ergic inhibition. Naturally, our claims now need to be verified in a large-cohort study that would also allow to establish normative values in heathy subjects.

In AG and sub-threshold M1 TEPs, we did not find any significant alprazolam-induced modulation of the early components of interest, which suggests that these might be preferentially generated by excitatory neurotransmission. This could be expected in the peak P30 in sub-threshold M1 TEPs, if indeed this component reflects the same neural events as P30 in supra-threshold M1 TEPs (an assumption that we supported in our first study by associating the same microstates with both components), which was previously attributed to the excitatory signalling [181, 182]. However, it is also conceivable that the effect of medication was simply too small to be captured by the methods we used. Considering the low number of trials we recorded and the general noisiness of EEG data aggravated by TEP-specific artifacts, the probability of falsely negative results is far from negligible and

may be particularly pertinent in the case of the AG, as we cannot exclude the possibility that sub-optimal stimulation parameters were used to record the TEPs. Furthermore, we saw a tendency to an increase of the AG TEP component P25 following the administration of alprazolam as compared to a tendency to decrease observed after the placebo.

Therefore, in the next step, we conducted another experiment with the aim to verify the (absence of) contribution of $GABA_AR$-mediated inhibition to early TEPs recorded from the AG. The results of our third study allowed us to thoroughly characterize the spatiotemporal profile of this response and to describe the optimal set of TMS parameters for the TEP acquisition. Proceeding from these findings, we then investigated the effect of increased local cortical inhibition on AG TEPs using the paired-pulse protocol previously tested in the M1. Perhaps expectedly, the analysis (see chapter 6.3) revealed several crucial differences between the TEP signature of SICI in the M1 and the AG. Such observation is in line with the assumption that the underlying neural processes likely involve distinct sets of brain regions and the TEP components presumably correspond, at least partially, to different neural events.

The pre-activation of local inhibitory interneurons led to an increase in the amplitude of the AG TEP component of interest, P25, and this effect was clearly observable following the application of all three types of CS. Interestingly, P25 was labelled with two different microstates, indicating that two distinct, partially overlapping processes may contribute to the generation of this component. The earlier part of P25 in particular – here labelled P20 – seems to be sensitive to the paired-pulse stimulation, with the CS of 80% rMT causing the greatest increase of its amplitude. Therefore, it is possible that P20 reflects the inhibitory $GABA_AR$-mediated signalling within the AG and/or other closely connected areas, and that the efficiency of this local inhibition could be assessed using the paired-pulse protocol. However, although we observed clear differences in the data, the parametric statistical analysis we have performed did not confirm their significance. This may be to a large extent related to the relatively low number of participants included in the final analysis, if the SICI influence on the average AG TEP waveform is small or highly variable across individuals and could be improved by simply increasing the number of subjects. Moreover, considering the character of the data, it may be interesting to evaluate the effect of SICI in AG TEPs using more advanced mixed models.

It is also worth mentioning that the paired-pulse TMS applied to the AG led to a clear dose-dependent amplitude augmentation at the latencies corresponding to the late TEP peaks N100 and P180. Because in the first study we have identified these components as primarily generated by PEPs, their increase might be explained by the additive character of somatosensory and auditory stimuli whose processing is presumably unhindered by the increased inhibition within the AG. Interestingly, such observation is in direct contrast to the SICI in supra-threshold M1 TEPs, which manifested as a clear suppression of N100. This can be possibly explained by a differential effect of SICI on two parallel cortical processes contributing to this component in supra-threshold M1 TEPs. In other words, even if

the amplitude of PEPs augments following the paired-pulse stimulation, this increase might be counterbalanced – and overcome – in the case of M1 by a suppression of another simultaneous process affected by the initial boost of local inhibition. This suggests that the SICI-induced reduction of the N100 amplitude in supra-threshold M1 TEPs might provide an indirect information of the state of the $GABA_A$ergic inhibition in the sensory-motor network, although the parallel amplitude increase due to increase in PEPs must be always factored in when the changes in N100 are interpreted.

In summary, the finding presented in this manuscript provide evidence that early TEP components can be used to assess the state of $GABA_A$R-mediated inhibition in different stimulated brain networks. Furthermore, our observations in supra-threshold M1 TEPs indicate that paired-pulse stimulation and medication with benzodiazepines share a similar mechanism of action, therefore supporting the assumption that the conditioning TMS pulse activates local interneurons that inhibit the target site via the fast $GABA_A$ergic neurotransmission.

7.3. The utility of topographic analysis for TEP evaluation

In the studies presented in this manuscript, we introduced a novel approach to evaluate TEPs based on the global topography of the response – more specifically, we used analysis of topographic dissimilarity and microstate analysis to characterize and compare the spatiotemporal profile of different TEPs. Until now, these methods have been mostly ignored by the TMS-EEG community, although their application is otherwise becoming increasingly popular thanks to the multiple advantages they offer. By treating the signals of all EEG channels as a single multidimensional vector, topographic analysis allows to consider the total of available information and thus avoids the arbitrary selection of electrodes of interest. It also prevents the bias introduced by the choice of the reference [272, 273]. Yet, the greatest potential of this approach lies in the possibility to associate specific topographic patterns to the activity of distinct sets of neuronal generators. This means that by comparing topographies across datasets or timepoints, it is possible to isolate the underlying cortical processes and to assess their temporal properties without necessarily localizing their sources.

This is extremely useful when evaluating the significance of complex signals of heterogenous origin, such as TEPs. As we demonstrated, by comparing different types of TEPs, topographic analysis can help identify the components that most likely reflect the genuine TMS-evoked activity within the stimulated brain network and therefore represent specific biomarkers of local excitability. On the other hand, by revealing the substantial influence of muscle-related PEPs on the TEP topography, our results also highlight the need to eliminate (or at least quantify) the confounding factors linked to the inter-subject and inter-condition variability in TMS coil placement.

Furthermore, we showed that TEPs can be segmented into microstates that mostly correspond to individual TEP components. It is then possible to attribute to each microstate – and by consequence

to each component - its typical voltage distribution and to extract temporal characteristics, such as its onset, duration, or centre of gravity. These can be compared across conditions to evaluate the subtle differences in the timing of the underlying neural events, which may be detectable even when the microstate sequence and magnitude of compared TEPs are the same. Therefore, microstate analysis represents a highly sensitive tool that allows to make inferences about the dynamics of neural processes that generate TEPs.

Moreover, previous ERP studies demonstrated that the direct link between a microstate and a component of interest can be exploited to inform the source localization of the EEG signal: instead of estimating the sources for each timepoint of each condition, it is possible to compute the inverse solution for the template map associated to the given microstate [372-374]. Apart from greatly simplifying the analysis, such approach also avoids the arbitrary choice of the time of interest and, by considering the refined microstate topography, it reduces the noisiness of the input data. Admittedly, this probably leads to a certain loss of information (as it is the case with any averaging technique) that may further depend on the choice of parameters used for the microstate computation. Nevertheless, in future, microstate-based source localization may provide a useful tool for the identification of TEP generators. For example, it would be interesting to estimate the sources that produce the topography associated with the twitch of head muscles, as discussed in the first section.

Because topographic analysis focuses on the qualitative aspects of the data and operates with normalized datasets, it does not provide much information about the quantitative differences across conditions. It is therefore recommended to supplement it by some kind of amplitude analysis [280]. The usual method of choice, at least in the TMS-EEG field, would be a point-by-point comparison at each EEG channel using cluster-based randomization statistics. However, while this approach has many advantages, it requires temporal consistency in data across subjects and across conditions – an assumption that is often considerably violated in TEPs [114]. This may pose particular problems when evaluating the early, short-lasting TEP components of interest. To deal with the inter-subject variability in peak latency, we propose that the spatiotemporal features of individual microstates may also serve as a prior for the extraction of the TEP peak amplitude. In the second presented study (see chapter four), we selected the electrodes of interest based on the microstate topography and for each subject, we identified the peak within a time window whose span and onset (adjustable) was defined by the microstate duration. Using this procedure, a single peak value is obtained for each participant and condition and such simple dataset can be then fed to a statistical model of choice.

It must be nevertheless emphasized that by choosing the electrodes of interest, we inevitably disregard a great amount of information contained in the data. For that reason, our approach might not be suitable for the analysis of later TEP components that presumably reflect several overlapping signals – each of these may react differently to the experimental manipulation and it is therefore

impossible to determine in advance the location of the effect. However, if we assume that the early TEP components mainly reflect the activity of the stimulated brain network, it seems likely that any changes in the amplitude would be mainly detectable at the maxima and minima defined by the corresponding microstate topography.

To conclude, hereby presented studies illustrate the utility of analysis of topographic dissimilarity and microstate analysis in the evaluation of TEPs. By focusing on the global topography, these methods allow to describe the dynamics of the neural events that generate the recorded signal and to compare the spatiotemporal profiles of different responses. Therefore, in combination with appropriate amplitude analysis, they likely provide more information that is less influenced by arbitrary choices made by the researcher than amplitude-based approaches alone.

8. Bibliography

1. Jonas, P., *The time course of signaling at central glutamatergic synapses.* Physiology, 2000. **15**(2): p. 83-89.
2. Sallard, E., D. Letourneur, and P. Legendre, *Electrophysiology of ionotropic GABA receptors.* Cellular and Molecular Life Sciences, 2021. **78**(13): p. 5341-5370.
3. Lüscher, C., et al., *G protein-coupled inwardly rectifying K+ channels (GIRKs) mediate postsynaptic but not presynaptic transmitter actions in hippocampal neurons.* Neuron, 1997. **19**(3): p. 687-695.
4. Pérez-Garci, E., et al., *The GABAB1b isoform mediates long-lasting inhibition of dendritic Ca2+ spikes in layer 5 somatosensory pyramidal neurons.* Neuron, 2006. **50**(4): p. 603-616.
5. Bean, B.P., *The action potential in mammalian central neurons.* Nature Reviews Neuroscience, 2007. **8**(6): p. 451-465.
6. Meyer, H.S., et al., *Inhibitory interneurons in a cortical column form hot zones of inhibition in layers 2 and 5A.* Proceedings of the National Academy of Sciences, 2011. **108**(40): p. 16807-16812.
7. Narayanan, R.T., et al., *Beyond columnar organization: cell type-and target layer-specific principles of horizontal axon projection patterns in rat vibrissal cortex.* Cerebral cortex, 2015. **25**(11): p. 4450-4468.
8. Young, A.B. and D. Chu, *Distribution of GABAA and GABAB receptors in mammalian brain: potential targets for drug development.* Drug development research, 1990. **21**(3): p. 161-167.
9. Bloom, F. and L. Iversen, *Localizing 3H-GABA in nerve terminals of rat cerebral cortex by electron microscopic autoradiography.* Nature, 1971. **229**(5287): p. 628-630.
10. Markram, H., et al., *Interneurons of the neocortical inhibitory system.* Nature reviews neuroscience, 2004. **5**(10): p. 793-807.
11. Tremblay, R., S. Lee, and B. Rudy, *GABAergic interneurons in the neocortex: from cellular properties to circuits.* Neuron, 2016. **91**(2): p. 260-292.
12. DeFelipe, J., et al., *New insights into the classification and nomenclature of cortical GABAergic interneurons.* Nature Reviews Neuroscience, 2013. **14**(3): p. 202-216.
13. Fino, E. and R. Yuste, *Dense inhibitory connectivity in neocortex.* Neuron, 2011. **69**(6): p. 1188-1203.
14. Roux, L. and G. Buzsáki, *Tasks for inhibitory interneurons in intact brain circuits.* Neuropharmacology, 2015. **88**: p. 10-23.
15. Feldmeyer, D., et al., *Inhibitory interneurons and their circuit motifs in the many layers of the barrel cortex.* Neuroscience, 2018. **368**: p. 132-151.
16. Okun, M. and I. Lampl, *Instantaneous correlation of excitation and inhibition during ongoing and sensory-evoked activities.* Nature neuroscience, 2008. **11**(5): p. 535-537.
17. Wu, G.K., et al., *Lateral sharpening of cortical frequency tuning by approximately balanced inhibition.* Neuron, 2008. **58**(1): p. 132-143.
18. Poo, C. and J.S. Isaacson, *Odor representations in olfactory cortex:"sparse" coding, global inhibition, and oscillations.* Neuron, 2009. **62**(6): p. 850-861.
19. Anderson, J.S., M. Carandini, and D. Ferster, *Orientation tuning of input conductance, excitation, and inhibition in cat primary visual cortex.* Journal of neurophysiology, 2000. **84**(2): p. 909-926.
20. Atallah, B.V. and M. Scanziani, *Instantaneous modulation of gamma oscillation frequency by balancing excitation with inhibition.* Neuron, 2009. **62**(4): p. 566-577.

21. Isaacson, J.S. and M. Scanziani, *How inhibition shapes cortical activity.* Neuron, 2011. **72**(2): p. 231-243.

22. Herstel, L.J. and C.J. Wierenga, *Network control through coordinated inhibition.* Current Opinion in Neurobiology, 2021. **67**: p. 34-41.

23. Rubin, D.B., S.D. Van Hooser, and K.D. Miller, *The stabilized supralinear network: a unifying circuit motif underlying multi-input integration in sensory cortex.* Neuron, 2015. **85**(2): p. 402-417.

24. Moore, A.K., et al., *Rapid rebalancing of excitation and inhibition by cortical circuitry.* Neuron, 2018. **97**(6): p. 1341-1355. e6.

25. Murphy, B.K. and K.D. Miller, *Balanced amplification: a new mechanism of selective amplification of neural activity patterns.* Neuron, 2009. **61**(4): p. 635-648.

26. Joglekar, M.R., et al., *Inter-areal balanced amplification enhances signal propagation in a large-scale circuit model of the primate cortex.* Neuron, 2018. **98**(1): p. 222-234. e8.

27. Chen, G., et al., *Distinct inhibitory circuits orchestrate cortical beta and gamma band oscillations.* Neuron, 2017. **96**(6): p. 1403-1418. e6.

28. Cardin, J.A., et al., *Driving fast-spiking cells induces gamma rhythm and controls sensory responses.* Nature, 2009. **459**(7247): p. 663-667.

29. Veit, J., et al., *Cortical gamma band synchronization through somatostatin interneurons.* Nature neuroscience, 2017. **20**(7): p. 951-959.

30. Buzsáki, G. and X.-J. Wang, *Mechanisms of gamma oscillations.* Annual review of neuroscience, 2012. **35**: p. 203.

31. Fukunaga, I., et al., *Independent control of gamma and theta activity by distinct interneuron networks in the olfactory bulb.* Nature neuroscience, 2014. **17**(9): p. 1208-1216.

32. Hahn, G., et al., *Portraits of communication in neuronal networks.* Nature Reviews Neuroscience, 2019. **20**(2): p. 117-127.

33. Turrigiano, G., *Too many cooks? Intrinsic and synaptic homeostatic mechanisms in cortical circuit refinement.* Annual review of neuroscience, 2011. **34**: p. 89-103.

34. Bourne, J.N. and K.M. Harris, *Coordination of size and number of excitatory and inhibitory synapses results in a balanced structural plasticity along mature hippocampal CA1 dendrites during LTP.* Hippocampus, 2011. **21**(4): p. 354-373.

35. Hiratani, N. and T. Fukai, *Detailed dendritic excitatory/inhibitory balance through heterosynaptic spike-timing-dependent plasticity.* Journal of Neuroscience, 2017. **37**(50): p. 12106-12122.

36. Field, R.E., et al., *Heterosynaptic plasticity determines the set point for cortical excitatory-inhibitory balance.* Neuron, 2020. **106**(5): p. 842-854. e4.

37. Sohal, V.S. and J.L. Rubenstein, *Excitation-inhibition balance as a framework for investigating mechanisms in neuropsychiatric disorders.* Molecular psychiatry, 2019. **24**(9): p. 1248-1257.

38. Marín, O., *Interneuron dysfunction in psychiatric disorders.* Nature Reviews Neuroscience, 2012. **13**(2): p. 107-120.

39. Staley, K., *Molecular mechanisms of epilepsy.* Nature neuroscience, 2015. **18**(3): p. 367-372.

40. Shaw, A.D., et al., *Oscillatory, computational, and behavioral evidence for impaired GABAergic inhibition in schizophrenia.* Schizophrenia bulletin, 2020. **46**(2): p. 345-353.

41. Nelson, S.B. and V. Valakh, *Excitatory/inhibitory balance and circuit homeostasis in autism spectrum disorders.* Neuron, 2015. **87**(4): p. 684-698.

42. Van den Bos, M.A., et al., *Imbalance of cortical facilitatory and inhibitory circuits underlies hyperexcitability in ALS.* Neurology, 2018. **91**(18): p. e1669-e1676.

43. Maestú, F., et al., *Neuronal Excitation/Inhibition imbalance: a core element of a translational perspective on Alzheimer pathophysiology.* Ageing Research Reviews, 2021: p. 101372.

44. Raffin, E., et al., *Probing regional cortical excitability via input–output properties using transcranial magnetic stimulation and electroencephalography coupling.* Human Brain Mapping, 2020. **41**(10): p. 2741-2761.

45. Pascual-Leone, A., et al., *Study and modulation of human cortical excitability with transcranial magnetic stimulation.* Journal of clinical neurophysiology, 1998. **15**(4): p. 333-343.

46. Barker, A.T., R. Jalinous, and I.L. Freeston, *Non-invasive magnetic stimulation of human motor cortex.* The Lancet, 1985. **325**(8437): p. 1106-1107.

47. Merton, P., et al., *Scope of a technique for electrical stimulation of human brain, spinal cord, and muscle.* The Lancet, 1982. **320**(8298): p. 597-600.

48. Merton, P. and H. Morton, *Stimulation of the cerebral cortex in the intact human subject.* Nature, 1980. **285**(5762): p. 227-227.

49. Rossini, P.M., et al., *Non-invasive electrical and magnetic stimulation of the brain, spinal cord, roots and peripheral nerves: basic principles and procedures for routine clinical and research application. An updated report from an IFCN Committee.* Clinical Neurophysiology, 2015. **126**(6): p. 1071-1107.

50. Hallett, M., *Transcranial magnetic stimulation: a primer.* Neuron, 2007. **55**(2): p. 187-199.

51. Groppa, S., et al., *A practical guide to diagnostic transcranial magnetic stimulation: report of an IFCN committee.* Clinical Neurophysiology, 2012. **123**(5): p. 858-882.

52. Kammer, T., et al., *Motor thresholds in humans: a transcranial magnetic stimulation study comparing different pulse waveforms, current directions and stimulator types.* Clinical neurophysiology, 2001. **112**(2): p. 250-258.

53. Maxwell, J.C., *A treatise on electricity and magnetism*. Vol. 1. 1873: Clarendon press.

54. Wagner, T., A. Valero-Cabre, and A. Pascual-Leone, *Noninvasive human brain stimulation.* Annual review of biomedical engineering, 2007. **9**(1): p. 527-565.

55. Opitz, A., et al., *How the brain tissue shapes the electric field induced by transcranial magnetic stimulation.* Neuroimage, 2011. **58**(3): p. 849-859.

56. Goetz, S.M. and Z.-D. Deng, *The development and modelling of devices and paradigms for transcranial magnetic stimulation.* International Review of Psychiatry, 2017. **29**(2): p. 115-145.

57. Siebner, H.R., et al., *Transcranial magnetic stimulation of the brain: What is stimulated?–a consensus and critical position paper.* Clinical Neurophysiology, 2022.

58. Hannah, R. and J.C. Rothwell, *Pulse duration as well as current direction determines the specificity of transcranial magnetic stimulation of motor cortex during contraction.* Brain stimulation, 2017. **10**(1): p. 106-115.

59. D'Ostilio, K., et al., *Effect of coil orientation on strength–duration time constant and I-wave activation with controllable pulse parameter transcranial magnetic stimulation.* Clinical Neurophysiology, 2016. **127**(1): p. 675-683.

60. Peterchev, A.V., et al., *Pulse width dependence of motor threshold and input–output curve characterized with controllable pulse parameter transcranial magnetic stimulation.* Clinical Neurophysiology, 2013. **124**(7): p. 1364-1372.

61. Bikson, M., J. Dmochowski, and A. Rahman, *The "quasi-uniform" assumption in animal and computational models of non-invasive electrical stimulation.* Brain Stimulation: Basic, Translational, and Clinical Research in Neuromodulation, 2013. **6**(4): p. 704-705.

62. Aberra, A.S., A.V. Peterchev, and W.M. Grill, *Biophysically realistic neuron models for simulation of cortical stimulation.* Journal of neural engineering, 2018. **15**(6): p. 066023.

63. Salvador, R., et al., *Determining which mechanisms lead to activation in the motor cortex: a modeling study of transcranial magnetic stimulation using realistic stimulus waveforms and sulcal geometry.* Clinical neurophysiology, 2011. **122**(4): p. 748-758.

64. De Geeter, N., L. Dupré, and G. Crevecoeur, *Modeling transcranial magnetic stimulation from the induced electric fields to the membrane potentials along tractography-based white matter fiber tracts.* Journal of neural engineering, 2016. **13**(2): p. 026028.

65. Gomez–Tames, J., et al., *TMS activation site estimation using multiscale realistic head models.* Journal of Neural Engineering, 2020. **17**(3): p. 036004.

66. Aberra, A.S., et al., *Simulation of transcranial magnetic stimulation in head model with morphologically-realistic cortical neurons.* Brain stimulation, 2020. **13**(1): p. 175-189.

67. Sakai, K., et al., *Preferential activation of different I waves by transcranial magnetic stimulation with a figure-of-eight-shaped coil.* Experimental Brain Research, 1997. **113**(1): p. 24-32.

68. Werhahn, K., et al., *The effect of magnetic coil orientation on the latency of surface EMG and single motor unit responses in the first dorsal interosseous muscle.* Electroencephalography and Clinical Neurophysiology/Evoked Potentials Section, 1994. **93**(2): p. 138-146.

69. Di Lazzaro, V., et al., *The effect on corticospinal volleys of reversing the direction of current induced in the motor cortex by transcranial magnetic stimulation.* Experimental brain research, 2001. **138**(2): p. 268-273.

70. Di Lazzaro, V. and J.C. Rothwell, *Corticospinal activity evoked and modulated by non-invasive stimulation of the intact human motor cortex.* The Journal of physiology, 2014. **592**(19): p. 4115-4128.

71. Mills, K., S. Boniface, and M. Schubert, *Magnetic brain stimulation with a double coil: the importance of coil orientation.* Electroencephalography and clinical neurophysiology/Evoked potentials section, 1992. **85**(1): p. 17-21.

72. Brasil-Neto, J.P., et al., *Optimal focal transcranial magnetic activation of the human motor cortex: effects of coil orientation, shape of the induced current pulse, and stimulus intensity.* Journal of clinical neurophysiology: official publication of the American Electroencephalographic Society, 1992. **9**(1): p. 132-136.

73. Pisoni, A., et al., *TMS orientation and pulse waveform manipulation activates different neural populations: direct evidence from TMS-EEG.* BioRxiv, 2018: p. 308981.

74. Casarotto, S., et al., *EEG responses to TMS are sensitive to changes in the perturbation parameters and repeatable over time.* PloS one, 2010. **5**(4): p. e10281.

75. Bungert, A., et al., *Where does TMS stimulate the motor cortex? Combining electrophysiological measurements and realistic field estimates to reveal the affected cortex position.* Cerebral Cortex, 2017. **27**(11): p. 5083-5094.

76. Laakso, I., et al., *Where and what TMS activates: experiments and modeling.* Brain Stimulation, 2018. **11**(1): p. 166-174.

77. Weise, K., et al., *A novel approach to localize cortical TMS effects.* Neuroimage, 2020. **209**: p. 116486.

78. Gomez-Tames, J., et al., *Atlas of optimal coil orientation and position for TMS: A computational study.* Brain stimulation, 2018. **11**(4): p. 839-848.

79. Gomez, L.J., M. Dannhauer, and A.V. Peterchev, *Fast computational optimization of TMS coil placement for individualized electric field targeting.* Neuroimage, 2021. **228**: p. 117696.

80. Cohen, L.G., et al., *Effects of coil design on delivery of focal magnetic stimulation. Technical considerations.* Electroencephalography and clinical neurophysiology, 1990. **75**(4): p. 350-357.

81. Deng, Z.-D., S.H. Lisanby, and A.V. Peterchev, *Coil design considerations for deep transcranial magnetic stimulation.* Clinical Neurophysiology, 2014. **125**(6): p. 1202-1212.

82. Guadagnin, V., et al., *Deep transcranial magnetic stimulation: modeling of different coil configurations.* IEEE Transactions on Biomedical Engineering, 2015. **63**(7): p. 1543-1550.

83. Tendler, A., et al., *Deep transcranial magnetic stimulation (dTMS)–beyond depression.* Expert review of medical devices, 2016. **13**(10): p. 987-1000.

84. Gomez, L.J., S.M. Goetz, and A.V. Peterchev, *Design of transcranial magnetic stimulation coils with optimal trade-off between depth, focality, and energy.* Journal of neural engineering, 2018. **15**(4): p. 046033.

85. Deng, Z.-D., S.H. Lisanby, and A.V. Peterchev, *Electric field depth–focality tradeoff in transcranial magnetic stimulation: simulation comparison of 50 coil designs.* Brain stimulation, 2013. **6**(1): p. 1-13.

86. Romero, M.C., et al., *Neural effects of transcranial magnetic stimulation at the single-cell level.* Nature communications, 2019. **10**(1): p. 2642.

87. Gentner, R. and J. Classen, *Modular organization of finger movements by the human central nervous system.* Neuron, 2006. **52**(4): p. 731-742.

88. Nudo, R.J., et al., *Use-dependent alterations of movement representations in primary motor cortex of adult squirrel monkeys.* The Journal of neuroscience, 1996. **16**(2): p. 785.

89. Passera, B., et al., *Exploring the spatial resolution of TMS-EEG coupling on the sensorimotor region.* NeuroImage, 2022. **259**: p. 119419.

90. Berger, H., *Über das elektroenkephalogramm des menschen.* Archiv für psychiatrie und nervenkrankheiten, 1929. **87**(1): p. 527-570.

91. Niedermeyer, E. and F.L. da Silva, *Electroencephalography: basic principles, clinical applications, and related fields*. 2005: Lippincott Williams & Wilkins.

92. Bressler, S.L. and E. Tognoli, *Operational principles of neurocognitive networks.* International journal of psychophysiology, 2006. **60**(2): p. 139-148.

93. Teplan, M., *Fundamentals of EEG measurement.* Measurement science review, 2002. **2**(2): p. 1-11.

94. Nunez, P.L. and R. Srinivasan, *Electric fields of the brain: the neurophysics of EEG*. 2006: Oxford University Press, USA.

95. da Silva, F.L., *EEG and MEG: relevance to neuroscience.* Neuron, 2013. **80**(5): p. 1112-1128.

96. Buzsáki, G., C.A. Anastassiou, and C. Koch, *The origin of extracellular fields and currents—EEG, ECoG, LFP and spikes.* Nature reviews neuroscience, 2012. **13**(6): p. 407-420.

97. Kirschstein, T. and R. Köhling, *What is the source of the EEG?* Clinical EEG and neuroscience, 2009. **40**(3): p. 146-149.

98. He, B.J., et al., *The temporal structures and functional significance of scale-free brain activity.* Neuron, 2010. **66**(3): p. 353-369.

99. Buzsaki, G. and A. Draguhn, *Neuronal oscillations in cortical networks.* science, 2004. **304**(5679): p. 1926-1929.

100. Klimesch, W., *EEG alpha and theta oscillations reflect cognitive and memory performance: a review and analysis.* Brain research reviews, 1999. **29**(2-3): p. 169-195.

101. Buzsaki, G., *Rhythms of the Brain*. 2006: Oxford university press.

102. Cohen, M.X., *Where does EEG come from and what does it mean?* Trends in neurosciences, 2017. **40**(4): p. 208-218.

103. Siegel, M., T.H. Donner, and A.K. Engel, *Spectral fingerprints of large-scale neuronal interactions.* Nature Reviews Neuroscience, 2012. **13**(2): p. 121-134.

104. Freeman, W.J., *Use of spatial deconvolution to compensate for distortion of EEG by volume conduction.* IEEE Transactions on Biomedical Engineering, 1980(8): p. 421-429.

105. Grech, R., et al., *Review on solving the inverse problem in EEG source analysis.* Journal of neuroengineering and rehabilitation, 2008. **5**(1): p. 1-33.

106. Asadzadeh, S., et al., *A systematic review of EEG source localization techniques and their applications on diagnosis of brain abnormalities.* Journal of Neuroscience Methods, 2020. **339**: p. 108740.

107. Ilmoniemi, R.J. and D. Kičić, *Methodology for combined TMS and EEG.* Brain topography, 2010. **22**(4): p. 233.

108. Bergmann, T.O., et al., *Combining non-invasive transcranial brain stimulation with neuroimaging and electrophysiology: current approaches and future perspectives.* NeuroImage, 2016. **140**: p. 4-19.

109. Cracco, R.Q., et al., *Comparison of human transcallosal responses evoked by magnetic coil and electrical stimulation.* Electroencephalography and Clinical Neurophysiology/Evoked Potentials Section, 1989. **74**(6): p. 417-424.

110. Ilmoniemi, R.J., et al., *Neuronal responses to magnetic stimulation reveal cortical reactivity and connectivity.* Neuroreport, 1997. **8**(16): p. 3537-3540.

111. Tremblay, S., et al., *Clinical utility and prospective of TMS–EEG.* Clinical Neurophysiology, 2019.

112. Farzan, F., et al., *Characterizing and modulating brain circuitry through transcranial magnetic stimulation combined with electroencephalography.* Frontiers in neural circuits, 2016. **10**.

113. Lioumis, P., et al., *Reproducibility of TMS—Evoked EEG responses.* Human brain mapping, 2009. **30**(4): p. 1387-1396.

114. Ozdemir, R.A., et al., *Cortical responses to noninvasive perturbations enable individual brain fingerprinting.* Brain stimulation, 2021. **14**(2): p. 391-403.

115. Harquel, S., et al., *Mapping dynamical properties of cortical microcircuits using robotized TMS and EEG: Towards functional cytoarchitectonics.* Neuroimage, 2016. **135**: p. 115-124.

116. Komssi, S., S. Kähkönen, and R.J. Ilmoniemi, *The effect of stimulus intensity on brain responses evoked by transcranial magnetic stimulation.* Human brain mapping, 2004. **21**(3): p. 154-164.

117. Silvanto, J., N. Muggleton, and V. Walsh, *State-dependency in brain stimulation studies of perception and cognition.* Trends in cognitive sciences, 2008. **12**(12): p. 447-454.

118. Desideri, D., et al., *Phase of sensorimotor μ-oscillation modulates cortical responses to transcranial magnetic stimulation of the human motor cortex.* The Journal of Physiology, 2019. **597**(23): p. 5671-5686.

119. Zazio, A., C. Miniussi, and M. Bortoletto, *Alpha-band cortico-cortical phase synchronization is associated with effective connectivity in the motor network.* Clinical Neurophysiology, 2021. **132**(10): p. 2473-2480.

120. Massimini, M., et al., *Breakdown of cortical effective connectivity during sleep.* Science, 2005. **309**(5744): p. 2228-2232.

121. Huber, R., et al., *Human cortical excitability increases with time awake.* Cerebral cortex, 2013. **23**(2): p. 1-7.

122. Casali, A.G., et al., *General indices to characterize the electrical response of the cerebral cortex to TMS.* Neuroimage, 2010. **49**(2): p. 1459-1468.

123. Rosanova, M., et al., *Natural frequencies of human corticothalamic circuits.* Journal of Neuroscience, 2009. **29**(24): p. 7679-7685.

124. Rogasch, N.C. and P.B. Fitzgerald, *Assessing cortical network properties using TMS–EEG.* Human brain mapping, 2013. **34**(7): p. 1652-1669.

125. Komssi, S. and S. Kähkönen, *The novelty value of the combined use of electroencephalography and transcranial magnetic stimulation for neuroscience research.* Brain research reviews, 2006. **52**(1): p. 183-192.

126. Hallett, M., et al., *Contribution of transcranial magnetic stimulation to assessment of brain connectivity and networks.* Clinical Neurophysiology, 2017. **128**(11): p. 2125-2139.

127. Bortoletto, M., et al., *The contribution of TMS–EEG coregistration in the exploration of the human cortical connectome.* Neuroscience & Biobehavioral Reviews, 2015. **49**: p. 114-124.

128. Veniero, D., M. Bortoletto, and C. Miniussi, *TMS-EEG co-registration: on TMS-induced artifact.* Clinical Neurophysiology, 2009. **120**(7): p. 1392-1399.

129. Thut, G., et al., *A new device and protocol for combining TMS and online recordings of EEG and evoked potentials.* Journal of neuroscience methods, 2005. **141**(2): p. 207-217.

130. Litvak, V., et al., *Artifact correction and source analysis of early electroencephalographic responses evoked by transcranial magnetic stimulation over primary motor cortex.* Neuroimage, 2007. **37**(1): p. 56-70.

131. Virtanen, J., et al., *Instrumentation for the measurement of electric brain responses to transcranial magnetic stimulation.* Medical & biological engineering & computing, 1999. **37**(3): p. 322-326.

132. Freche, D., et al., *A quantitative physical model of the TMS-induced discharge artifacts in EEG.* PLoS computational biology, 2018. **14**(7): p. e1006177.

133. Sekiguchi, H., et al., *TMS-induced artifacts on EEG can be reduced by rearrangement of the electrode's lead wire before recording.* Clinical Neurophysiology, 2011. **122**(5): p. 984-990.

134. Ruddy, K.L., et al., *Improving the quality of combined EEG-TMS neural recordings: Introducing the coil spacer.* Journal of neuroscience methods, 2018. **294**: p. 34-39.

135. Rogasch, N.C., et al., *Short-latency artifacts associated with concurrent TMS–EEG.* Brain Stimulation: Basic, Translational, and Clinical Research in Neuromodulation, 2013. **6**(6): p. 868-876.

136. Fernandez, L., et al., *Assessing cerebellar-cortical connectivity using concurrent TMS-EEG: a feasibility study.* Journal of neurophysiology, 2021. **125**(5): p. 1768-1787.

137. Mancuso, M., et al., *Transcranial evoked potentials can be reliably recorded with active electrodes.* Brain Sciences, 2021. **11**(2): p. 145.

138. Rogasch, N.C., M. Biabani, and T.P. Mutanen, *Designing and comparing cleaning pipelines for TMS-EEG data: a theoretical overview and practical example.* Journal of Neuroscience Methods, 2022: p. 109494.

139. Rogasch, N.C., et al., *Removing artefacts from TMS-EEG recordings using independent component analysis: importance for assessing prefrontal and motor cortex network properties.* Neuroimage, 2014. **101**: p. 425-439.

140. Korhonen, R.J., et al., *Removal of large muscle artifacts from transcranial magnetic stimulation-evoked EEG by independent component analysis.* Medical & biological engineering & computing, 2011. **49**(4): p. 397-407.

141. Mutanen, T., H. Mäki, and R.J. Ilmoniemi, *The effect of stimulus parameters on TMS–EEG muscle artifacts.* Brain stimulation, 2013. **6**(3): p. 371-376.

142. Hernandez-Pavon, J.C., et al., *Uncovering neural independent components from highly artifactual TMS-evoked EEG data.* Journal of Neuroscience methods, 2012. **209**(1): p. 144-157.

143. Metsomaa, J., J. Sarvas, and R.J. Ilmoniemi, *Multi-trial evoked EEG and independent component analysis.* Journal of Neuroscience Methods, 2014. **228**: p. 15-26.

144. ter Braack, E.M., B. de Jonge, and M.J. Van Putten, *Reduction of TMS induced artifacts in EEG using principal component analysis.* IEEE transactions on neural systems and rehabilitation engineering, 2013. **21**(3): p. 376-382.

145. Mäki, H. and R.J. Ilmoniemi, *Projecting out muscle artifacts from TMS-evoked EEG.* Neuroimage, 2011. **54**(4): p. 2706-2710.

146. Mutanen, T.P., et al., *Recovering TMS-evoked EEG responses masked by muscle artifacts.* Neuroimage, 2016. **139**: p. 157-166.

147. Nikulin, V.V., et al., *Modulation of electroencephalographic responses to transcranial magnetic stimulation: evidence for changes in cortical excitability related to movement.* European Journal of Neuroscience, 2003. **18**(5): p. 1206-1212.

148. Nikouline, V., J. Ruohonen, and R.J. Ilmoniemi, *The role of the coil click in TMS assessed with simultaneous EEG.* Clinical Neurophysiology, 1999. **110**(8): p. 1325-1328.

149. Tiitinen, H., et al., *Separation of contamination caused by coil clicks from responses elicited by transcranial magnetic stimulation.* Clinical neurophysiology, 1999. **110**(5): p. 982-985.

150. Conde, V., et al., *The non-transcranial TMS-evoked potential is an inherent source of ambiguity in TMS-EEG studies.* Neuroimage, 2019. **185**: p. 300-312.

151. Russo, S., et al., *TAAC-TMS Adaptable Auditory Control: a universal tool to mask TMS clicks.* Journal of Neuroscience Methods, 2022. **370**: p. 109491.

152. Ross, J.M., M. Sarkar, and C.J. Keller, *Experimental suppression of transcranial magnetic stimulation-electroencephalography sensory potentials.* Human Brain Mapping, 2022.

153. Ilmoniemi, R.J., et al. *Dealing with artifacts in TMS-evoked EEG*. in *2015 37th Annual International Conference of the IEEE Engineering in Medicine and Biology Society (EMBC)*. 2015. IEEE.

154. Rocchi, L., et al., *Disentangling EEG responses to TMS due to cortical and peripheral activations.* Brain stimulation, 2021. **14**(1): p. 4-18.

155. Ter Braack, E.M., C.C. de Vos, and M.J. van Putten, *Masking the auditory evoked potential in TMS–EEG: a comparison of various methods.* Brain topography, 2015. **28**(3): p. 520-528.

156. Biabani, M., et al., *The correspondence between EMG and EEG measures of changes in cortical excitability following transcranial magnetic stimulation.* The Journal of Physiology, 2021. **599**(11): p. 2907-2932.

157. Herring, J.D., et al., *Attention modulates TMS-locked alpha oscillations in the visual cortex.* Journal of Neuroscience, 2015. **35**(43): p. 14435-14447.

158. Gordon, P.C., et al., *Comparison of cortical EEG responses to realistic sham versus real TMS of human motor cortex.* Brain stimulation, 2018. **11**(6): p. 1322-1330.

159. Gordon, P.C., et al., *Recording brain responses to TMS of primary motor cortex by EEG–utility of an optimized sham procedure.* NeuroImage, 2021. **245**: p. 118708.

160. Ross, J.M., et al., *A structured ICA-based process for removing auditory evoked potentials.* Scientific Reports, 2022. **12**(1): p. 1-19.

161. Mouraux, A. and G.D. Iannetti, *Nociceptive laser-evoked brain potentials do not reflect nociceptive-specific neural activity.* Journal of neurophysiology, 2009. **101**(6): p. 3258-3269.

162. Welniarz, Q., I. Dusart, and E. Roze, *The corticospinal tract: Evolution, development, and human disorders.* Developmental neurobiology, 2017. **77**(7): p. 810-829.

163. Strick, P.L., R.P. Dum, and J.-A. Rathelot, *The cortical motor areas and the emergence of motor skills: a neuroanatomical perspective.* Annual Review of Neuroscience, 2021. **44**: p. 425-447.

164. Rivara, C.B., et al., *Stereologic characterization and spatial distribution patterns of Betz cells in the human primary motor cortex.* The Anatomical Record Part A: Discoveries in Molecular, Cellular, and Evolutionary Biology: An Official Publication of the American Association of Anatomists, 2003. **270**(2): p. 137-151.

165. Sanes, J.N. and J.P. Donoghue, *Plasticity and primary motor cortex.* Annual Review of Neuroscience, 2000. **23**: p. 393-415.

166. Kernell, D. and W. Chien-Ping, *Responses of the pyramidal tract to stimulation of the baboon's motor cortex.* The Journal of physiology, 1967. **191**(3): p. 653-672.

167. Patton, H.D. and V.E. Amassian, *Single-and multiple-unit analysis of cortical stage of pyramidal tract activation.* Journal of neurophysiology, 1954. **17**(4): p. 345-363.

168. Nakamura, H., et al., *Intracortical facilitation and inhibition after transcranial magnetic stimulation in conscious humans.* The Journal of physiology, 1997. **498**(3): p. 817-823.

169. Nakamura, H., et al., *Direct and indirect activation of human corticospinal neurons by transcranial magnetic and electrical stimulation.* Neuroscience letters, 1996. **210**(1): p. 45-48.

170. Di Lazzaro, V., et al., *The physiological basis of transcranial motor cortex stimulation in conscious humans.* Clinical neurophysiology, 2004. **115**(2): p. 255-266.

171. Di Lazzaro, V., U. Ziemann, and R.N. Lemon, *State of the art: physiology of transcranial motor cortex stimulation.* Brain stimulation, 2008. **1**(4): p. 345-362.

172. Ziemann, U., *I-waves in motor cortex revisited.* Experimental Brain Research, 2020. **238**(7): p. 1601-1610.

173. Bestmann, S. and J.W. Krakauer, *The uses and interpretations of the motor-evoked potential for understanding behaviour.* Experimental brain research, 2015. **233**(3): p. 679-689.

174. Paus, T., P. Sipila, and A. Strafella, *Synchronization of neuronal activity in the human primary motor cortex by transcranial magnetic stimulation: an EEG study.* Journal of Neurophysiology, 2001. **86**(4): p. 1983-1990.

175. Komssi, S., et al., *Ipsi-and contralateral EEG reactions to transcranial magnetic stimulation.* Clinical Neurophysiology, 2002. **113**(2): p. 175-184.

176. Bonato, C., C. Miniussi, and P. Rossini, *Transcranial magnetic stimulation and cortical evoked potentials: a TMS/EEG co-registration study.* Clinical neurophysiology, 2006. **117**(8): p. 1699-1707.

177. Biabani, M., et al., *Characterizing and minimizing the contribution of sensory inputs to TMS-evoked potentials.* bioRxiv, 2018: p. 489864.

178. Ahn, S. and F. Fröhlich, *Pinging the brain with transcranial magnetic stimulation reveals cortical reactivity in time and space.* Brain Stimulation, 2021. **14**(2): p. 304-315.

179. Esser, S., et al., *A direct demonstration of cortical LTP in humans: a combined TMS/EEG study.* Brain research bulletin, 2006. **69**(1): p. 86-94.

180. Mäki, H. and R.J. Ilmoniemi, *The relationship between peripheral and early cortical activation induced by transcranial magnetic stimulation.* Neuroscience letters, 2010. **478**(1): p. 24-28.

181. Rogasch, N.C., Z.J. Daskalakis, and P.B. Fitzgerald, *Mechanisms underlying long-interval cortical inhibition in the human motor cortex: a TMS-EEG study.* Journal of neurophysiology, 2013. **109**(1): p. 89-98.

182. Darmani, G., et al., *Effects of antiepileptic drugs on cortical excitability in humans: a TMS-EMG and TMS-EEG study.* Human brain mapping, 2019. **40**(4): p. 1276-1289.

183. Petrichella, S., N. Johnson, and B. He, *The influence of corticospinal activity on TMS-evoked activity and connectivity in healthy subjects: A TMS-EEG study.* PLoS One, 2017. **12**(4).

184. Freedberg, M., et al., *Identifying site-and stimulation-specific TMS-evoked EEG potentials using a quantitative cosine similarity metric.* Plos one, 2020. **15**(1): p. e0216185.

185. Biabani, M., et al., *Characterizing and minimizing the contribution of sensory inputs to TMS-evoked potentials.* Brain stimulation, 2019. **12**(6): p. 1537-1552.

186. Premoli, I., et al., *TMS-EEG signatures of GABAergic neurotransmission in the human cortex.* Journal of Neuroscience, 2014. **34**(16): p. 5603-5612.

187. Belardinelli, P., et al., *TMS-EEG signatures of glutamatergic neurotransmission in human cortex.* Scientific reports, 2021. **11**(1): p. 1-14.

188. Darmani, G., et al., *Effects of the selective α5-GABAAR antagonist S44819 on excitability in the human brain: a TMS–EMG and TMS–EEG phase I study.* Journal of Neuroscience, 2016. **36**(49): p. 12312-12320.

189. Bonnard, M., et al., *Prior intention can locally tune inhibitory processes in the primary motor cortex: direct evidence from combined TMS-EEG.* European Journal of Neuroscience, 2009. **30**(5): p. 913-923.

190. Kičić, D., et al., *Bilateral changes in excitability of sensorimotor cortices during unilateral movement: combined electroencephalographic and transcranial magnetic stimulation study.* Neuroscience, 2008. **152**(4): p. 1119-1129.

191. Farzan, F., et al., *The EEG correlates of the TMS-induced EMG silent period in humans.* Neuroimage, 2013. **83**: p. 120-134.

192. Roos, D., et al., *Local Differences in Cortical Excitability–A Systematic Mapping Study of the TMS-Evoked N100 Component.* Frontiers in neuroscience, 2021. **15**: p. 81.

193. Premoli, I., et al., *Lamotrigine and levetiracetam exert a similar modulation of TMS-evoked EEG potentials.* Epilepsia, 2017. **58**(1): p. 42-50.

194. Premoli, I., et al., *Short-interval and long-interval intracortical inhibition of TMS-evoked EEG potentials.* Brain stimulation, 2018.

195. Fox, P.T., et al., *Column-based model of electric field excitation of cerebral cortex.* Human brain mapping, 2004. **22**(1): p. 1-14.

196. Stokes, M.G., et al., *Distance-adjusted motor threshold for transcranial magnetic stimulation.* Clinical Neurophysiology, 2007. **118**(7): p. 1617-1625.

197. Saturnino, G.B., et al., *SimNIBS 2.1: a comprehensive pipeline for individualized electric field modelling for transcranial brain stimulation.* Brain and human body modeling, 2019: p. 3-25.

198. Stewart, L., V. Walsh, and J. Rothwell, *Motor and phosphene thresholds: a transcranial magnetic stimulation correlation study.* Neuropsychologia, 2001. **39**(4): p. 415-419.

199. Noda, Y., et al., *Single-pulse transcranial magnetic stimulation-evoked potential amplitudes and latencies in the motor and dorsolateral prefrontal cortex among young, older healthy participants, and schizophrenia patients.* Journal of personalized medicine, 2021. **11**(1): p. 54.

200. Rogasch, N.C., et al., *The effects of NMDA receptor blockade on TMS-evoked EEG potentials from prefrontal and parietal cortex.* Scientific reports, 2020. **10**(1): p. 1-12.

201. Eshel, N., et al., *Global connectivity and local excitability changes underlie antidepressant effects of repetitive transcranial magnetic stimulation.* Neuropsychopharmacology, 2020. **45**(6): p. 1018-1025.

202. Voineskos, D., et al., *Altered transcranial magnetic stimulation–electroencephalographic markers of inhibition and excitation in the dorsolateral prefrontal cortex in major depressive disorder.* Biological psychiatry, 2019. **85**(6): p. 477-486.

203. Lauro, L.J.R., et al., *TDCS increases cortical excitability: Direct evidence from TMS–EEG.* Cortex, 2014. **58**: p. 99-111.

204. Grasso, P.A., et al., *tDCS over posterior parietal cortex increases cortical excitability but decreases learning: An ERPs and TMS-EEG study.* Brain Research, 2021. **1753**: p. 147227.

205. Fecchio, M., et al., *The spectral features of EEG responses to transcranial magnetic stimulation of the primary motor cortex depend on the amplitude of the motor evoked potentials.* PloS one, 2017. **12**(9): p. e0184910.

206. Zanon, M., et al., *Long-range neural activity evoked by premotor cortex stimulation: a TMS/EEG co-registration study.* Frontiers in human neuroscience, 2013. **7**: p. 803.

207. Salo, K.S.-T., et al., *Individual activation patterns after the stimulation of different motor areas: A transcranial magnetic stimulation–electroencephalography study.* Brain Connectivity, 2018. **8**(7): p. 420-428.

208. Fertonani, A., et al., *Age-related changes in cortical connectivity influence the neuromodulatory effects of transcranial electrical stimulation.* Neurobiology of Aging, 2019. **82**: p. 77-87.

209. Garcia, J.O., E.D. Grossman, and R. Srinivasan, *Evoked potentials in large-scale cortical networks elicited by TMS of the visual cortex.* Journal of neurophysiology, 2011. **106**(4): p. 1734-1746.

210. Croxson, P.L., et al., *Structural variability across the primate brain: a cross-species comparison.* Cerebral Cortex, 2018. **28**(11): p. 3829-3841.

211. Mars, R.B., et al., *Diffusion-weighted imaging tractography-based parcellation of the human parietal cortex and comparison with human and macaque resting-state functional connectivity.* Journal of Neuroscience, 2011. **31**(11): p. 4087-4100.

212. Hill, J., et al., *Similar patterns of cortical expansion during human development and evolution.* Proceedings of the National Academy of Sciences, 2010. **107**(29): p. 13135-13140.

213. Caspers, S., et al., *The human inferior parietal cortex: cytoarchitectonic parcellation and interindividual variability.* Neuroimage, 2006. **33**(2): p. 430-448.

214. Caspers, S., et al., *Organization of the human inferior parietal lobule based on receptor architectonics.* Cerebral Cortex, 2013. **23**(3): p. 615-628.

215. Uddin, L.Q., et al., *Dissociable connectivity within human angular gyrus and intraparietal sulcus: evidence from functional and structural connectivity.* Cerebral cortex, 2010. **20**(11): p. 2636-2646.

216. Wang, J., et al., *Functional topography of the right inferior parietal lobule structured by anatomical connectivity profiles.* Human brain mapping, 2016. **37**(12): p. 4316-4332.

217. Kelly, C., et al., *Broca's region: linking human brain functional connectivity data and non-human primate tracing anatomy studies.* European Journal of Neuroscience, 2010. **32**(3): p. 383-398.

218. Wang, J., et al., *Correspondent Functional Topography of the Human Left Inferior Parietal Lobule at Rest and Under Task Revealed Using Resting-State f MRI and Coactivation Based Parcellation.* Human brain mapping, 2017. **38**(3): p. 1659-1675.

219. Rademacher, J., et al., *Human cerebral cortex: localization, parcellation, and morphometry with magnetic resonance imaging.* Journal of cognitive neuroscience, 1992. **4**(4): p. 352-374.

220. Tomasi, D. and N.D. Volkow, *Association between functional connectivity hubs and brain networks.* Cerebral cortex, 2011. **21**(9): p. 2003-2013.

221. Kernbach, J.M., et al., *Subspecialization within default mode nodes characterized in 10,000 UK Biobank participants.* Proceedings of the National Academy of Sciences, 2018. **115**(48): p. 12295-12300.

222. Seghier, M.L., *The angular gyrus: multiple functions and multiple subdivisions.* The Neuroscientist, 2013. **19**(1): p. 43-61.

223. Binder, J.R. and R.H. Desai, *The neurobiology of semantic memory.* Trends in cognitive sciences, 2011. **15**(11): p. 527-536.

224. Ramanan, S., O. Piguet, and M. Irish, *Rethinking the role of the angular gyrus in remembering the past and imagining the future: the contextual integration model.* The Neuroscientist, 2018. **24**(4): p. 342-352.

225. Humphreys, G.F., M.A.L. Ralph, and J.S. Simons, *A unifying account of angular gyrus contributions to episodic and semantic cognition.* Trends in Neurosciences, 2021. **44**(6): p. 452-463.

226. Singh-Curry, V. and M. Husain, *The functional role of the inferior parietal lobe in the dorsal and ventral stream dichotomy.* Neuropsychologia, 2009. **47**(6): p. 1434-1448.

227. Sack, A.T., *Parietal cortex and spatial cognition.* Behavioural brain research, 2009. **202**(2): p. 153-161.

228. Numssen, O., D. Bzdok, and G. Hartwigsen, *Functional specialization within the inferior parietal lobes across cognitive domains.* Elife, 2021. **10**: p. e63591.

229. Humphreys, G.F. and M.A. Lambon Ralph, *Fusion and fission of cognitive functions in the human parietal cortex.* Cerebral Cortex, 2015. **25**(10): p. 3547-3560.

230. Buckner, R.L. and L.M. DiNicola, *The brain's default network: updated anatomy, physiology and evolving insights.* Nature Reviews Neuroscience, 2019. **20**(10): p. 593-608.

231. Greicius, M.D., et al., *Functional connectivity in the resting brain: a network analysis of the default mode hypothesis.* Proceedings of the National Academy of Sciences, 2003. **100**(1): p. 253-258.

232. Shehzad, Z., et al., *The resting brain: unconstrained yet reliable.* Cerebral cortex, 2009. **19**(10): p. 2209-2229.

233. Bonnard, M., et al., *Resting state brain dynamics and its transients: a combined TMS-EEG study.* Scientific reports, 2016. **6**(1): p. 1-9.

234. Fox, K.C., et al., *Intrinsic network architecture predicts the effects elicited by intracranial electrical stimulation of the human brain.* Nature human behaviour, 2020. **4**(10): p. 1039-1052.

235. Ozdemir, R.A., et al., *Individualized perturbation of the human connectome reveals reproducible biomarkers of network dynamics relevant to cognition.* Proceedings of the National Academy of Sciences, 2020. **117**(14): p. 8115-8125.

236. Dhami, P., et al., *Neurophysiological markers of response to theta burst stimulation in youth depression.* Depression and anxiety, 2021. **38**(2): p. 172-184.

237. Lewis, D.A., *Inhibitory neurons in human cortical circuits: substrate for cognitive dysfunction in schizophrenia.* Current opinion in neurobiology, 2014. **26**: p. 22-26.

238. Xu, Y., et al., *GABAergic inhibitory interneuron deficits in Alzheimer's disease: implications for treatment.* Frontiers in neuroscience, 2020. **14**: p. 660.

239. Fritschy, J.-M., *Epilepsy, E/I balance and GABAA receptor plasticity.* Frontiers in molecular neuroscience, 2008. **1**: p. 5.

240. Luscher, B., Q. Shen, and N. Sahir, *The GABAergic deficit hypothesis of major depressive disorder.* Molecular psychiatry, 2011. **16**(4): p. 383-406.

241. Charych, E.I., et al., *GABAA receptors and their associated proteins: implications in the etiology and treatment of schizophrenia and related disorders.* Neuropharmacology, 2009. **57**(5-6): p. 481-495.

242. Di Cristo, G., *Development of cortical GABAergic circuits and its implications for neurodevelopmental disorders.* Clinical genetics, 2007. **72**(1): p. 1-8.

243. Farrant, M. and K. Kaila, *The cellular, molecular and ionic basis of GABAA receptor signalling.* Progress in brain research, 2007. **160**: p. 59-87.

244. Möhler, H., *GABA A receptor diversity and pharmacology.* Cell and tissue research, 2006. **326**(2): p. 505-516.

245. Serwanski, D.R., et al., *Synaptic and nonsynaptic localization of GABAA receptors containing the α5 subunit in the rat brain.* Journal of Comparative Neurology, 2006. **499**(3): p. 458-470.

246. Riss, J., et al., *Benzodiazepines in epilepsy: pharmacology and pharmacokinetics.* Acta neurologica scandinavica, 2008. **118**(2): p. 69-86.

247. Crestani, F., et al., *Mechanism of action of the hypnotic zolpidem in vivo.* British journal of pharmacology, 2000. **131**(7): p. 1251-1254.

248. Kujirai, T., et al., *Corticocortical inhibition in human motor cortex.* The Journal of physiology, 1993. **471**(1): p. 501-519.

249. Ziemann, U., J.C. Rothwell, and M. Ridding, *Interaction between intracortical inhibition and facilitation in human motor cortex.* The Journal of physiology, 1996. **496**(3): p. 873-881.

250. Chen, R., et al., *Intracortical inhibition and facilitation in different representations of the human motor cortex.* Journal of neurophysiology, 1998. **80**(6): p. 2870-2881.

251. Hanajima, R., et al., *Paired-pulse magnetic stimulation of the human motor cortex: differences among I waves.* The Journal of physiology, 1998. **509**(2): p. 607-618.

252. Lazzaro, V.D., et al., *Magnetic transcranial stimulation at intensities below active motor threshold activates intracortical inhibitory circuits.* Experimental brain research, 1998. **119**(2): p. 265-268.

253. Davey, N.J., et al., *Suppression of voluntary motor activity revealed using transcranial magnetic stimulation of the motor cortex in man.* The Journal of Physiology, 1994. **477**(2): p. 223-235.

254. Fisher, R., et al., *Two phases of intracortical inhibition revealed by transcranial magnetic threshold tracking.* Experimental brain research, 2002. **143**(2): p. 240-248.

255. Ilić, T.V., et al., *Short-interval paired-pulse inhibition and facilitation of human motor cortex: the dimension of stimulus intensity.* The Journal of physiology, 2002. **545**(1): p. 153-167.

256. Müller-Dahlhaus, J.F.M., Y. Liu, and U. Ziemann, *Inhibitory circuits and the nature of their interactions in the human motor cortex–a pharmacological TMS study.* The Journal of physiology, 2008. **586**(2): p. 495-514.

257. Ziemann, U., et al., *The effect of lorazepam on the motor cortical excitability in man.* Experimental brain research, 1996. **109**(1): p. 127-135.

258. Di Lazzaro, V., et al., *Segregating two inhibitory circuits in human motor cortex at the level of GABAA receptor subtypes: a TMS study.* Clinical Neurophysiology, 2007. **118**(10): p. 2207-2214.

259. Cash, R.F., et al., *Characterization of Glutamatergic and GABA A-Mediated Neurotransmission in Motor and Dorsolateral Prefrontal Cortex Using Paired-Pulse TMS–EEG.* Neuropsychopharmacology, 2017. **42**(2): p. 502.

260. Ferreri, F., et al., *Human brain connectivity during single and paired pulse transcranial magnetic stimulation.* Neuroimage, 2011. **54**(1): p. 90-102.

261. Rawji, V., et al., *Preconditioning stimulus intensity alters paired-pulse TMS evoked potentials.* Brain sciences, 2021. **11**(3): p. 326.

262. Noda, Y., et al., *Characterization of the influence of age on GABAA and glutamatergic mediated functions in the dorsolateral prefrontal cortex using paired-pulse TMS-EEG.* Aging (Albany NY), 2017. **9**(2): p. 556.

263. Rocchi, L., et al., *Disentangling EEG responses to TMS due to cortical and peripheral activations.* Brain Stimulation, 2020.

264. Belardinelli, P., et al., *Reproducibility in TMS–EEG studies: A call for data sharing, standard procedures and effective experimental control.* Brain Stimulation: Basic, Translational, and Clinical Research in Neuromodulation, 2019. **12**(3): p. 787-790.

265. Vaughan, H.G., *The neural origins of human event-related potentials.* Annals of the New York Academy of Sciences, 1982.

266. Michel, C.M., et al., *EEG source imaging.* Clinical neurophysiology, 2004. **115**(10): p. 2195-2222.

267. Michel, C.M. and T. Koenig, *EEG microstates as a tool for studying the temporal dynamics of whole-brain neuronal networks: a review.* Neuroimage, 2018. **180**: p. 577-593.

268. Khanna, A., et al., *Microstates in resting-state EEG: current status and future directions.* Neuroscience & Biobehavioral Reviews, 2015. **49**: p. 105-113.

269. Lehmann, D., H. Ozaki, and I. Pál, *EEG alpha map series: brain micro-states by space-oriented adaptive segmentation.* Electroencephalography and clinical neurophysiology, 1987. **67**(3): p. 271-288.

270. Lehmann, D., *Brain electric microstates and cognition: the atoms of thought*, in *Machinery of the Mind*. 1990, Springer. p. 209-224.

271. Murray, M.M., D. Brunet, and C.M. Michel, *Topographic ERP analyses: a step-by-step tutorial review.* Brain topography, 2008. **20**(4): p. 249-264.

272. Lehmann, D. and W. Skrandies, *Reference-free identification of components of checkerboard-evoked multichannel potential fields.* Electroencephalography and clinical neurophysiology, 1980. **48**(6): p. 609-621.

273. Geselowitz, D.B., *The zero of potential.* IEEE Engineering in Medicine and Biology Magazine, 1998. **17**(1): p. 128-136.

274. Rossi, S., et al., *Safety, ethical considerations, and application guidelines for the use of transcranial magnetic stimulation in clinical practice and research.* Clinical neurophysiology, 2009. **120**(12): p. 2008-2039.

275. Gugino, L.D., et al., *Transcranial magnetic stimulation coregistered with MRI: a comparison of a guided versus blind stimulation technique and its effect on evoked compound muscle action potentials.* Clinical neurophysiology, 2001. **112**(10): p. 1781-1792.

276. Conforto, A.B., et al., *Impact of coil position and electrophysiological monitoring on determination of motor thresholds to transcranial magnetic stimulation.* Clinical neurophysiology, 2004. **115**(4): p. 812-819.

277. Hyvärinen, A. and E. Oja, *Independent component analysis: algorithms and applications.* Neural networks, 2000. **13**(4-5): p. 411-430.

278. Winkler, I., S. Haufe, and M. Tangermann, *Automatic classification of artifactual ICA-components for artifact removal in EEG signals.* Behavioral and Brain Functions, 2011. **7**(1): p. 1-15.

279. Koenig, T., et al., *Ragu: a free tool for the analysis of EEG and MEG event-related scalp field data using global randomization statistics.* Computational intelligence and neuroscience, 2011. **2011**.

280. Habermann, M., et al., *A student's guide to randomization statistics for multichannel event-related potentials using ragu.* Frontiers in neuroscience, 2018. **12**: p. 355.

281. Wilks, S.S., *Multivariate statistical outliers.* Sankhyā: The Indian Journal of Statistics, Series A, 1963: p. 407-426.

282. Koenig, T., et al., *A tutorial on data-driven methods for statistically assessing ERP topographies.* Brain topography, 2014. **27**(1): p. 72-83.

283. Yaffe, R.B., et al., *Reinstatement of distributed cortical oscillations occurs with precise spatiotemporal dynamics during successful memory retrieval.* Proceedings of the National Academy of Sciences, 2014. **111**(52): p. 18727-18732.

284. Kerwin, L.J., et al., *Test-retest reliability of transcranial magnetic stimulation EEG evoked potentials.* Brain stimulation, 2018. **11**(3): p. 536-544.

285. Niessen, E., et al., *An analytical approach to identify indirect multisensory cortical activations elicited by TMS?* Brain Stimulation: Basic, Translational, and Clinical Research in Neuromodulation, 2021. **14**(2): p. 376-378.

286. Kujirai, T., et al., *The effect of transcranial magnetic stimulation on median nerve somatosensory evoked potentials.* Electroencephalography and Clinical Neurophysiology/Evoked Potentials Section, 1993. **89**(4): p. 227-234.

287. Buchner, H., et al., *Source analysis of median nerve and finger stimulated somatosensory evoked potentials: multichannel simultaneous recording of electric and magnetic fields combined with 3D-MR tomography.* Brain topography, 1994. **6**(4): p. 299-310.

288. Van de Wassenberg, W., et al., *Multichannel recording of median nerve somatosensory evoked potentials.* Neurophysiologie Clinique/Clinical Neurophysiology, 2008. **38**(1): p. 9-21.

289. Allison, T., et al., *Human cortical potentials evoked by stimulation of the median nerve. II. Cytoarchitectonic areas generating short-latency activity.* Journal of neurophysiology, 1989. **62**(3): p. 694-710.

290. Rothwell, J., S. Gandevia, and D. Burke, *Activation of fusimotor neurones by motor cortical stimulation in human subjects.* The Journal of Physiology, 1990. **431**(1): p. 743-756.

291. Haider, B., et al., *Neocortical network activity in vivo is generated through a dynamic balance of excitation and inhibition.* Journal of Neuroscience, 2006. **26**(17): p. 4535-4545.

292. Yizhar, O., et al., *Neocortical excitation/inhibition balance in information processing and social dysfunction.* Nature, 2011. **477**(7363): p. 171-178.

293. Kubota, Y., et al., *The diversity of cortical inhibitory synapses.* Frontiers in neural circuits, 2016. **10**: p. 27.

294. Jiang, X., et al., *Principles of connectivity among morphologically defined cell types in adult neocortex.* Science, 2015. **350**(6264): p. aac9462.

295. Cruikshank, S.J., T.J. Lewis, and B.W. Connors, *Synaptic basis for intense thalamocortical activation of feedforward inhibitory cells in neocortex.* Nature neuroscience, 2007. **10**(4): p. 462-468.

296. Huguenard, J.R. and D.A. McCormick, *Thalamic synchrony and dynamic regulation of global forebrain oscillations.* Trends in neurosciences, 2007. **30**(7): p. 350-356.

297. Zhu, S., et al., *Structure of a human synaptic GABAA receptor.* Nature, 2018. **559**(7712): p. 67-72.

298. Hallett, M., *Transcranial magnetic stimulation and the human brain.* Nature, 2000. **406**(6792): p. 147-150.

299. Ziemann, U., et al., *TMS and drugs revisited 2014.* Clinical neurophysiology, 2015. **126**(10): p. 1847-1868.

300. Leodori, G., et al., *Intracortical inhibition and surround inhibition in the motor cortex: a TMS-EEG study.* Frontiers in neuroscience, 2019. **13**: p. 612.

301. Möhler, H., J. Fritschy, and U. Rudolph, *A new benzodiazepine pharmacology.* Journal of Pharmacology and Experimental Therapeutics, 2002. **300**(1): p. 2-8.

302. Greenblatt, D.J. and C.E. Wright, *Clinical pharmacokinetics of alprazolam.* Clinical pharmacokinetics, 1993. **24**(6): p. 453-471.

303. Barbanoj, M., et al., *Different acute tolerance development to EEG, psychomotor performance and subjective assessment effects after two intermittent oral doses of alprazolam in healthy volunteers.* Neuropsychobiology, 2007. **55**(3-4): p. 203-212.

304. Šulcová, D., et al., *Investigating the origin of TMS-evoked brain potentials using topographic analysis.* 2022.

305. Saletu, B., P. Anderer, and G.M. Saletu-Zyhlarz, *EEG topography and tomography (LORETA) in the classification and evaluation of the pharmacodynamics of psychotropic drugs.* Clinical EEG and neuroscience, 2006. **37**(2): p. 66-80.

306. Gilles, C. and R. Luthringer, *Pharmacological models in healthy volunteers: their use in the clinical development of psychotropic drugs.* Journal of Psychopharmacology, 2007. **21**(3): p. 272-282.

307. Buchsbaum, M.S., et al., *Topographic EEG changes with benzodiazepine administration in generalized anxiety disorder.* Biological psychiatry, 1985. **20**(8): p. 832-842.

308. Veselis, R.A., et al., *Use of neural network analysis to classify electroencephalographic patterns against depth of midazolam sedation in intensive care unit patients.* Journal of clinical monitoring, 1991. **7**(3): p. 259-267.

309. Kaida, K., et al., *Validation of the Karolinska sleepiness scale against performance and EEG variables.* Clinical neurophysiology, 2006. **117**(7): p. 1574-1581.

310. Stampi, C., P. Stone, and A. Michimori, *A new quantitative method for assessing sleepiness: the Alpha Attenuation Test.* Work & Stress, 1995. **9**(2-3): p. 368-376.

311. Feshchenko, V.A., R.A. Veselis, and R.A. Reinsel, *Comparison of the EEG effects of midazolam, thiopental, and propofol: the role of underlying oscillatory systems.* Neuropsychobiology, 1997. **35**(4): p. 211-220.

312. Nutt, D., et al., *Differences between magnetoencephalographic (MEG) spectral profiles of drugs acting on GABA at synaptic and extrasynaptic sites: a study in healthy volunteers.* Neuropharmacology, 2015. **88**: p. 155-163.

313. Lozano-Soldevilla, D., *On the physiological modulation and potential mechanisms underlying parieto-occipital alpha oscillations.* Frontiers in computational neuroscience, 2018. **12**: p. 23.

314. Colombo, M.A., et al., *The spectral exponent of the resting EEG indexes the presence of consciousness during unresponsiveness induced by propofol, xenon, and ketamine.* NeuroImage, 2019. **189**: p. 631-644.

315. Gao, R.D., E.J. Peterson, and B. Voytek, *Inferring Synaptic Excitation/Inhibition Balance from Field Potentials.* bioRxiv, 2016: p. 081125.

316. R Core Team, *R: A language and environment for statistical computing.* 2021, R Foundation for Statistical Computing: Vienna, Austria.

317. Bates, D., et al., *Fitting Linear Mixed-Effects Models Using lme4.* Journal of Statistical Software, 2015. **67**(1): p. 1 - 48.

318. Kuznetsova, A., P.B. Brockhoff, and R.H.B. Christensen, *lmerTest Package: Tests in Linear Mixed Effects Models.* Journal of Statistical Software, 2017. **82**(13): p. 1 - 26.

319. Banoub, M., J.E. Tetzlaff, and A. Schubert, *Pharmacologic and physiologic influences affecting sensory evoked potentials: implications for perioperative monitoring.* The Journal of the American Society of Anesthesiologists, 2003. **99**(3): p. 716-737.

320. Scaife, J., et al., *Sensitivity of late-latency auditory and somatosensory evoked potentials to threat of electric shock and the sedative drugs diazepam and diphenhydramine in human volunteers.* Journal of Psychopharmacology, 2006. **20**(4): p. 485-495.

321. Rockstroh, B., et al., *Effects of the anticonvulsant benzodiazepine clonazepam on event-related brain potentials in humans.* Electroencephalography and clinical neurophysiology, 1991. **78**(2): p. 142-149.

322. Casula, E.P., et al., *Low-frequency rTMS inhibitory effects in the primary motor cortex: Insights from TMS-evoked potentials.* Neuroimage, 2014. **98**: p. 225-232.

323. Mandema, J.W. and M. Danhof, *Electroencephalogram effect measures and relationships between pharmacokinetics and pharmacodynamics of centrally acting drugs.* Clinical pharmacokinetics, 1992. **23**(3): p. 191-215.

324. Kilavik, B.E., et al., *The ups and downs of beta oscillations in sensorimotor cortex.* Experimental neurology, 2013. **245**: p. 15-26.

325. Engel, A.K. and P. Fries, *Beta-band oscillations—signalling the status quo?* Current opinion in neurobiology, 2010. **20**(2): p. 156-165.

326. Gilbertson, T., et al., *Existing motor state is favored at the expense of new movement during 13-35 Hz oscillatory synchrony in the human corticospinal system.* Journal of Neuroscience, 2005. **25**(34): p. 7771-7779.

327. Pogosyan, A., et al., *Boosting cortical activity at beta-band frequencies slows movement in humans.* Current biology, 2009. **19**(19): p. 1637-1641.

328. Miskovic, V., et al., *Changes in EEG multiscale entropy and power-law frequency scaling during the human sleep cycle.* Human brain mapping, 2019. **40**(2): p. 538-551.

329. Lendner, J.D., et al., *An electrophysiological marker of arousal level in humans.* Elife, 2020. **9**.

330. Gao, R., E.J. Peterson, and B. Voytek, *Inferring synaptic excitation/inhibition balance from field potentials.* Neuroimage, 2017. **158**: p. 70-78.

331. Di Lazzaro, V., et al., *Direct demonstration of the effect of lorazepam on the excitability of the human motor cortex.* Clinical neurophysiology, 2000. **111**(5): p. 794-799.

332. Di Lazzaro, V., et al., *Effects of lorazepam on short latency afferent inhibition and short latency intracortical inhibition in humans.* The Journal of physiology, 2005. **564**(2): p. 661-668.

333. Teo, J., et al., *Differing effects of intracortical circuits on plasticity.* Experimental brain research, 2009. **193**(4): p. 555-563.

334. Hagmann, P., et al., *Mapping the structural core of human cerebral cortex.* PLoS biology, 2008. **6**(7): p. e159.

335. Buckner, R.L., J.R. Andrews-Hanna, and D.L. Schacter, *The brain's default network: anatomy, function, and relevance to disease.* Annals of the new York Academy of Sciences, 2008. **1124**(1): p. 1-38.

336. Price, A.R., et al., *Converging evidence for the neuroanatomic basis of combinatorial semantics in the angular gyrus.* Journal of Neuroscience, 2015. **35**(7): p. 3276-3284.

337. Binder, J.R., et al., *Where is the semantic system? A critical review and meta-analysis of 120 functional neuroimaging studies.* Cerebral cortex, 2009. **19**(12): p. 2767-2796.

338. Davey, J., et al., *Automatic and controlled semantic retrieval: TMS reveals distinct contributions of posterior middle temporal gyrus and angular gyrus.* Journal of neuroscience, 2015. **35**(46): p. 15230-15239.

339. Ciaramelli, E., C.L. Grady, and M. Moscovitch, *Top-down and bottom-up attention to memory: a hypothesis (AtoM) on the role of the posterior parietal cortex in memory retrieval.* Neuropsychologia, 2008. **46**(7): p. 1828-1851.

340. Vilberg, K.L. and M.D. Rugg, *Memory retrieval and the parietal cortex: a review of evidence from a dual-process perspective.* Neuropsychologia, 2008. **46**(7): p. 1787-1799.

341. Bonnici, H.M., et al., *Specifying a causal role for angular gyrus in autobiographical memory.* Journal of Neuroscience, 2018. **38**(49): p. 10438-10443.

342. Ardila, A., *A proposed reinterpretation of Gerstmann's syndrome.* Archives of clinical neuropsychology, 2014. **29**(8): p. 828-833.

343. Jagust, W., et al., *Brain imaging evidence of preclinical Alzheimer's disease in normal aging.* Annals of Neurology: Official Journal of the American Neurological Association and the Child Neurology Society, 2006. **59**(4): p. 673-681.

344. Smith, C., et al., *Brain structural alterations before mild cognitive impairment.* Neurology, 2007. **68**(16): p. 1268-1273.

345. Berron, D., et al., *Medial temporal lobe connectivity and its associations with cognition in early Alzheimer's disease.* Brain, 2020. **143**(4): p. 1233-1248.

346. Chahine, G., et al., *Disruptions in the left frontoparietal network underlie resting state endophenotypic markers in schizophrenia.* Human Brain Mapping, 2017. **38**(4): p. 1741-1750.

347. Torrey, E.F., *Schizophrenia and the inferior parietal lobule.* Schizophrenia research, 2007. **97**(1-3): p. 215-225.

348. Sakurai, T., et al., *Dysfunction of the left angular gyrus may be associated with writing errors in ALS.* Amyotrophic lateral sclerosis and frontotemporal degeneration, 2021. **22**(3-4): p. 267-275.

349. Agosta, F., et al., *Divergent brain network connectivity in amyotrophic lateral sclerosis.* Neurobiology of aging, 2013. **34**(2): p. 419-427.

350. Macdonald, V., et al., *Significant loss of pyramidal neurons in the angular gyrus of patients with Huntington's disease.* Neuropathology and applied neurobiology, 1997. **23**(6): p. 492-495.

351. Ogawa, S., et al., *Brain magnetic resonance imaging with contrast dependent on blood oxygenation.* proceedings of the National Academy of Sciences, 1990. **87**(24): p. 9868-9872.

352. Attwell, D. and C. Iadecola, *The neural basis of functional brain imaging signals.* Trends in neurosciences, 2002. **25**(12): p. 621-625.

353. Cole, D.M., S.M. Smith, and C.F. Beckmann, *Advances and pitfalls in the analysis and interpretation of resting-state FMRI data.* Frontiers in systems neuroscience, 2010: p. 8.

354. Ferreri, F. and P.M. Rossini, *TMS and TMS-EEG techniques in the study of the excitability, connectivity, and plasticity of the human motor cortex.* Reviews in the Neurosciences, 2013. **24**(4): p. 431-442.

355. Bergmann, T.O. and G. Hartwigsen, *Inferring causality from noninvasive brain stimulation in cognitive neuroscience.* Journal of cognitive neuroscience, 2021. **33**(2): p. 195-225.

356. Fox, P.T., et al., *Column-based model of electric field excitation of cerebral cortex.* Hum Brain Mapp, 2004. **22**(1): p. 1-14.

357. Caspers, S., et al., *The human inferior parietal lobule in stereotaxic space.* Brain Structure and Function, 2008. **212**(6): p. 481-495.

358. Seghier, M.L., E. Fagan, and C.J. Price, *Functional subdivisions in the left angular gyrus where the semantic system meets and diverges from the default network.* Journal of Neuroscience, 2010. **30**(50): p. 16809-16817.

359. Nelson, S.M., et al., *A parcellation scheme for human left lateral parietal cortex.* Neuron, 2010. **67**(1): p. 156-170.

360. Sulcova, D., et al., *Evaluation of GABAAR-mediated inhibition in the human brain using TMS-evoked potentials.* bioRxiv, 2022: p. 2022.10.31.514225.

361. Sulcova, D., et al., *Investigating the origin of TMS-evoked brain potentials using topographic analysis.* Brain Topography, 2022: p. 1-16.

362. Chowdhury, N.S., et al., *The influence of sensory potentials on transcranial magnetic stimulation–Electroencephalography recordings.* Clinical Neurophysiology, 2022. **140**: p. 98-109.

363. Poorganji, M., et al., *Differentiating Transcranial Magnetic Stimulation Cortical and Auditory Responses via Single Pulse and Paired Pulse protocols: A TMS-EEG study.* Clinical Neurophysiology, 2021.

364. Raichle, M.E., et al., *A default mode of brain function.* Proceedings of the National Academy of Sciences, 2001. **98**(2): p. 676-682.

365. Machetanz, J., et al., *Magnetically induced muscle contraction is caused by motor nerve stimulation and not by direct muscle activation.* Muscle & Nerve: Official Journal of the American Association of Electrodiagnostic Medicine, 1994. **17**(10): p. 1170-1175.

366. Miller, L.E., M.R. Longo, and A.P. Saygin, *Tool use modulates somatosensory cortical processing in humans.* Journal of cognitive neuroscience, 2019. **31**(12): p. 1782-1795.

367. Restuccia, D., et al., *Modality-related scalp responses after electrical stimulation of cutaneous and muscular upper limb afferents in humans.* Muscle & Nerve: Official Journal of the American Association of Electrodiagnostic Medicine, 2002. **26**(1): p. 44-54.

368. Sulcova, D., et al., *Exploring the properties of the left angular gyrus using TMS-evoked potentials.* bioRxiv, 2022: p. 2022.11.15.516568.

369. Cash, R.F., et al., *Using brain imaging to improve spatial targeting of transcranial magnetic stimulation for depression.* Biological Psychiatry, 2021. **90**(10): p. 689-700.

370. Lioumis, P. and M. Rosanova, *The role of neuronavigation in TMS–EEG studies: Current applications and future perspectives.* Journal of Neuroscience Methods, 2022: p. 109677.

371. Casarotto, S., et al., *The rt-TEP tool: real-time visualization of TMS-evoked potentials to maximize cortical activation and minimize artifacts.* Journal of Neuroscience Methods, 2022. **370**: p. 109486.

372. Schiller, B., et al., *Clocking the social mind by identifying mental processes in the IAT with electrical neuroimaging.* Proceedings of the National Academy of Sciences, 2016. **113**(10): p. 2786-2791.

373. Bréchet, L., et al., *Capturing the spatiotemporal dynamics of self-generated, task-initiated thoughts with EEG and fMRI.* Neuroimage, 2019. **194**: p. 82-92.

374. Iannotti, G.R., et al., *EEG Spatiotemporal patterns underlying self-other voice discrimination.* Cerebral cortex, 2022. **32**(9): p. 1978-1992.